CHALMERS
UNIVERSITY OF TECHNOLOGY

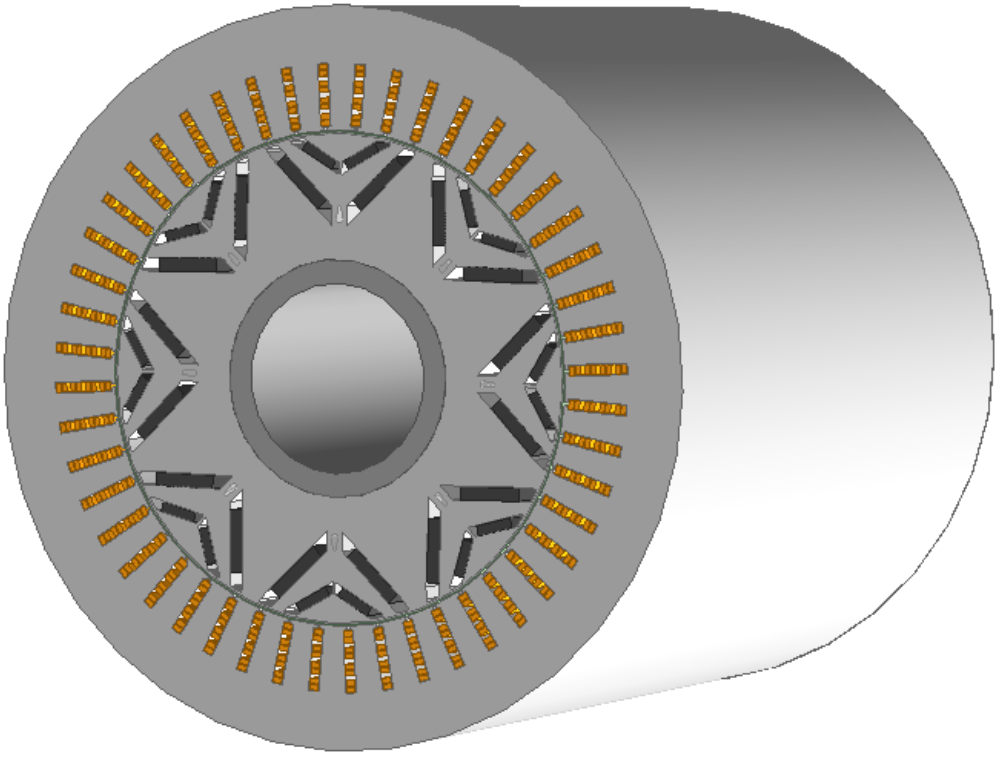

Investigation of Circulating Currents in Delta Connected PMSM

A Combined Analytical and Numerical Approach Considering Rotor Design

Master's thesis in Sustainable Electric Power Engineering and Electromobility

GUSTAV TYDÉN
EMIL CALLERFJORD

DEPARTMENT OF ELECTRICAL ENGINEERING
CHALMERS UNIVERSITY OF TECHNOLOGY
Gothenburg, Sweden 2024
www.chalmers.se

Master's thesis 2024

Investigation of Circulating Currents in Delta Connected PMSM

A Combined Analytical and Numerical Approach Considering Rotor Design

GUSTAV TYDÉN
EMIL CALLERFJORD

CHALMERS
UNIVERSITY OF TECHNOLOGY

Department of Electrical Engineering
Division of Electric Power Engineering
Chalmers University of Technology
Gothenburg, Sweden 2024

Investigation of Circulating Currents in Delta Connected PMSM
A Combined Analytical and Numerical Approach Considering Rotor Design
GUSTAV TYDÉN
EMIL CALLERFJORD

Supervisor: Rasmus Andersson, Volvo Group Trucks Technology
Supervisor: Zhe Huang, Volvo Group Trucks Technology
Examiner: Torbjörn Thiringer, Department of Electrical Engineering

Master's Thesis 2024
Department of Electrical Engineering
Division of Electric Power Engineering
Chalmers University of Technology
SE-412 96 Gothenburg
Telephone +46 31 772 1000

Cover: Circulating currents

Typeset in LaTeX
Printed by Chalmers Reproservice
Gothenburg, Sweden 2024

Investigation of Circulating Currents in Delta Connected PMSM
A Combined Analytical and Numerical Approach Considering Rotor Design
GUSTAV TYDÉN
EMIL CALLERFJORD
Department of Electrical Engineering
Chalmers University of Technology

Abstract

Triplen harmonics are a key concern in delta connected machines, primarily because they lead to circulating currents which decreases the efficiency of the machine. This thesis presents a comprehensive analysis, employing both analytical and numerical methods, to enhance the understanding of triplen harmonic generation in relation to rotor design. Specifically, the study focuses on a delta connected double-layer interior permanent magnet synchronous machine (DIPMSM), where the phenomena of circulating currents is analyzed as a consequence of the triplen harmonics in the generated flux linkage.

In the study, eight rotor parameters are thoroughly investigated individually, in pairs and through interconnected influence on the circulating currents. The parametric research was conducted numerically in Ansys Maxwell. It is concluded that the arc angles and the inner extension spacing length are the most significant parameters with respect to the third harmonic current amplitude.

Furthermore, the study identifies the iron core saturation as having the greatest impact on the amplitude of the circulating currents. This is found due to the reason of the specific third harmonic enhancement with increasing levels of saturation. Spectral analysis is employed to break down current harmonic components in the delta loop, leading to the construction of an optimization strategy for minimizing circulating current based on rotor parameters. The optimal rotor design reduced the third harmonic by 95.5% in no-load conditions and 5.7% in maximum load condition, highlighting that the saturation effect inducing the third harmonic cannot be eliminated by optimal rotor parametric alignment.

Keywords: Circulating currents, triplen harmonics, delta connected PMSM.

Acknowledgements

We would like to express our sincerest gratitude to our supervisors Rasmus Andersson and Zhe Huang at Volvo GTT for their continuous guidance and support. Your encouragement and expertise have been instrumental in the completion of our work. The insights and advice you provided have greatly enriched our research process.

Furthermore, we would like to extend our deepest thanks to our examiner, Torbjörn Thiringer for his invaluable feedback and thorough evaluation of our thesis. His support and constructive criticism have not only improved our work but also contributed to our professional growth. We also want to thank our good friend Oskar Blom who generously shared his time and insights, making this research possible.

Finally, we would like to articulate our heartfelt appreciation to our families, particularly our respective partners Felicia Lindström and Halime Selimoglu. Their unwavering support throughout this journey. Without your encouragement and belief in us, this work would not have been possible.

Gustav Tydén, Gothenburg, May 2024
Emil Callerfjord, Gothenburg, May 2024

List of Acronyms

ANOVA	Analysis of Variance
Back-EMF	Back-electromotive force
B-field	Magnetic flux density
D-axis	Direct axis
DIPMSM	Double-layer interior permanent magnet synchronous machine
DOE	Design of Experiments
DQ-frame	Direct and quadrant frame
H-field	Magnetic field strength
FEA	Finite element analysis
FEM	Finite element method
FFT	Fast Fourier transform
IPMSM	Interior permanent magnet synchronous machine
MTPA	Maximum torque per ampere
OA	Orthogonal array
PMSM	Permanent magnet synchronous machine
Q-axis	Quadrature axis
REE	Rare earth elements

Nomenclature

Parameters

$L1$	First magnet layer, closest to rotor shaft
$L2$	Second magnet layer, closest to air-gap
$L1_{Arc}$	First magnet layer arc angle
$L2_{Arc}$	Second magnet layer arc angle
$L1_{Pole}$	First magnet layer pole angle
$L2_{Pole}$	Second magnet layer pole angle
$L1_{T}$	First magnet layer thickness
$L2_{T}$	Second magnet layer thickness
$L1_{Ext}$	First magnet layer flux barrier spacing extension
$L2_{Ext}$	Second magnet layer flux barrier spacing extension

Variables

I_{cc}	Circulating Currents [A]
$\hat{I}$	Peak Current [A]
I_a	Phase A Current [A]
I_b	Phase B Current [A]
I_c	Phase C Current [A]
I_{line}	Line Current [A]
I_{phase}	Phase Current [A]
Ψ	Flux Linkage [Wb]
Ψ_h	Flux Linkage Harmonic Amplitude [Wb]
R_s	Stator Resistance [Ω]
L_s	Self Inductance [H]

L_m	Mutual Inductance [H]
h	Harmonic Order
n	Number of Phases
N_s	Number of Turns
$N_{parallel}$	Number of Parallel Branches
p	Number of Poles
Q	Number of Stator Slots
q	Number of Slots per Pole per Phase
k_{fill}	Copper Fill Factor
V_{DC}	DC link voltage [V]
r	Number of Winding Layers
B_{airgap}	Air-gap Flux Density [T]
$B_{airgap\|3^{rd}}$	Third Harmonic Air-gap Flux Density [T]
A_{airgap}	Air-gap Area [m^2]
ω	Electrical Frequency [rad/s]
μ_0	Permeability of Vacuum [H/m]
μ_r	Relative Permeability [H/m]
H	Magnetic Field Strength [A/m]
B	Magnetic Flux Density [T]
$\Re$	Magnetic Reluctance [1/H]
Ψ_d	d-axis Flux Linkage [Wb]
Ψ_q	q-axis Flux Linkage [Wb]
Ψ_m	Mutual Flux Linkage [Wb]
L_d	d-axis Inductance [H]
L_q	q-axis Inductance [H]
L_{ew}	End winding length [m]
L_{pitch}	Pitch Length [m]
L_{endext}	End Extension Length [m]
A_{coil}	Coil Area [m^2]
R_{ew}	End Winding Resistance [Ω]
$r_{slotcenter}$	Radius of Slotcenter [m]
ρ_{cu}	Resistivity of Copper [Ωm]

Contents

1
Introduction

The role of electrical machines in traction applications is drastically increasing. Long haul trucks and buses, as well as transit buses, are responsible for more than 25% of all greenhouse gas emissions from the road transport section within the European Union (EU), and responsible for over 6% of all greenhouse gas emissions in the EU [1]. This has severe consequences for humans and ecosystems. Increased occurrences of extreme weather, irreversible damage to ecosystems, and negatively impacting human and animal health living in affected areas.

The European Commission has set the goal that all member states of the EU should be climate-neutral as a whole by 2050 [2]. Specifically, Volvo Group has set the goal for 2035 that 35% of all sold vehicles should be fully electric. And by 2040, the goal is set to have a net-zero value chain, enabling the customers to have a zero-emission fleet by 2050 [3].

In this context, the research and development of electrical machines play a pivotal role in realizing these sustainability goals. Among these electrical traction machines is the permanent magnet synchronous machine (PMSM) who stands out for its power density. Leading to size-saving, weight, and material reduction which are factors of high importance for sustainable traction components. To further enhance the usage of PMSMs, delta connections can assure machine scalability by voltage instead of the common core active length adjustments, thus simplifying production. However, circulating currents are inherent characteristics of delta connected PMSM which are problematic due to the risk of increased power losses thus reducing the efficiency.

1.1 Background

PMSMs are commonly used in heavy duty applications due to their high power density and efficiency. Scalability of these machines becomes of great importance to reduce manufacturing costs for mass production. There are several ways of scaling the characteristics of PMSMs. In order to scale the power output, the induced voltage needs to be adjusted, where the flux linkage is serving as the driving factor. Scaling the core length or changing the number of magnets in the rotor are methods that are easily adopted but comes with a high cost. However, by changing the connection type from star to delta, the phase voltages can be changed with a much lower cost. In fact, even though star connection is commonly used in traction applications, switching to delta connection have several advantages regarding the cost

of manufacturing since the neutral point is not needed, no bus-bar will be needed, ultimately reducing manufacturing costs [4].

Using a delta connection the flexibility of scaling the flux linkage is increased. But due to the lack of a neutral point typically found in wye connection. The non-sinusoidal waveform of the flux linkage will generate back-electromotive force (back-EMF) harmonics in the three phase windings, which in turn generates circulating currents. These circulating currents can lead to additional copper losses and heating, thus reduced efficiency [4].

1.1.1 Aim

The project aims to investigate circulating currents within delta connected PMSMs as a function of rotor design, by analyzing rotor parameters individually and their interconnection. The goal is to gain insights into the emergence of circulating currents and how to mitigate them.

Specifically, the aim of this thesis encompasses:

- Identifying the relationship between circulating current and the triplen harmonic generated in the air-gap flux.
- Defining the rotor parameters under investigation.
- Numerically evaluating the correlation between the defined rotor parameters and circulating current in the delta connection.
- Identifying specific rotor design aspects affecting the enhancement of the third harmonic.
- Minimizing circulating current in a numerical delta connected permanent magnet synchronous machine.

1.1.2 Limitations

This thesis is constrained to cover:

- Numerical and analytical models exclusively, precluding testing on a real machine.
- Permanent magnet machine rotor design.
- Load condition represented solely as pure sinusoidal line current.
- Full pitch winding configuration.
- Copper winding losses.
- Solely circulating currents, no further performance or efficiency evaluation is covered.

1.2 Previous work

The research on the reduction of circulating currents in a delta connected double-layer interior permanent magnet synchronous machine (DIPMSM) is relatively unexplored. Existing literature, while investigating surface mounted magnets [5] and

single layer interior magnets [6], [7] provides important groundwork and insight into this study. Notably, the work done by [8] provides valuable context and has paved the path for the continuing work of investigating circulating currents in a delta connected DIPMSM. In [8] it is concluded that the magnet location within the rotor as well as the magnet characteristics, such as thickness and pole angle directly impacts the air-gap flux waveform and can be adjusted to lower the third harmonic. A second important conclusion is that the third harmonic present in the air-gap flux is transferred to the back-EMF.

1.3 Societal, ethical and ecological aspects

Electric traction machines, including DIPMSMs, have a significant advantage in reducing reducing green house emission, noise pollution and energy consumption compared to traditional combustion engines. An increase in scalability of DIPMSM and the reduction in component numbers have the capability of lowering the cost of these machines and to accelerate the transition of the transport industry into net zero carbon emissions. It is difficult to anticipate any direct negative societal impact stemming from the use of delta connected configuration.

From an ethical standpoint, while no immediate issues are evident in the development and application of electric machines or the methodologies employed in this research, broader ethical considerations do emerge. Specifically, the sourcing of materials for permanent magnets, such as rare-earth elements (REE) which are critical for the performance of DIPMSM. The mining and processing of these materials pose significant environmental and social challenges, including habitat destruction as well as water and air pollution causing health problems for nearby residents. Moreover, the common REE neodymium-iron-boron (NdFeB) is non-biodegradable and portrays troublesome challenges in recycling processes [9]. As further discussed in [9], innovative recycling methods are being explored, where each method primarily aims to purify the REEs and improve the extraction processes. These methods have a potential to enhance the recyclability of permanent magnet, thereby reduce the reliance on mining processes.

From an ecological perspective, if delta connected machines can be developed with the knowledge of circulating currents and how to reduce them, this would lead to a decrease in energy consumption and material usage which is only beneficial from an ecological perspective.

2

Theory

This chapter covers the underlying theories used in the thesis. First, theories regarding harmonics in three phase systems are presented followed by electrical machine connection types. Then, relevant theories for the permanent magnet synchronous machine are listed specified for the v-shaped rotor topology. Finally, theories explaining optimization methods and techniques used in the thesis are displayed.

2.1 Harmonics

Harmonics refer to elements within a complex waveform, that occur at frequencies that are integer multiples of the fundamental frequency. The fundamental frequency is the supply frequency and is equal to the first, as well as the lowest frequency component. Harmonics can lead to increased power losses and dielectric losses as well as unwanted capacitive currents [10]. In three phase power systems, harmonics are a consequence of imbalances between the phases and occur due to many different reasons. Harmonic components are categorized based on their phase sequence and harmonic order.

A harmonic component has a phasor rotation in relation to the fundamental wave. The relation describes a harmonic components phase sequence. In three phase systems there are three separate sequences, positive-sequence, negative-sequence, and zero-sequence. Depending on system and load, the different sequences can have different impact.

The positive-sequence harmonics have the same phase rotation as the fundamental frequency and are the harmonics in order of 1st, 4th, 7th, etc. multiples of the fundamental frequency are generated. The negative-sequence harmonics have the opposite phase rotation in relation to the fundamental frequency, creating harmonics in the order of 2nd, 5th, 8th, etc. multiples of the fundamental frequency.

The zero-sequence harmonics have zero rotational phase sequence meaning that zero-sequence harmonics are defined by the same magnitude and phase angle as the fundamental signal at a specific instant in time. These harmonics are represented by the a multiple of three time the fundamental frequency (3rd, 6th, 9th, etc.). These are denoted as the triplen harmonic, or sometimes as the third harmonic multiple. In a three phase system with each phase shifted $\frac{2\pi}{3}$ radians the expression for the

phase currents including a third harmonic are,

$$I_a = \hat{I}\sin(\omega t) + \hat{I}\sin(3\omega t) \tag{2.1a}$$

$$I_b = \hat{I}\sin\left(\omega t - \frac{2\pi}{3}\right) + \hat{I}\sin(3\omega t) \tag{2.1b}$$

$$I_c = \hat{I}\sin\left(\omega t + \frac{2\pi}{3}\right) + \hat{I}\sin(3\omega t) \tag{2.1c}$$

The resulting third harmonic multiples are equal in each phase, since the phase angle of each third harmonic multiple component equals to 0 as,

$$|\frac{2\pi}{3}| \times 3 = |-\frac{2\pi}{3}| \times 3 = 2\pi\ rad = 0\ rad \tag{2.2}$$

In a perfectly balanced three phase system, the zero-sequence components are ideally zero, since the sum of the phases cancel out. However, in systems containing harmonic distortion, zero-sequence components are present. In systems with a neutral conductor, the zero-sequence components are the apparent voltage and current flowing in the neutral. In Figure 2.1, an example of a signal consisting of triplen harmonics is shown as components of a signal as well as a complete composite signal distorted for the same harmonics.

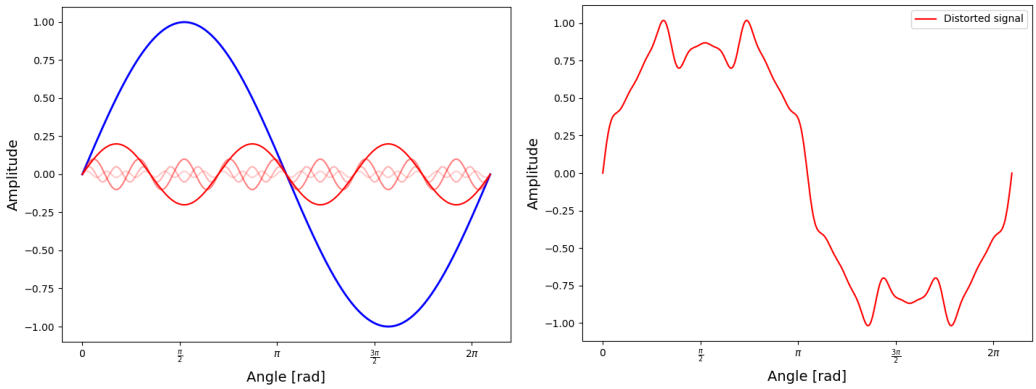

(a) Decomposed harmonic signal **(b)** Distorted signal

Figure 2.1: Triplen harmonics distortion

2.1.1 Fast Fourier transform

Fourier transform is a tool for transforming signals from the time domain to a representation in the frequency domain. The transformation decomposes complex signals into simpler sinusoidal components, making them easier to understand and manipulate. The Fast Fourier Transform (FFT) is an algorithmic technique that builds upon the principles of the Fourier Transform, enhancing its efficiency in signal-processing applications. While the Fourier Transform provides a valuable means of converting signals from the time domain to the frequency domain, however, it entails a high level of computational complexity. FFT utilizes the Fourier transform and significantly

reduces the number of arithmetic operations required to perform the transformation.

In electrical traction machine models, FFT can be used to in a sufficient way calculate the harmonic content in the generated electromagnetic quantities.

2.1.2 Hairpin

The winding type has gotten its name from the shape it forms when being bent into a hairpin shape. It yields higher copper fill factor than conventional stranded winding type, ultimately leading to higher power density [11]. In turn, higher power density means that a machine can produce more power while being smaller in size. This is a highly desirable attribute due to its space saving benefits as well as the reduction in cost due to material saving.

Moreover, the process of manufacturing hairpin winding type can be automated in an easier process, and thereby beneficial in large scale production [12]. However, the type has a relatively low electromagnetic flexibility since the number of variants of series and parallel conductors are decreased compared with stranded winding.

2.1.3 Star connection

Star connection, sometimes also denoted as wye or Y connection is the most commonly used connection type in electrical machines. If the the connection is made without a neutral return path the zero sequence current is simply eliminated. If there would be a neutral return path the zero sequence current would flow through the neutral. Either way, the zero sequence current can not flow through the phase windings due to Kirchhoff's current law where the sum of currents flowing in to one node is equal to the sum of the currents flowing out of the same node.

However, the wye connection uses more copper as it is in need for a neutral point connection ring bar as well as the need for high amount of winding turns per slot to adjust for the low phase voltage [4].

Figure 2.2 shows how a wye connection connects to an electrical machine, where the colors represent different phases in a three phase configuration.

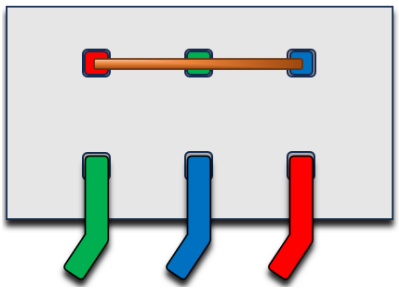

Figure 2.2: Wye connection

2.1.4 Delta connection

Delta connections provide higher phase voltage than wye connection and therefore needs less winding turns per slot. There is also no need for a neutral point connection ring bar. Consequently a delta connection machine can use less copper [4].

On the other hand, in a delta connection the phase currents and line currents are unequal as,

$$I_{line} = \sqrt{3} \times I_{phase} \tag{2.3}$$

Figure 2.3 shows how a delta connection connects to an electrical machine with three phases.

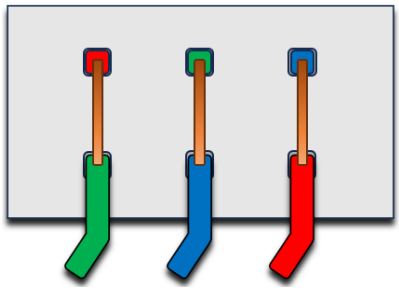

Figure 2.3: Delta connection

Despite having some clear advantages, the delta connection can suffer from circulating currents [13]. A phenomena that occurs in delta winding configurations due to zero sequence harmonics as explained in 2.1. Compared to wye-configuration, the circulating currents can not be cancelled in delta-configuration. Due to the fact that the back-EMF voltage have zero relative phase between the individual phase winding. Instead the phase harmonics are added together and circulate within the delta loop. Hence, the relationship between the circulating currents in the delta winding and the harmonic content is the zero order triplen harmonics.

2.1.5 Circulating Currents

The zero sequence currents circulates within the delta loop, and are therefore often denoted as circulating currents. In Figure 2.4, the phenomena is visualized.
These circulating currents lead to increased heating and thus reduced performance as the power losses are a function of current. Even though the circulating current is induced by the triplen harmonics in the back-emf, there are several causes increasing the circulating current. Such causes are eccentric rotor and stator as well as asymmetric loading and phase balancing [4].

In [6], P. Pramod expresses an equation for the circulating current defined by the harmonics in the flux linkage as an extension of Faraday's law.

$$I_{cc} = -\frac{\Psi_h \omega_e n h}{\sqrt{R_s^2 + (h\omega_e(L - 2M))^2}} \tag{2.4}$$

Here, Ψ_h represents the magnet flux linkage harmonic multiple, h is the harmonic order, n is the number of phases, ω_e is the rotational speed in electrical radians, and the stator resistance R_s together with the self and mutual inductances L and M represents the impedance.

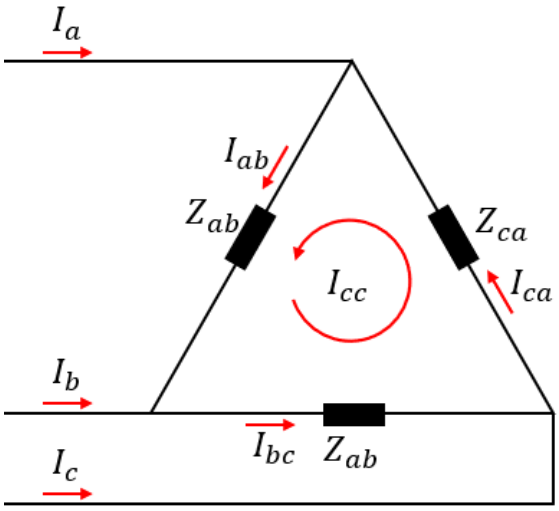

Figure 2.4: Circulating current in a delta connection

As the circulating current is a function of the resistance and the inductance, the circulating current will have a frequency dependency, hence a rotational speed dependency. This is shown in [6], where the magnitude changes with speed for low speeds but ceases to be impacted by speed variances in speeds stretching over 1000rpm. This is because the inductive component in the impedance becomes much larger than the resistive component with increased speed. In high speeds, the expression for the circulating current can therefor be reduced to,

$$I_{cc} = -\frac{\Psi_h n}{L - 2M} \tag{2.5}$$

Further, the flux linkage Ψ can be describe as a function of the flux density B_{airgap} in the air-gap making circulating current directly dependent on the air-gap flux harmonics. The expression can be stated as,

$$\Psi = B_{airgap} A_{airgap} \frac{N_s r p}{N_{parallel}} \tag{2.6}$$

where A_{airgap} is the air-gap area, N_s the number of turns, $N_{parallel}$ parallel branches. Number of winding layers r as well as pole pairs p needs to be taken into consideration.

Moreover, the most significant impact on the circulating current is the core saturation in the machine [4], [13], and [14]. The saturation impacts the inductance and rapidly decreases the impedance, which according to (2.5) makes the circulating current increase drastically with increased level of saturation. High circulating

currents will further impact the saturation, increase the machine temperature, and can have a severe effect on magnet demagnetization under peak load conditions [7], thus decreasing the machine performance.

2.1.6 Lenz's Law

Lenz's Law is a fundamental law of physics commonly seen in electric machines. It states that the direction of an induced current in a conductor due to a changing magnetic field is such that the induced current will create its own magnetic field, opposing the initial magnetic field that produced it.

In a delta connection, the zero sequence currents present in the windings, will produce its own magnetic field, opposing the initial field in the stator windings according to Lenz's Law. This is denoted as the minus sign in Faraday's Law from [14] as,

$$\Delta \times E = -\frac{\partial B}{\partial t} \tag{2.7}$$

Reducing the triplen harmonic amplitudes in the flux linkage will in turn reduce the triplen harmonic amplitudes of the back-EMF. In [15], a delta connected motor had slightly lower hysteresis losses compared to a wye-connected motor.

2.2 Permanent Magnet Synchronous Machine

The permanent magnet synchronous machine have various rotor topologies. Some are, the V-shaped, U-shaped and surface-magnet, seen in Figure 2.5a, 2.5b, and 2.5c, respectively.

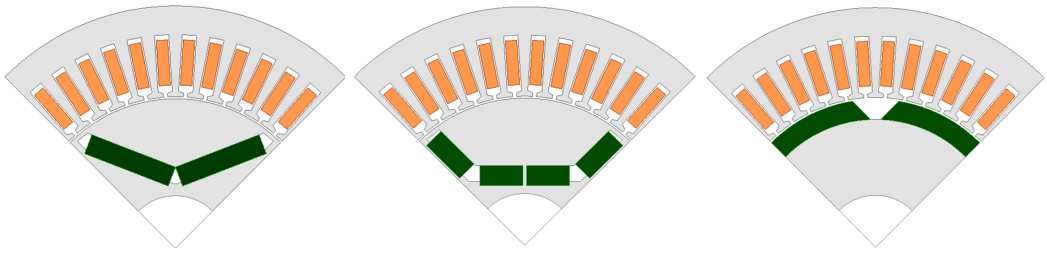

(a) V-shaped rotor design

(b) U-shaped rotor design

(c) Surface-magnet rotor design

Figure 2.5: Various rotor designs

The various topologies of PMSMs yield different traits. Efficiency stands as a cornerstone criterion, defining how the PMSM converts electrical input power to mechanical output power. Moreover, power density is another crucial consideration since it reflects on the overall cost of the machine. A PMSM with high power density enables more compact and lightweight rotor design, ultimately leading to space-saving and material reduction. Also, the ability of the rotor to suppress undesirable harmonic components in the generated magnetic flux is a key design aspect to minimize the

extensive heating and vibration caused by harmonics. Other factors such as demagnetization and environmental impact are equally crucial and are typically addressed through careful selection of magnet materials.

In recent years, the interior permanent magnet synchronous machine (IPMSM) has gained favor over the surface-mounted PMSM owing to several notable advantages. First, the IPMSM can reach higher speeds due to superior force withstand ability gained by the placements of the magnets. Moreover, interior magnets can yield more torque benefiting from the added reluctance torque generated from its salient attribute. Also, easier manufacturing processes since the process of gluing and magnet bending are simplified [16].

2.2.1 Saturation

Saturation occurs in ferromagnetic materials such as iron when the linear relationship between magnetic flux (B-field) and magnetic field strength turns (H-field) non-linear. When the B-field no longer increases linearly with the applied H-field, or the other way around. This phenomena can be clearly seen in a material BH-curve where the flattening occurs at high H-field magnitudes, visualized in Figure 2.6.

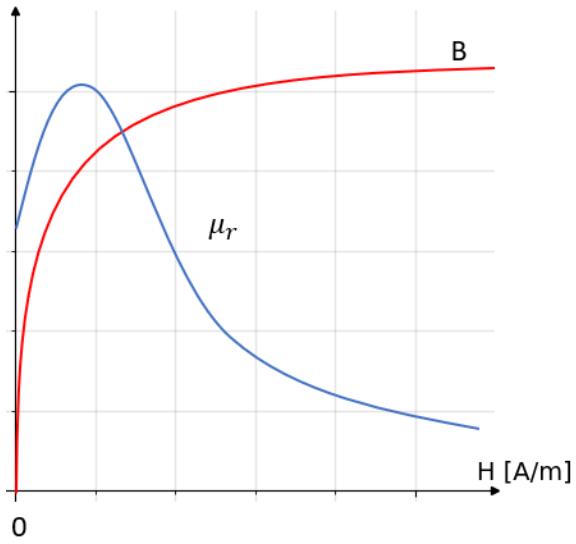

Figure 2.6: Saturation curve

In detail, when the flux density increases above the materialistic knee point, its relative permeability is heavily decreases resulting in an increased magnetic field strength since,

$$H = \frac{B}{\mu_0 \mu_r} \tag{2.8}$$

thus linkage of the flux gradually decrease. Consequently, at positive as well as negative peaks of the B-field the magnitude is reduced below the peak it would reach

considering ideally sinusoidal conditions. As the B-field is in direct correlation with the back-EMF seen in (2.7) the flattening of the B-field peak will be included in the back-EMF wave shape as well. Ultimately, this distortion-phenomena is leading to the triplen harmonic characteristic of the back-EMF wave shape. Further saturation will increase the triplen harmonics in relation with the reduced relative permeability [14].

Saturation impacts several aspects of the PMSM. The torque production is directly related to the magnetic flux generated by the stator and the interaction between the rotor magnets. Saturation limits the maximum flux density in the stator core thereby limiting the torque output.

2.2.2 Inductance

The PMSM has a inductive characteristic, therefor its inductive components are pivotal for its performance. Fundamentally, the inductance can easily be separated in two components. First the self-inductance explicitly defines the inductive property as a function of the machine design, specifically relating to the magnetic influence within an individual series of coils as,

$$L_s = \frac{N_{s1}^2}{\Re} \tag{2.9}$$

where N_{s1} represents one individual series of coils and $\Re$ is the reluctance.

With saturation, the inductive properties are decreasing rapidly as a function of the decreasing relative permeability of the saturated material, thus making the material reluctance increase leading to decreased inductance [14].

The second inductive component is the cross-coupled inductance, also defined by the design properties. However, the cross-coupled inductance referrers to the mutual inductive attributes between two individual series of coils as,

$$L_{cc} = \frac{N_{s1}^2 N_{sn}^2}{\Re} \tag{2.10}$$

where N_{sn} represents any second individual series of coils.

Moreover, the cross-coupling inductance can enhance the saturation effect as cross-saturation. This can be seen for high negative I_d currents, where the flux linkage in the Q-direction is affected. Hence, in accurate modelling the mutual inductive effects must be taken in to considerations as described in [17] as,

$$\Psi_d = L_d(I_d, I_q) + \Psi_m \tag{2.11a}$$
$$\Psi_q = L_q(I_q, I_d) \tag{2.11b}$$

2.3 V-shape rotor topology

The geometric design of a V-shaped rotor can vary in terms of shapes and configurations. Nonetheless, by establishing definitions for magnetic characteristics, it becomes possible to describe the primary electromagnetic attributes of such rotors. The rotor pole pitch is defined by the angular position between two consecutive magnetic poles in the rotor. It is mathematically described as $\frac{2\pi}{P}$, where P is the number of magnetic poles in the rotor. Furthermore, the magnetic pole arc, also known as rotor pole pitch angle, is the angular distance along the circumference of the rotor that is covered by a single pole. The ratio between the rotor pole pitch and the magnetic pole arc defines as the rotor pole coverage. Moreover, the pole angle denotes as the angle between two magnets of the same pole.

2.3.1 Harmonic content

The harmonic content produced by a electrical machine can be found in the back-emf waveform. Since the back-emf is generated as a function of the machine flux, the harmonic content can therefore be seen in the flux density of the air-gap, as described. There are several factors influencing the characteristics of the air-gap flux density in the V-shape rotor topology which in turn influence the harmonic content in the back-emf according to Faraday's law (2.7). The pole angle, relative width, and height of the permanent magnets have definitive influence over the air-gap flux density. The relative magnet width affects the flux magnitude, the height affects the inductance in the direct axis (D-axis), and the pole angle affects the harmonics in the rotor-generated flux density [18].

The textbook way of controlling the third harmonic content in the back-emf is to chose a specific winding pitch factor. However, when only considering the rotor topology the focus should be to control the level of saturation [14]. Naturally, the saturation level for the flux density should be as high as possible in order to ensure the highest possible force density, but also from an triplen harmonic perspective since it is highly influenced by the level of saturation. A core material with high saturation threshold is iron. Usually, a mixture of iron and silicon is used as core material since silicon reduces the iron losses, however the mixture decreases the saturation threshold. Consequently, a trade-off between saturation threshold and iron losses is needed [19].

2.3.1.1 Pole coverage

It can be considered well-known that a pole coverage of two-thirds of the rotor surface for a surface mounted PMSM suppresses the third harmonic multiples in the air-gap flux density [5]. This is evident when assuming the triplen harmonic is of sinusoidal heritage, the third harmonic will be a multiple of three

$$B_{airgap|3^{rd}} = \hat{B}sin(h\theta_e) \tag{2.12}$$

where $h = 3, 9, 15...$ and $\hat{B}$ is the magnitude of the air-gap flux density.

As the pole pitch stretches 180° for $\frac{1}{8}^{th}$ of a eight pole model as,

$$\theta_e = \frac{p}{2}\theta_m \tag{2.13}$$

two-thirds pole coverage will be 120°. Assigning $\theta_e = 120°$, the resulting air-gap flux density will be zero, for any h-third harmonic multiple.

$$B_{airgap|3^{rd}} = \hat{B}sin(3 \times 120) = 0 \tag{2.14}$$

However, for the V-shaped rotor topology the complexity increases. In [20] the theory of minimizing harmonic content in a V-shaped single magnet layer PMSM using analytical representation is presented. Using the theory, each magnetic flux generating segment in the rotor directly impacting the air-gap flux density is evaluated separately. As the V-shaped magnet alignment generates a trapezoidal flux density wave in the air-gap, the breakdown of each segment describes the wave, hence in-depth analysis of the harmonic content can be made.

In detail, the theory describes the relation between the magnet position and the wave shape, visualized in Figure 2.7, where the position of the magnet is divided into sections of angular pole coverage, measured in radians. One part magnet pole pitch in the V-shaped topology is equal to one half pole pitch $\frac{\pi}{P}$. Thereby also equal to the sum of the magnetic pole arc segments, α_1, α_2, and α_3.

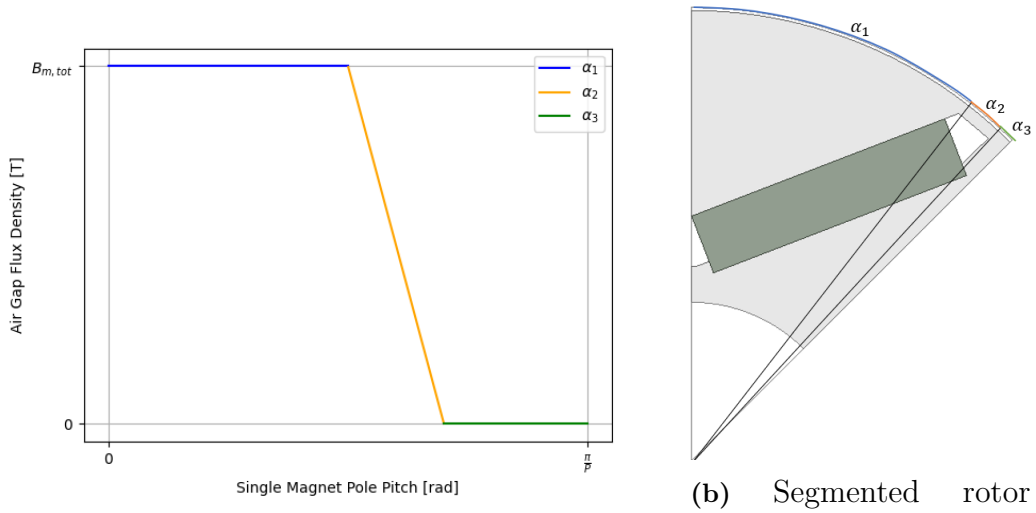

(a) Segmented air-gap flux density

(b) Segmented rotor model

Figure 2.7: Corresponding air-gap flux density in segmented rotor model

From angle 0 to α_1, it was assumed that the rotor reluctance is independent of the reluctance path length, and due to the very low reluctance value, as a factor of the high relative permeability in the rotor material, therefore neglected. This part could thereby be assumed to generate the square-shaped part of the trapezoidal wave flux density in the air-gap. The angular divisions were done in the rib of the magnet,

in the corners of the flux barriers, since it was assumed that the magnetic flux in the flux barrier is aligned with the flux of the magnet, thereby neglecting any magnetic flux leakage. This assumption was made concerning the increased reluctance within the flux barriers directly minimizing the magnetic flux leakage and reducing the saturation effects. In the rib, in segment α_2, seen in Figure 2.7a, the magnetic flux density gradually decreases along the angular length. The last section, α_3, has zero flux density within the air-gap, due to the opposing flux density generated from neighboring reversed-pole magnets.

The resulting analytical air-gap flux density as a function of the magnet position over one half pole pitch, is expressed from [20] as

$$B_{airgap} = \begin{cases} B_m & (0 \leq \theta < \alpha_1) \\ \frac{B_m}{\alpha_2}(\alpha_1 + \alpha_2 - \theta) & (\alpha_1 \leq \theta < \alpha_1 + \alpha_2) \\ 0 & (\alpha_1 + \alpha_2 \leq \theta < \alpha_1 + \alpha_2 + \alpha_3) \end{cases} \tag{2.15}$$

Moreover, the theory presents an analytical expression of the harmonic content in the air-gap flux density by the use of FFT. By implementing an expression of the harmonic content as a function of the magnetic pole arc the harmonic content based on the pole coverage segments can be analyzed from [20], according to

$$B_{m|h} = \frac{p}{\pi}\int_0^{a1} B_m cos(\frac{hp\theta}{2}) + \frac{p}{\pi}\int_{a1}^{a1+a2} \frac{B_m}{a2}(a1 + a2 - \theta)cos(\frac{hp\theta}{2}) \tag{2.16}$$

where, h denotes the harmonic order, θ is the angular position in relation to the pole pitch, and p is the number of poles.

2.3.1.2 Pole arc angle

Connected with the pole coverage is the pole arc angle. The angle is defined as the angle stretching across the outer arc between two magnets with the same orientation, Figure 2.8. As the angle is used in the permanent magnet rotor typologies to regulate the pole coverage it determines the specific space harmonics in the rotor to stator relation as it influences the magnetic flux path. In [21] the influence of pole arc angle is describes to impact the triplen harmonics and in [22] the optimal pole arc angle reducing the specific third harmonic was found for the analyzed model.

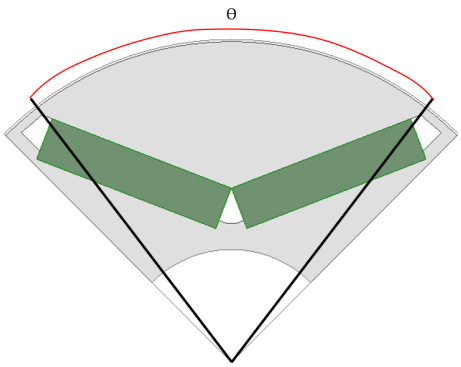

Figure 2.8: Magnet arc angle

2.3.1.3 Pole angle

The magnetic pole angle, often denoted as magnetic span angle, represents the angle between two magnet of the same orientation in the V-shaped geometry, Figure 2.9. The pole angle contributes to the air-gap flux density waveform. As the interaction between the magnets in the V-shaped pole depends on the distance between them, the concentration of magnetic flux intensifies with the decreased pole angle, consequently increasing the harmonic distortion in the air-gap flux density [23]. Therefore, adjustments of the pole angle will impact the sinusoidal degree of the air-gap flux density. Moreover, the pole angle impacts the relation between the inductances in direct and quadrant frame (DQ-frame), L_d and L_q, because the permeance in the quadrant axis (Q-axis) which is a factor of the magnetic flux path geometry, specifically the area and relative length of the flux path [23]. Also the permeance can be described as the inverse of reluctance

$$P = \frac{1}{\Re} = \frac{\mu A}{l} \tag{2.17}$$

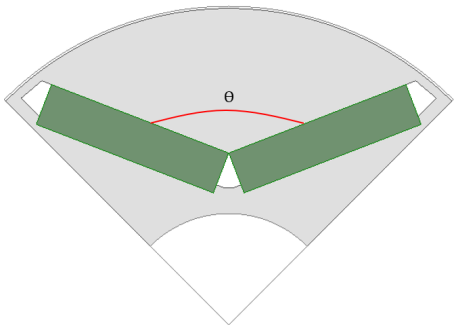

Figure 2.9: Magnet pole angle

2.3.1.4 Flux barriers

Flux barriers are used in permanent magnet machines to influence the path of the magnetic flux and thereby impact the waveform of the resulting air-gap flux density. By adjusting the geometry of the flux barriers the characteristics of the leakage flux can be altered ultimately influencing the harmonic content. The flux barriers have a much lower relative permeability ($\mu_r = 1$) than the iron core ($\mu_r \simeq 6000$ at 99.8% purity) in the rotor thus drastically increasing the local reluctance according to

$$\Re = \frac{l}{\mu_o \mu_r A} \tag{2.18}$$

Furthermore, rotor ducts are introduced in the rotor geometry to alter the concentration of magnetic flux in order to impact the level of saturation. Moreover, ducts can also be used for mechanical purposes. The most common mechanical purposes are cooling and reduction of material[24].

In terms of electromagnetic purpose, a rotor duct placed in a single or double V-shaped topology is often located in alignment with the D-axis, Figure 2.10.

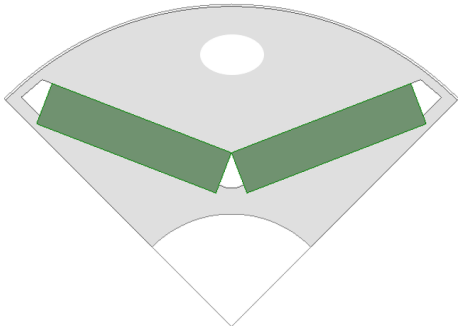

Figure 2.10: Rotor duct in D-axis

The duct, with air as material has a much lower relative permeability than the surrounding rotor iron. Consequently, the duct works as a magnetic flux barrier, hence the distribution and local concentration of magnetic flux changes in the D-axis due to the increased reluctance, in other words, the divergence flux is reduced.

2.4 Optimizing and statistical methods

This section covers the optimizing and statistical methods used. It begins with a description of the optimization method used for the analytical part, the 'scipy.optimize.minimize' function. Continuing with the presentation of the theoretical foundation of the Taguchi design methodology. Lastly, the statistical method analysis of variance (ANOVA) is presented, where the p-value and F-value metrics are described.

2.4.1 SciPy optimization

Optimization methods are often used to solve or give hints in complex mathematical problems. The 'scipy.optimize.minimize' function is part of the SciPy libray in Python, within the optimization module. The function utilizes various optimization algorithms, one of many are the Simplex algorithm is used in the Nelder-Mead method. The algorithm is well-suited for solving simple boundary-constrained optimization problems fast and in a robust manner. It utilized a heuristic search method and is used to find the maximum or minimum value of an objective function of several variables [25].

2.4.2 Taguchi design methodology

The Taguchi optimization method is a statistical technique developed by Genichi Taguchi for improving the quality of manufactured goods. It has since been widely applied in engineering, product design, and process optimization to achieve robust

and reliable products. The core of Taguchi's approach lies in the design of experiments (DOE) and the concept of robust design.

The main tool for the Taguchi optimization method is the orthogonal array (OA). An OA is a balanced array where all parameter levels are equally weighted. This in turns lead to each factor can be assessed independently from all other factors. This reduces time and cost as the effect from one parameter does not intervene with the estimation of the other parameters.

The user can use one of the predefined orthogonal tables given by the Taguchi method. Depending on how many factors, levels for these factors and if there are interactions or not [26].

Finite element analysis (FEA) can be very time consuming, especially with multi-objective goals and multiple adjustable parameters. The advantage of using the Taguchi method combined with FEA is the significantly reduced number of simulations. To conduct a Taguchi experimental design there are generally five steps that are followed:

1. Define parameters to be analysed, their constraints and the objective/s.
2. Select an OA based on number of parameters and their levels.
3. Using finite element method (FEM), simulate each run based on the OA and calculate the response variable/s.
4. Calculate the signal-to-noise ratio for each parameter and its levels.
5. Determine the best combination of the parameters.

The simulations in Ansys Maxwell will be conducted with the Taguchi method. For objectives that should be minimized. The SN ratio is calculated as,

$$Smaller\ the\ better\ S/N - ratio = -10 \log_{10} \left(\frac{1}{n} \sum_{i=1}^{n} y_i^2 \right) \tag{2.19}$$

where n is the number of simulations and y_i is the value for that simulation [26].

2.4.3 Analysis of variance

ANOVA is a statistical method used to analyze differences among group means in a sample. Its primary purpose is to test if the null hypothesis, which states that all group means are equal, holds true. This implies that any observed variation in the response variable among groups could be attributed to random chance rather than the effect of the independent variable. The null hypothesis is tested by calculating the p-value, which indicates the probability of observing the data, or something more extreme, if the null hypothesis were true. A p-value below 0.05 typically leads to rejecting the null hypothesis, suggesting that the group means differ in a statistically significant way, not attributable to random chance. Conversely, a high p-value suggests insufficient evidence to reject the null hypothesis, indicating no significant difference in means [27].

The F-value, another important metric in ANOVA, measures the ratio of the variance between groups to the variance within groups. It reflects how much the group means deviate from the overall mean relative to the variation within the groups. A higher F-value indicates a greater difference in means, suggesting significant variability between groups. Calculating both the p-value and F-value provides a comprehensive understanding of the data, allowing researchers to assess the significance and magnitude of differences between group means [27].

3
Case set-up

The case set-up of the thesis project will be divided into two cases. Analytical and numerical analysis, both based on an eight-pole DIPMSM with V-shaped rotor topology but with different complexity. First, in the analysis case, emphasis will be placed on expanding and assessing the analytical relationship with the third harmonic present in the air gap flux density and rotor pole arrangement. Subsequently, a numerical case will be established through FEM modeling to simulate the relevant parameters, saturation effects, and numerical optimization.

Finally, even though the main part of the study is aimed at the rotor parameters, a minor study of the stator saturation will be investigated to find the relationship between the triplen harmonic and the machine core saturation. The primary objective of the case set-up is to generate systematically organized data clarifying the dependency of circulating currents on the analyzed parameters, analytically and numerically.

3.1 Analytical case

The analytical case will generate the underlying foundation of the numerical case. First it will aim towards analyzing the third harmonic multiple contents in the air gap flux density, based on theory presented in section 2.3.1.1 but with an extension involving double magnet layers. The case is limited to only analyzing the third harmonic content in the air gap flux density as a function of the rotor pole coverage.

3.1.1 Model

The analytical analysis of the magnitude of the third harmonic in the air gap flux density as a function of the rotor pole coverage will initially be conducted on an eight-pole IPMSM. The IPMSM will be characterized by a single interior magnet layer and a V-shaped rotor topology, to validate the underlying theory. Subsequently, the analysis will be expanded to incorporate the complexity of a double magnet layer using the same rotor topology. It is important to note that this analytical focus is exclusively directed toward the rotor, with the stator assumed to be slotless for the purpose of this study. Furthermore, all materials in the model are considered linear, thus no saturation effect can occur. Also, the overall rotor parameters such as outer and inner rotor diameter, do not impact the solely theoretical calculation, hence they can be seen as arbitrary.

Figure 3.1 displays $\frac{1}{16}^{th}$ of the two models to be analyzed in the analytical case. The first magnet layer denoted as $L1$ represents the magnet closest to the rotor shaft, and the second layer $L2$ is the layer closest to the air gap.

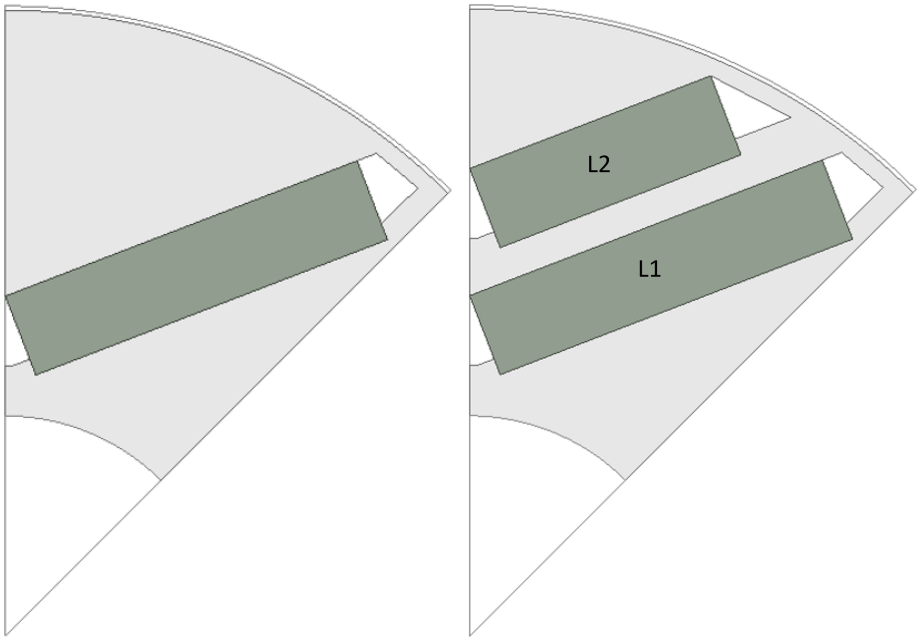

(a) Single magnet layer **(b)** Double magnet layer

Figure 3.1: Analytical model with different magnet layers

3.1.2 Segmented pole coverage method

The method to be used for the analytical relation between air gap flux density and pole coverage will be referred to as the segmented pole coverage method. The segmented pole coverage method will require segmentation of the pole pitch in order to find the relation of each magnetic flux generating part and the magnetic pole arc. This to discern the relationship between each magnetic flux-generating section and the magnetic pole arc.

The methodology involves a comprehensive analysis of the contribution made by the primary magnetic flux-generating segments within a magnetic pole. Since the length of each segment has an impact on the harmonic content, identifying optimal segmented lengths becomes crucial.

A segment is defined by a magnetic vector aimed toward the air gap. In other words, the magnetic flux vector is directed along the D-axis as can be seen in Figure 3.2a. Conversely, Figure 3.2b depicts a magnet with highlighted sides facing the air gap.

A single-layer magnet V-shaped pole, only considering half of the pole pitch representing $\frac{1}{16}^{th}$ of the IPMSM model, will have three segments. Thus, the double-layer

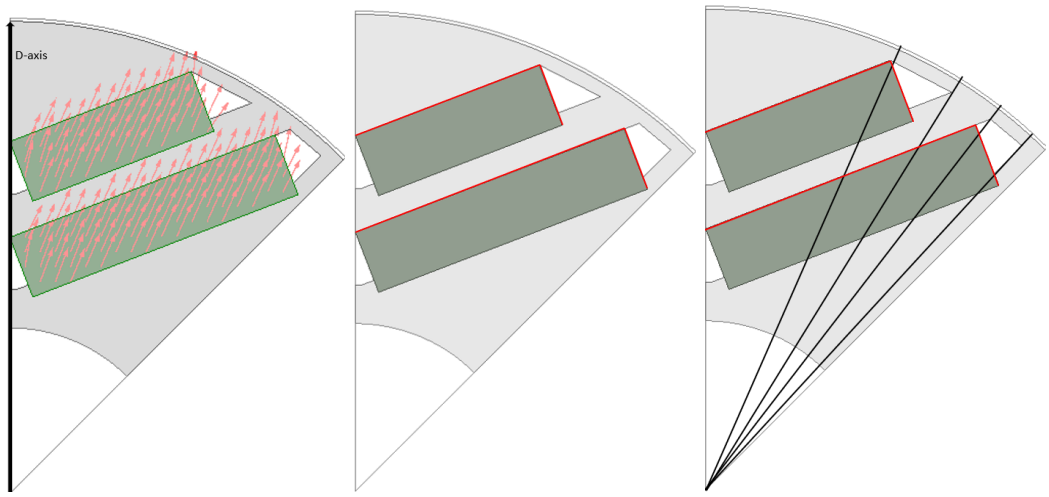

(a) Flux vectors in D-axis direction

(b) Highlighted flux-generating boundaries

(c) Magnetic flux segmentation lines

Figure 3.2: Magnetic flux segmentation

model will require five segments. By only segmenting one-half of the V-shaped pole, the number of segments is minimized, thereby also the number of calculations. This reduction is achievable due to the symmetrical geometry inherent in a V-shaped pole. This is highlighted in Figure 3.2c, which illustrates the magnet sides facing the air gap and delineates the resulting five segments.

Moreover, the computational process will entail iterative procedures using the Python programming language. The determination of segment boundaries will depend on the placement of magnets, ensuring the establishment of relevant limits for each segment.

To ascertain the optimal segment lengths that yield the minimal third harmonic content in air-gap flux density, an optimization algorithm will be employed. Specifically, the algorithm is a basic optimization function sourced from the scipy.optimize library, recognized as *minimize* in python. The theoretical ground of this optimization process is further described in section 2.4.1.

3.2 Numerical case

In contrast to the analytical case, where only one parameter is analyzed, the numerical case aims to analyze multiple parameters. This to find interactions between the parameters and which parameters have a significant impact on the third harmonic current amplitude. From this investigation, optimal rotor parametric values can be determined in terms of reducing the third harmonic amplitude and increasing robustness. In addition, analysis of saturation in the machine iron core will be made as a function of different D-and Q-currents.

3.2.1 Model

The numerical case involves the creation of a FEM DIPMSM model with a V-shaped rotor topology using Ansys Maxwell. The DIPMSM is commonly used topology in the automotive industry due to its high torque to weight ratio. The model is to be created as a Maxwell 2D design. The overall setup in Ansys Maxwell can be variate depending on the objective of the simulations. By selecting a solution type to be transient, dynamic simulations can be made. However, by selecting magnetostatic, static field simulations can be made. The numerical case will require both solution types.

Furthermore, the model is to be designed with the same principles as the analytical case model but with increased complexity to make it more realistic. The winding configuration will be single-layered full pitch with the number of slots per pole per phase equal to two. The winding is to be modeled as a hairpin type and the model is to be created with a focus on the parameters arranging the magnet positions in the rotor. Therefore the specific diameters and lengths are arbitrary for the purpose of the thesis. The relevant design parameters for the model are shown in Table 3.1.

Table 3.1: Model parameters

Parameter	Variable	Value	Unit
Number of series windings	N_s	8	-
Number of parallel windings	N_p	4	-
Number of poles	p	8	-
Number of stator slots	Q	48	-
Number of stator slots per pole per phase	q	2	-
Number of phases	n	3	-
Fill factor	k_{fill}	70	%
DC link voltage	V_{DC}	650	V
Current limit	I_{peak}	800	A

3.2.1.1 Material assignment

The materials can be found in the existing material library or defined by the user. The project model is to be built by combining the two methods. The materials in the model are copper for the coils, electric steel (M19-29G) for the rotor and stator core, and neodymium-iron-boron (N42UH) for the magnets. The shaft is to be modeled with stainless steel. The materials are commonly used in the automotive industry, such as in the 2004 Toyota Prius IPMSM.

3.2.1.2 Mesh Generation

To ensure the right accuracy of the simulation results as well as maximized computational efficiency in a FEM model, it is imperative to establish precise and well-defined mesh settings tailored to each element within the model.

The definition of mesh parameters, such as element size, shape, and refinement criteria, plays a central role in achieving reliable simulations. However, the selection of mesh needs to be a balance between accuracy and computational time. Given that the model will have areas that can contain high levels of magnetic flux density, it is paramount to define a finer mesh within these specific regions. A finer resolution is particularly significant for accurately computing saturation levels, being a critical factor in studying harmonics. In Table 3.2, the mesh settings for each element are displayed where the rotor bands are areas with potential high local saturation.

Table 3.2: Mesh

Part	Mesh type	Size	Surface deviation
Coils	Length based	3mm	-
Stator	Surface Approximation Based	-	0.1mm
Rotor	Length based	2mm	-
Rotor bands	Length based	0.5mm	-
Rotor shaft	Length based	10mm	-
Magnets	Length based	3mm	-
Rotor duct	Length based	0.5mm	-

3.2.1.3 External circuit

In order to conduct measurement on the circulating currents in Ansys Maxwell, an external circuit is to be created and added to the model. The external circuit will represent the delta connection and links with the active winding in the model. Therefore, calculations of the end winding parameters need to be conducted in order to obtain a realistic external circuit.

3.2.2 Simulations

The simulations will be divided into two sections covering analysis of saturation affecting the circulating current, as well as rotor parameter evaluation.

3.2.2.1 Saturation evaluation

Saturation analysis in the model involves injecting sinusoidal three-phase currents corresponding to distinct phase delays between the three-phase voltages and currents waveform. These phase delays are referred to the DQ-frame as magnitude ratios between the d-and q-axis current magnitude and represent typical load currents using maximum torque per ampere (MTPA), placing the load current in the second quadrant within the DQ-frame. The following phase delays are to be analyzed; $-30°$, $-45°$, and $-60°$. Figure 3.3 illustrates the ratios under examination as angles in the DQ-frame. It should be recognized that while this injection method may not precisely mirror realistic control scenarios, it effectively captures the saturation effect in the model, and enables the study of circulating currents.

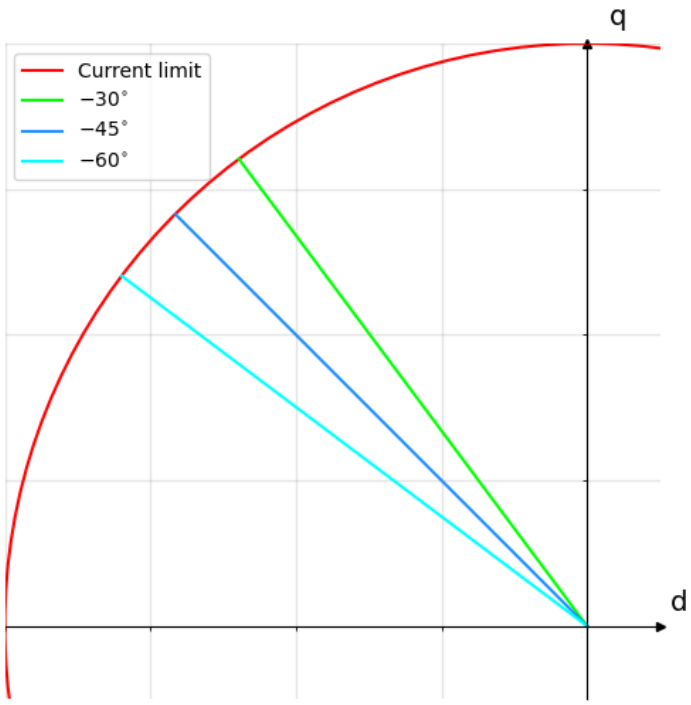

Figure 3.3: Input current magnitude ratios in DQ-frame

3.2.2.2 Parametric evaluation

The parametric simulations will feature eight adjustable rotor parameters. These are pole angle, arc pole angle, magnet thickness, and flux blocker extension length, for each magnet layer, visualized in Figure 3.4. These parameters represent the magnet flux generation in relation to the magnet layout. The arc pole angle will be measured in electrical degrees in relation to the pole pitch of 180 electrical degrees, whereas the magnet thickness and extension length are to be measured in mm. The pole angle will be measured in mechanical degrees.

The initial values can be seen in Table 3.3, where the individual parameter simulations are considered to provide the foundation for the boundaries in the optimization.

Table 3.3: Description of the parameters

Parameter	Description	Initial Value	Unit
$L1_{Ext}$	Flux barrier spacing extension	3.5	mm
$L2_{Ext}$	Flux barrier spacing extension	12.5	mm
$L1_{Arc}$	Magnetic arc angle	134	electrical degrees
$L2_{Arc}$	Magnetic arc angle	78	electrical degrees
$L1_{Pole}$	Magnet pole angle	92	degrees
$L2_{Pole}$	Magnet pole angle	120	degrees
$L1_T$	Magnet Thickness	4.2	mm
$L2_T$	Magnet thickness	3.2	mm

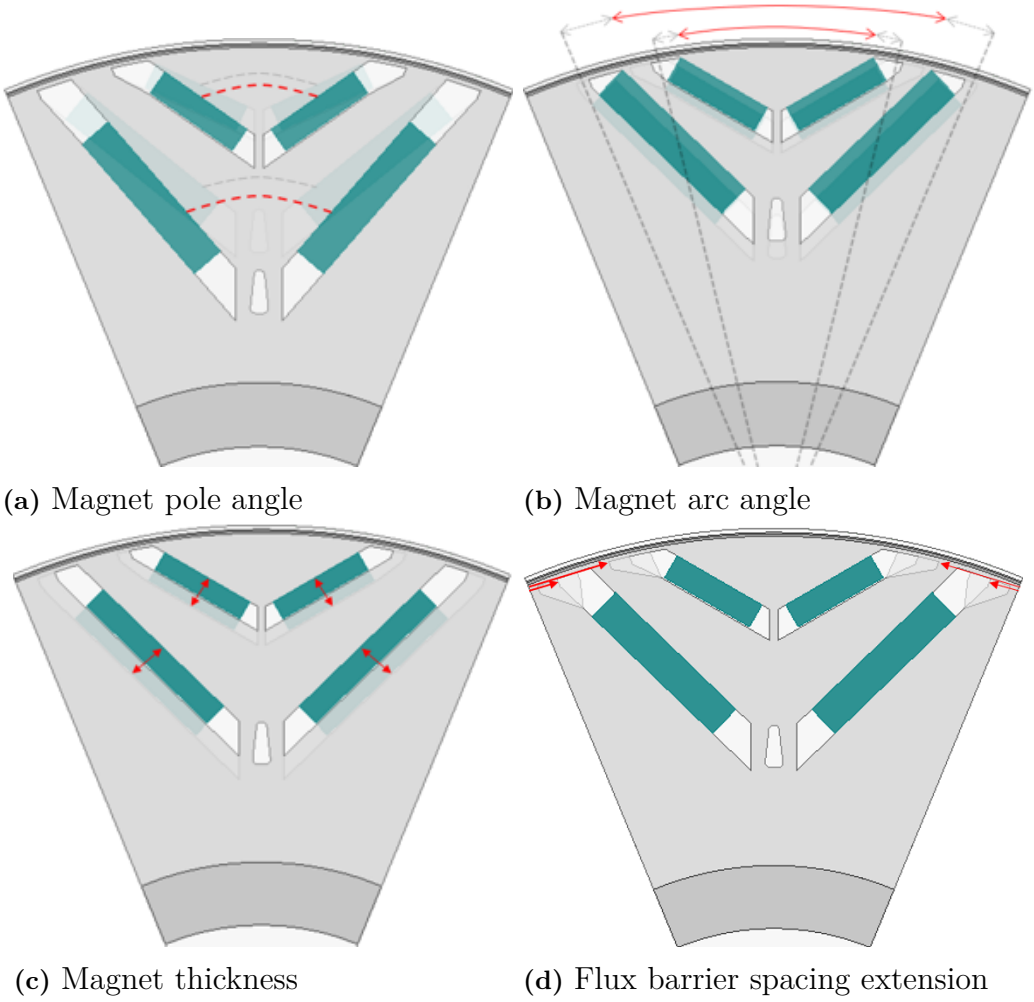

(a) Magnet pole angle

(b) Magnet arc angle

(c) Magnet thickness

(d) Flux barrier spacing extension

Figure 3.4: Visualisation of changeable parameters

Each parameter's impact on the circulating current is first simulated individually, then in pairs, to model accurate boundaries. Thereafter, an optimization of the combined impact of the mentioned parameters is computed. Generally, more than one Taguchi optimization method is conducted. Due to the fact that a large value difference between each level leads to reduced accuracy. By incrementing the levels to smaller values, the accuracy of the design experiment increases. The process can be viewed in Figure 3.5. The parametric simulations are to be done in no load condition in order to evaluate the result accurately by excluding as much saturation effect as possible.

3.2.3 Taguchi optimization method

In this study, the eight parameters are assigned with four different levels. An orthogonal array of 32 simulations and 4 levels $L_{32}(4^8)$ is used.

Reducing the orthogonal array to three level $L_{27}(3^8)$ array will only reduce com-

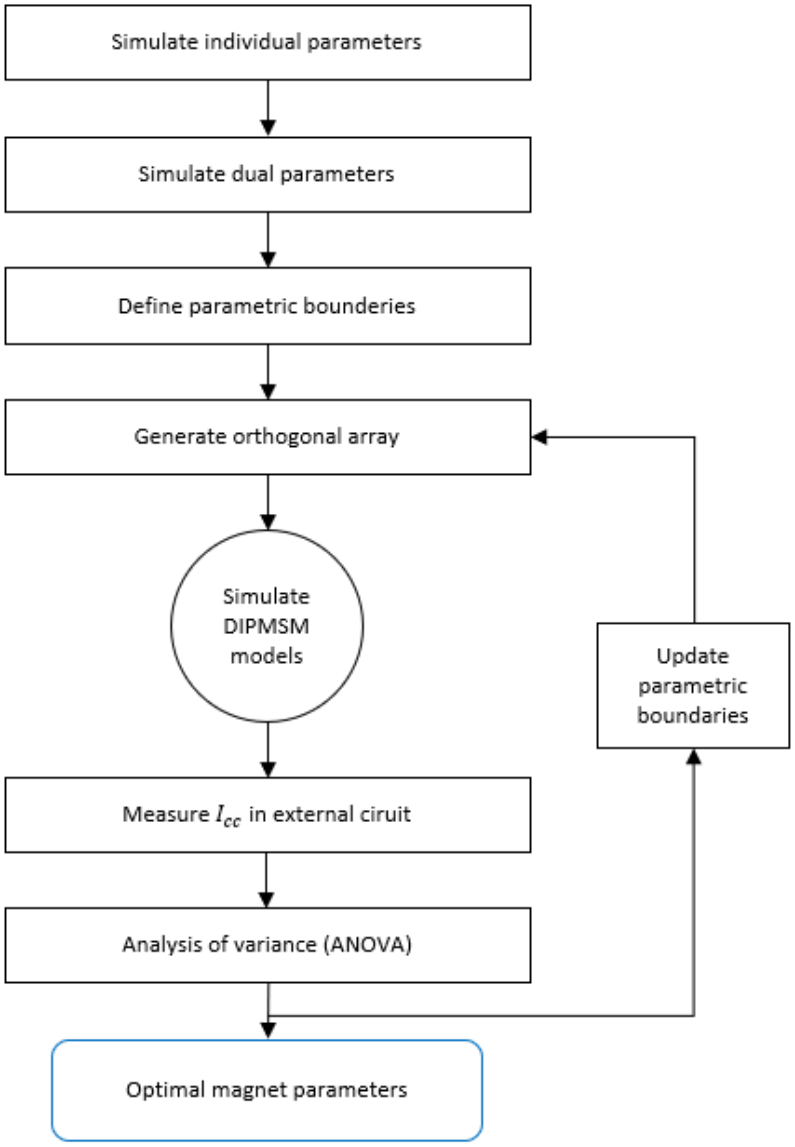

Figure 3.5: Parametric evaluation process

putational time by 15% while reducing the accuracy by 32%. Having a five-level orthogonal array like the $L_{54}(125^8)$ array would only increase the accuracy by 20% while the computational time would increase by 300%. The $L_{32}(4^8)$ is therefore considered the right choice in this case, taking both accuracy and simulation time into consideration. The process of determining the boundaries and levels is explained in subsection 3.2.2.2.

In this case, where 4 levels and 8 parameters are used, a full factorial would require $4^8 = 65\,536$ simulations. While using the orthogonal array $L_{32}(4^8)$ reduces this number down to 32 simulations. This saves the amount of computational time required by around 99.95 %.

Since the objective is to reduce the circulating currents, Equation (2.19) will be

used, provided in section 2.4.2.

3.2.3.1 Analysis of variance

After the Taguchi optimization method has been conducted, an ANOVA of the result will be carried out to find the most significant parameters impacting the circulating currents. The ANOVA will also be used to find potential interaction effects between parameters.

3.2.4 Rotor duct analysis

Once the model is optimized for the mentioned parameter using the Taguchi method, further machine design is to be analysed by introducing a rotor duct. This to evaluate the effect of the permeance in the D-axis direction on the induced circulating current. The duct will be shaped as an ellipse and its major radius will be swept to analyze the effect of change in circulating current.

4
Analytical Analysis

The analytical calculations were conducted with the usage of the Segmented pole coverage method. The method originates from [20] and is described in section 3.1.2.

Moreover, it is noteworthy that one pole pitch corresponds to the angular length of $\frac{2\pi}{8}$ for the magnetic pole arc. Consequently, one half pole pitch represents an angular length of $\frac{\pi}{8}$, given that the model comprises eight poles. In the analysis, one half-pole pitch was considered equivalent to 100% pole coverage. This choice was motivated by the fact that, while one half-pole pitch necessitates fewer calculations, it yields the same results owing to the symmetrical nature of the model.

4.1 Single magnet layer

First, the model presented in section 3.1.1, Figure 3.1a, was analyzed. The harmonic content in the air-gap flux density could be calculated using (2.16) from section 2.3.1.1. Since the model has eight poles the equation formulates as,

$$B_{m|3} = \frac{8}{\pi}\int_0^{\alpha_1} B_m cos(\frac{3\times 8\times\theta}{2}) + \frac{8}{\pi}\int_{\alpha_1}^{\alpha_1+\alpha_2} \frac{B_m}{\alpha_2}(\alpha_1+\alpha_2-\theta)cos(\frac{3\times 8\times\theta}{2}) \quad (4.1)$$

By assigning boundaries for the angular length of the magnetic pole arc segments, it was possible to calculate the third harmonic content for the pole coverage. When the pole coverage is equal to one, the largest possible magnetic pole arc of $\frac{\pi}{8}$ is obtained, suggesting the upper boundary of α_1, at 100% pole coverage. The lower boundary of α_1 was selected to be an arbitrary limit of $\frac{\pi}{40}$ representing 20% pole coverage. As for α_2, it is a function of the flux barrier width, since the flux density goes from high to low along the barrier. Its limits were defined to be from $\frac{\pi}{40}$ to $\frac{\pi}{320}$ magnetic pole arc length. It is clear that segment α_1 never will reach an pole coverage of 100% since α_2 will always be greater than 0, thereby an specified upper limit will not be necessary. The amplitude of the flux density produced by the magnets B_m was set to 1 T in the analytical calculations, representing a nominal value. In Table 4.1, the defined boundaries are displayed.

The resulting dependence of the segment arc length as a function of the magnitude of the third harmonic content in the air-gap flux density for both α_1- and α_2-segment are displayed in Figure 4.1a and 4.1b respectively.

Table 4.1: Pole coverage for each segment

Segment	Min coverage [%]	Max coverage [%]
α_1	20%	100%
α_2	2.5%	20%

Importantly, 4.1a represents the first sums of (4.1) where only the dependence of α_1 is considered. Nevertheless, 4.1b represent the second sums of (4.1), where both α_1 and α_2 are considered.

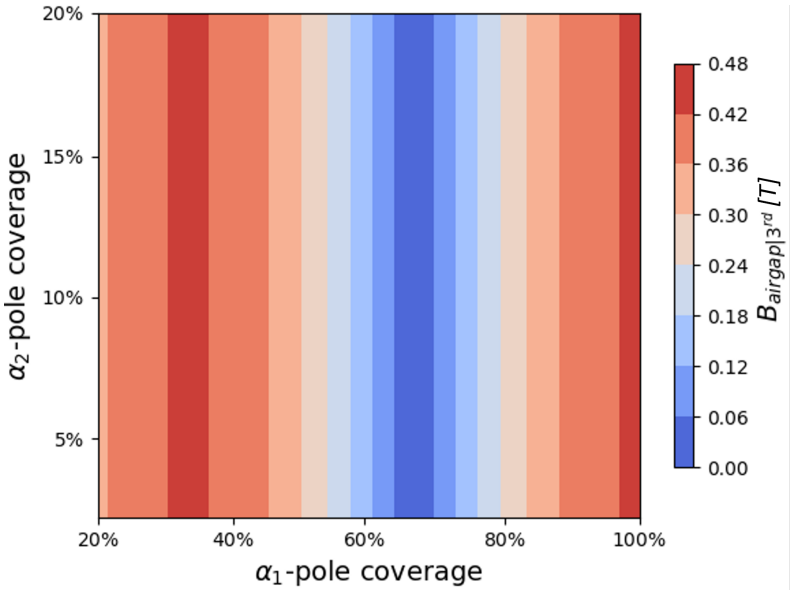

(a) α_1-segment relation to $B_{airgap|3^{rd}}$

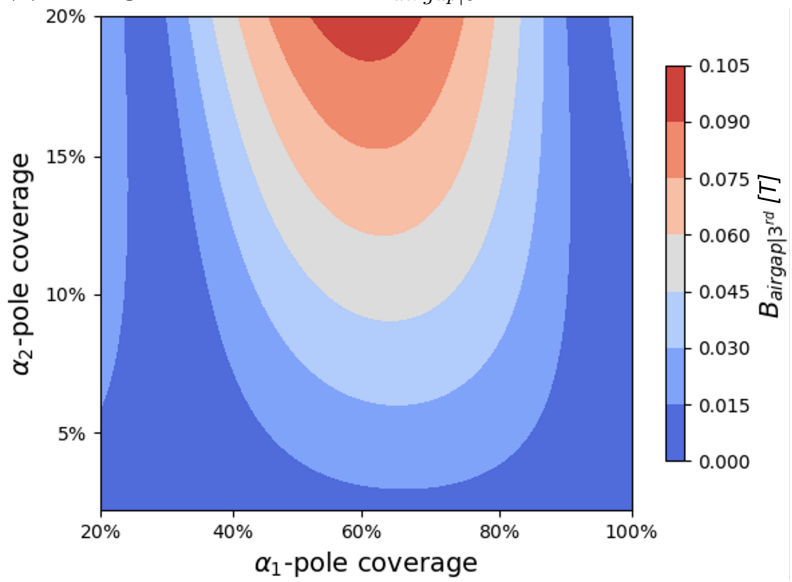

(b) α_2-segment relation to $B_{airgap|3^{rd}}$

Figure 4.1: Individual segment relation to $B_{airgap|3^{rd}}$

Furthermore, Figure 4.2 shows the absolute value of the combined sum of equation (4.1), describing the third harmonic content in relation with the segmented pole coverage.

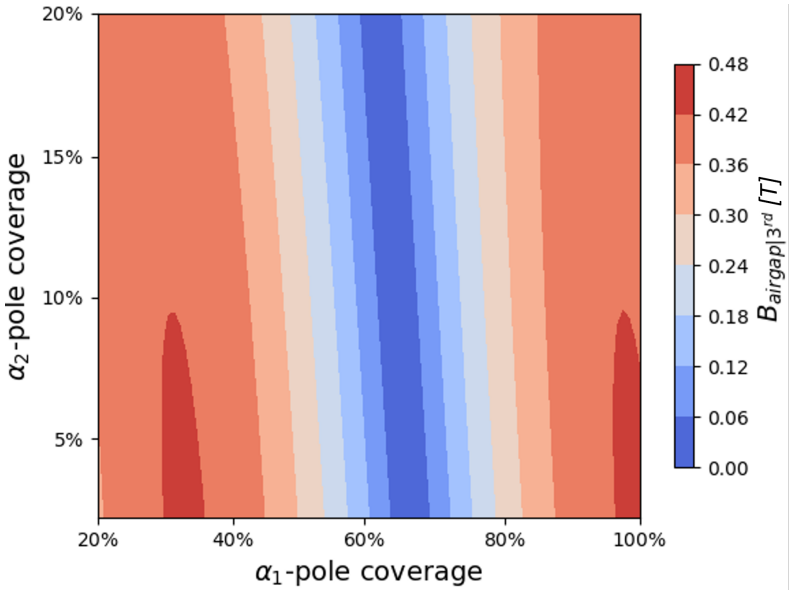

Figure 4.2: Combined segment relation to $B_{airgap|3^{rd}}$

In addition, the third harmonic content closest to zero for the combined segments was calculated with the implemented optimization algorithm resulting in a total third harmonic contribution $B_{m|3} = 2.684 \times 10^{-5}\ T$ with an optimal segment distribution in Table 4.2, where the sum of the segments is equal to the pole pitch.

Table 4.2: Optimal segment distribution

Pole arc segment	Pole coverage [%]
α_1	64.61%
α_2	8.26%
α_3	27.13%

As mentioned, the triplen harmonic content in the air-gap flux density produced in a surface-mounted PMSM can be minimized by arranging the magnets with a pole coverage of 120 deg_e. This was also shown in the result of the analytical calculations for one magnet layer, as the zero-crossing occurred at 120 deg_e (66.67 %) pole coverage for the α_1 segment, seen in Figure 4.1a. It replicates a surface-mounted magnet since the reluctance in the rotor was neglected in the analysis.

However, for the V-shaped rotor topology, the width of the flux barriers impacted the α_2 segment. The resulting combined pole coverage exceeded 120 deg_e, as expected due to the contribution from the gradient magnetic flux caused by the flux barriers.

4.2 Double magnet layer

With two magnet layers, the complexity of the analytical expression for the air gap flux density increases. By using the same method as for one magnet layer, one half pole pitch was instead divided into five segments, Figure 4.3.

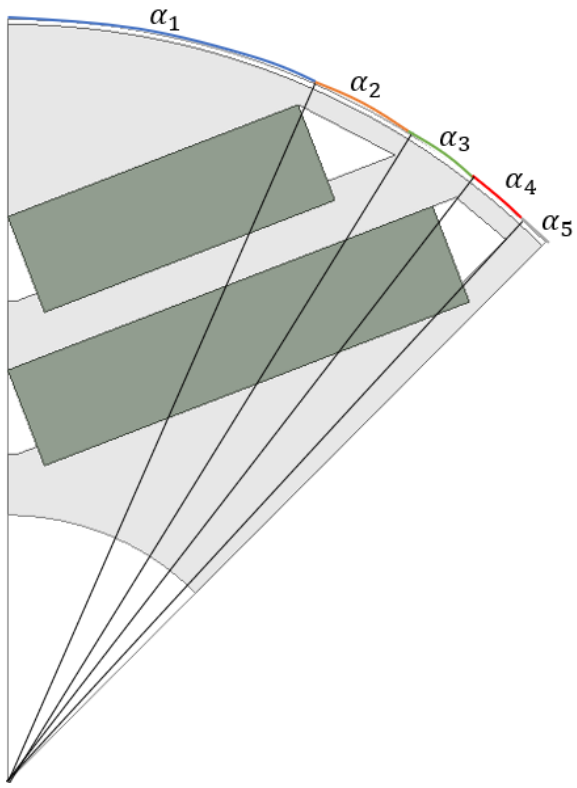

Figure 4.3: Segmented pole coverage

As the expression for the harmonic content in the air-gap flux density presented in the theory only covers a single magnet layer, it needed to be extended. With the segmented pole coverage method, the amplitude of the air-gap flux density per segment could be expressed for the double magnet layer model as,

$$B_{airgap} = \begin{cases} B_{m1} + B_{m2} & (0 \leq \theta < \alpha_1) \\ \frac{B_{m1}+B_{m2}}{\alpha_2}(\alpha_1 + \alpha_2 - \theta) & (\alpha_1 \leq \theta < \alpha_1 + \alpha_2) \\ B_{m1} & (\alpha_1 + \alpha_2 \leq \theta < \alpha_1 + \alpha_2 + \alpha_3) \\ \frac{B_{m1}}{\alpha_4}(\alpha_1 + \alpha_2 + \alpha_3 + \alpha_4 - \theta) & (\alpha_1 + \alpha_2 + \alpha_3 \leq \theta < \alpha_1 + \alpha_2 + \alpha_3 + \alpha_4) \\ 0 & (\alpha_1 + \alpha_2 + \alpha_3 + \alpha_4 \leq \theta \leq \alpha_1 + \alpha_2 + \alpha_3 + \alpha_4 + \alpha_5) \end{cases} \tag{4.2}$$

and visualized in Figure 4.4.

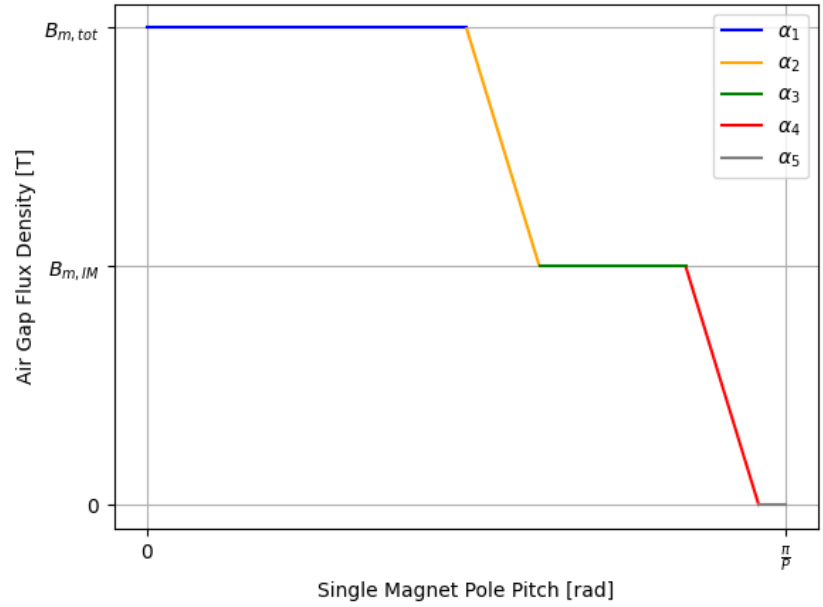

Figure 4.4: Analytical air-gap flux density over pole arc segments

Moreover, each component in (4.2) shapes the air-gap flux wave shape in different ways, to analyze the impact from the components, they were calculated with different values and visualized with respect to the pole pitch. First as a function of the magnet layer thicknesses B_{m1} and B_{m2} in three separate cases indicating its specific impact in Figure 4.5, while the segments were kept unchanged for each separate case.

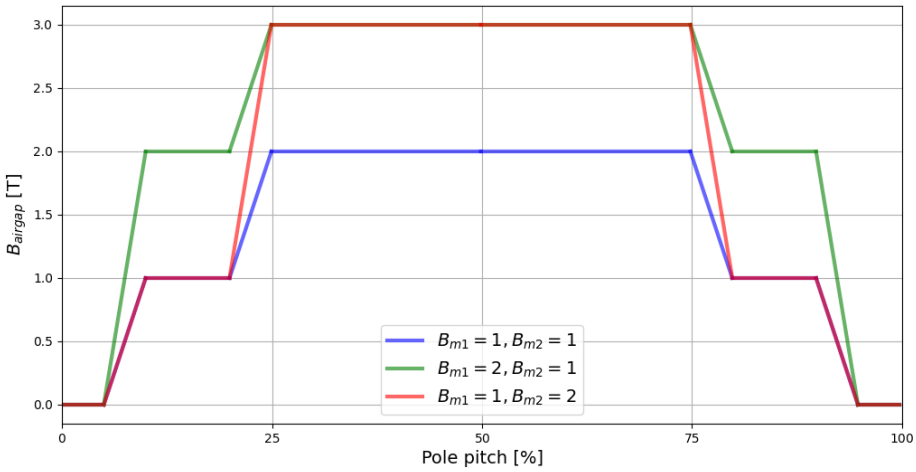

Figure 4.5: Magnet layer thickness ratio - wave shape impact

In Figure 4.6, the impact of the width of segments α_1 and α_3 were visualized as the other segments and amplitudes were kept unchanged. As can be seen, this were heavily impacting the width of the wave.

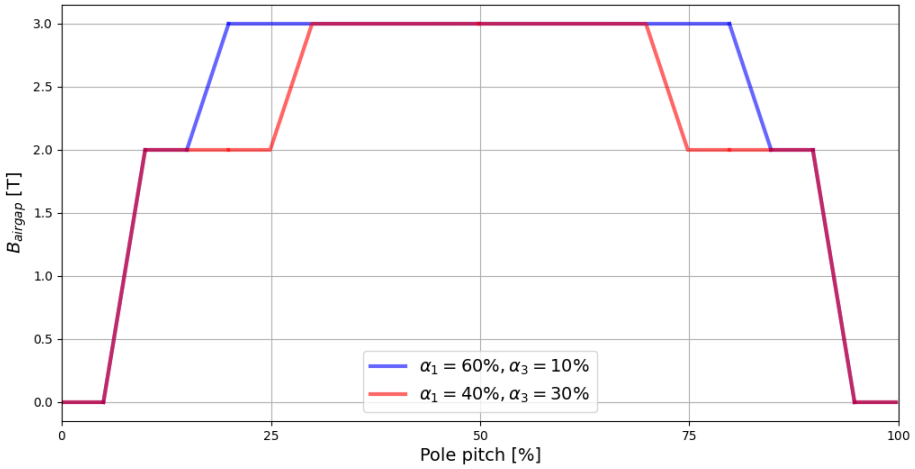

Figure 4.6: α_1 and α_3 ratio - wave shape impact

Lastly, in Figure 4.7, the impact of the segments α_2 and α_4 can be seen affecting the trapezoidal slops. Here, the other segments and amplitudes were kept unchanged.

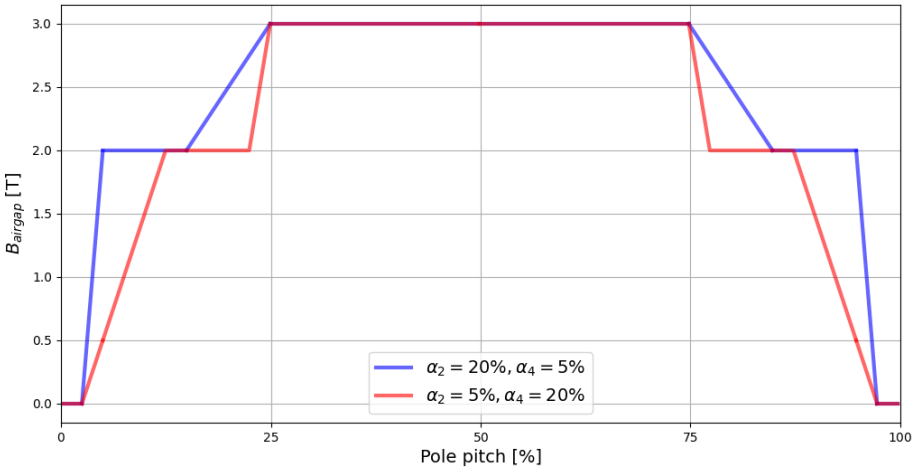

Figure 4.7: α_2 and α_4 ratio - wave shape impact

The harmonic content per segment could be calculated using FFT, thereby transforming the sum of the harmonics as,

$$\begin{aligned} B_{airgap|h} &= \frac{p}{\pi}\int_{0}^{\alpha_1}(B_{m1}+B_{m2})\,cos(\frac{hp\theta}{2}) \\ &+ \frac{p}{\pi}\int_{\alpha_1}^{\alpha_1+\alpha_2}\frac{B_{m1}+B_{m2}}{\alpha_2}(\alpha_1+\alpha_2-\theta)\,cos(\frac{hp\theta}{2}) \\ &+ \frac{p}{\pi}\int_{\alpha_1+\alpha_2}^{\alpha_1+\alpha_2+\alpha_3}B_{m1}\,cos(\frac{hp\theta}{2}) \\ &+ \frac{p}{\pi}\int_{\alpha_1+\alpha_2+\alpha_3}^{\alpha_1+\alpha_2+\alpha_3+\alpha_4}\frac{B_{m1}}{\alpha_4}(\alpha_1+\alpha_2+\alpha_3+\alpha_4-\theta)\,cos(\frac{hp\theta}{2}) \end{aligned} \quad (4.3)$$

where, h denotes the harmonic order, θ is the angular position in relation to the pole pitch, and p is the number of poles. In the double magnet layer calculations,

segments α_1 and α_3 were much larger than segments α_2 and α_4, hence the second and fourth sums of (4.3) were neglected. This since they are having a much lower impact on the resulting air-gap flux. It is also making it easier to visualize since the number of dimensions decreases to three instead of five.

The first and third parts of (4.3) are represented visually in Figure 4.8a and 4.8b respectively. The figure displays the amplitude of the third harmonic content in the air-gap flux density, $B_{airgap|3^{rd}}$, as a function of pole coverage for the α_1- and α_3 segment.

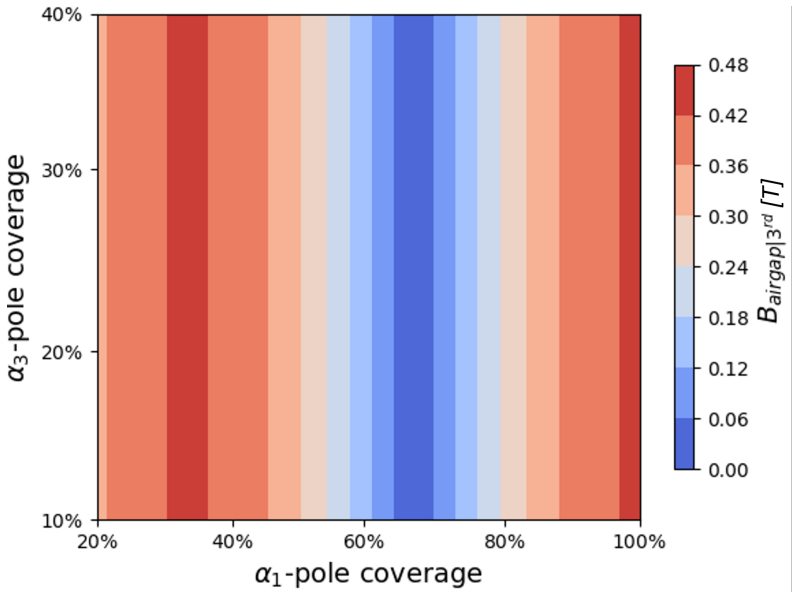

(a) α_1-segment relation to $B_{airgap|3^{rd}}$

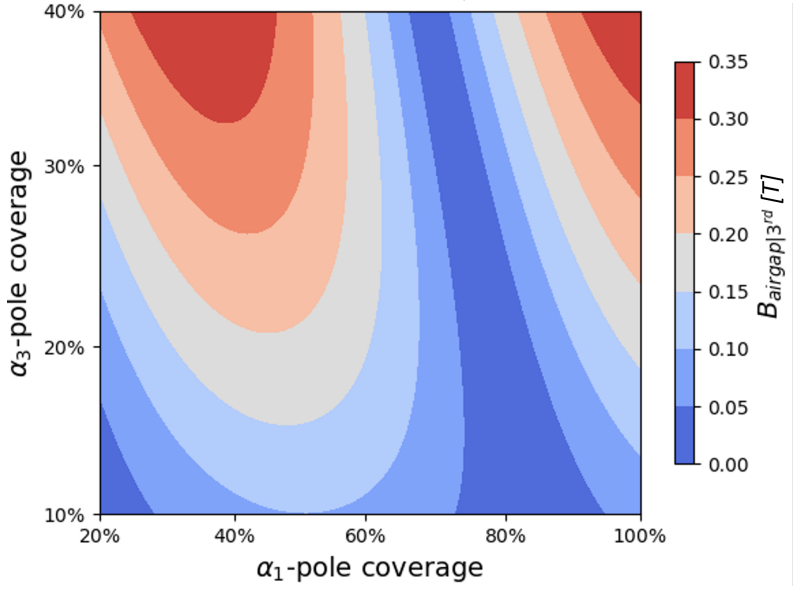

(b) α_3-segment relation to $B_{airgap|3^{rd}}$

Figure 4.8: Individual segment relation to $B_{airgap|3^{rd}}$

In addition, Figure 4.9 shows the absolute value of the combined amplitude of the

third harmonic content in relation to α_1- and α_3-segment.

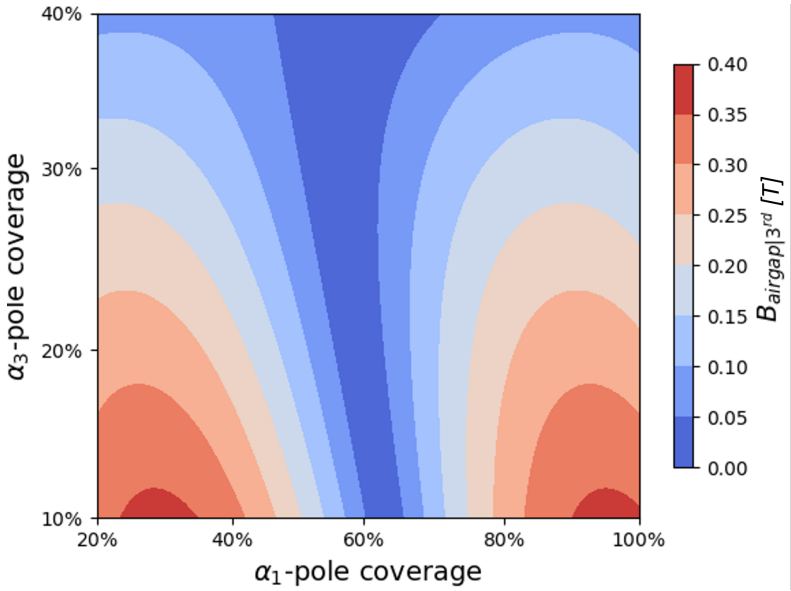

Figure 4.9: Combined segment relation to to $B_{airgap|3^{rd}}$

The result indicates that the magnetic pole arc of the α_1 segment had the greatest impact on the third harmonic content in the air-gap flux density. This was due to it was covering the largest part of the pole pitch, as well as inducing the highest amplitude of the air-gap flux density. The resulting Figures 4.8a and 4.8b as well as 4.9 are showing the magnitude of the flux density. Thereby, as seen when comparing the lowest values generated from each part of the sum with the total sum, it is clear that the total sum is lower than some parts of the sum, since the magnitude does not show weather the value is positive or negative.

In addition, a minimization solution was made. The expression for two magnet layers, with the increased amount of changeable dependent parameters in (4.3) requires mathematical optimization in order to find the value closest to zero including all five segments.

An optimization algorithm extended for the model was used to solve the complex optimization. In the algorithm, the implemented boundaries displayed in Table 4.3 were assumed as reasonable boundaries for the magnets to fit within the pole pitch in a V-shape rotor topology.

Table 4.3: Pole coverage for each segment

Segment	Min coverage [%]	Max coverage [%]
α_1	20%	100%
α_2	8%	20%
α_3	10%	40%
α_4	8%	20%

The objective function of the optimization was the function (4.3) where each component in the sum had the mentioned specified boundaries. In Figure 4.10, each objective function value per iteration can be seen from the heuristic search in Table 4.4.

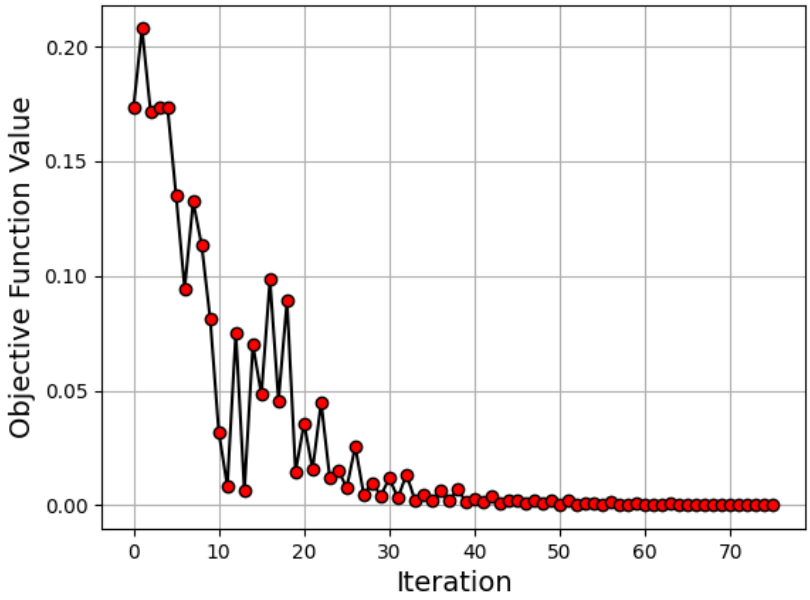

Figure 4.10: Objective function value per iteration

The solution for the optimal segment pole coverage for each segment can also be seen in Table 4.4. This combination was resulting in $B_{m|3^{rd}} = 4.92 \times 10^{-5}T$, where the sum of the segments is equal to the pole pitch.

Table 4.4: Optimal segment distribution

Pole arc segment	Pole coverage [%]
α_1	52.70%
α_2	8.87%
α_3	20.67%
α_4	8.47%
α_5	9.29%

The optimal segment distribution could be found exceeding 120 deg_e (66.67%) pole coverage and resulting in 163 deg_e (90.5%) pole coverage. This was due to the contribution of magnetic flux from both magnet layers as well as the gradient magnetic flux outside of the flux barriers generated different flux magnitudes along the pole pitch. The air-gap flux density wave shape formed by the optimal segment distribution could be visualized in Figure 4.11.

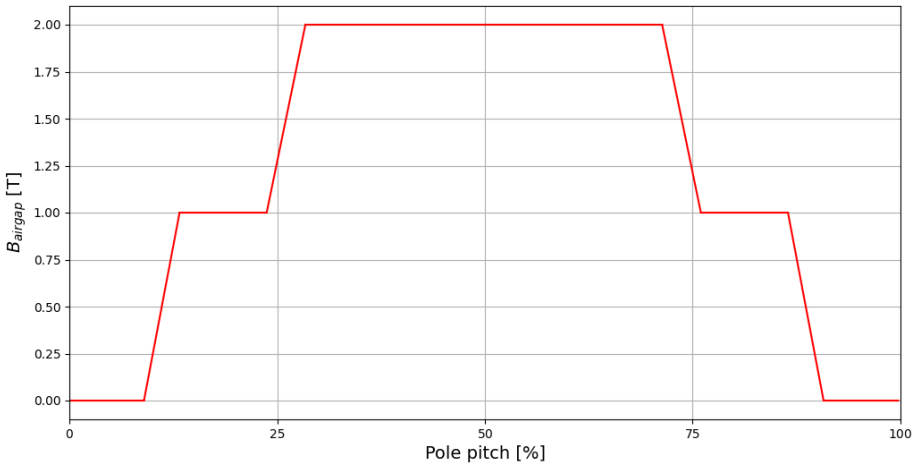

Figure 4.11: Analytically optimized air-gap flux density wave shape

5

Numerical Analysis

In this section, the numerical analysis is presented as well as the corresponding results. First the model was built using FEM in Ansys Maxwell. Thereafter, the characteristics of the model were analyzed, followed by a detailed analysis of the core saturation. Then, the rotor parametric evaluation was also computed together with an optimization.

5.1 Model

The model used in the numerical case was built using the existing RMxprt-template design tool in Ansys Maxwell. The option SlotCore was used for the stator geometry and VPMcore for the rotor geometry. The shaft was drawn using the center point arc option. By reducing the model symmetrically to one magnetic pole, resulting in $\frac{1}{8}th$ model, the computational time could be significantly reduced. In addition, a flux barrier was positioned between the first layer magnets in order to minimize the local flux leakage. Moreover, the model was built with multiple rotor bands increasing the mesh in highly saturated areas. This to increase the accuracy of the FEA. The model is displayed in Figure 5.1.

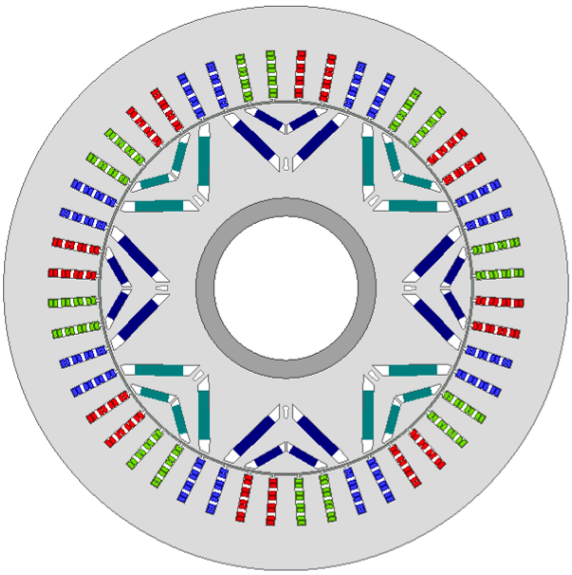

Figure 5.1: Complete DIPMSM

The resulting mesh of $\frac{1}{8^{th}}$ part model can be seen in Figure 5.2. As can be seen, the mesh grid is significantly finer along in areas where saturation are commonly occurring and expected.

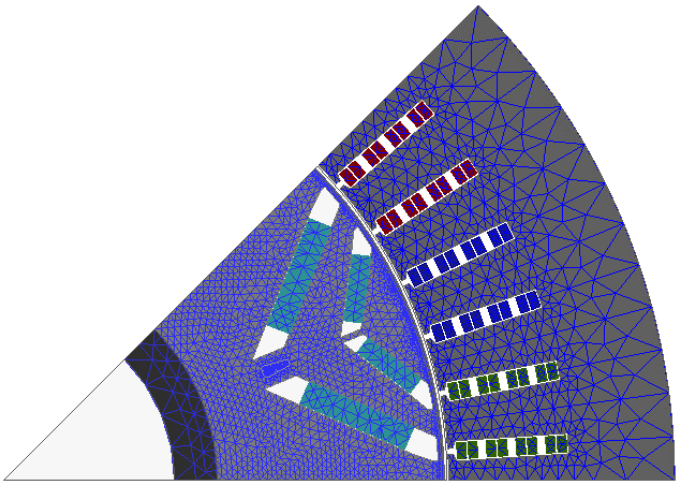

Figure 5.2: Resulting mesh grid of $\frac{1}{8^{th}}$ model

5.1.1 External circuit

The circulating currents in the model, an external circuit was built to represent the delta connection to allow for measuring. The model presented in Figure 5.1, was built in Maxwell2D, hence the end winding resistance was not taken into consideration. Therefore, an estimation of the end winding resistance was calculated using (5.1)-(5.4).

$$L_{ew} = 2(1.2L_{pitch} + 2L_{endext}) \tag{5.1}$$

Here L_{pitch} is calculated using the radius of the center of the stator slot together with the number of poles N_p as,

$$L_{pitch} = \frac{2\pi r_{slotcenter}}{N_p} \tag{5.2}$$

The resulting end winding resistance was calculated using the resistivity of copper ρ_{cu} and the winding configuration as

$$R_{coilext} = \frac{\rho_{cu} N_s L_{ew}}{A_{coil}/N_s} \tag{5.3}$$

where A_{coil} equals the product of the coil area and the fill factor, N_s is the number of series connected coils, and q is the number of slots per poles per phases, resulting in

$$R_{ew} = \frac{R_{coilext} N_p q}{2N_p^2} = 3.10\ m\Omega \tag{5.4}$$

The estimation is based on an assumed end winding overhang L_{endext} of 25mm. The end winding resistance is implemented in the circuit as R_{end} in Figure 5.3. Furthermore, the circuit is fed by three separated current sources to mimic a balanced three phase source. Each current source can be regarded as ideal due to its parallel connected high omic resistor.

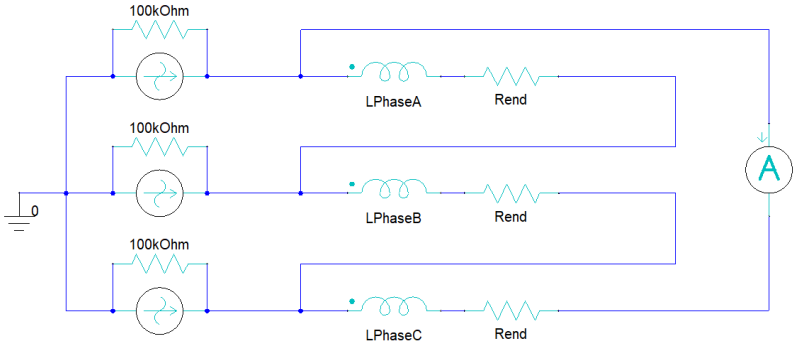

Figure 5.3: External circuit

The sources produces ideal sinusoidal waves and were chosen as load current for two reasons. First, they will saturate the material implemented in the model. Second, the ideal waves makes it easy to extract harmonic content, to be more precise, the triplen harmonic content. For the purpose of the analysis, the current sources were set to generate maximum 800 A, representing the maximum line current. The maximum phase current could then be determined as,

$$I_{max\ phase} = \frac{I_{max\ line}}{\sqrt{3}} = 461.8\ A \tag{5.5}$$

5.2 Model characteristics

The rotor in the model is characterized by the parameters presented in section 3.2.2.2. The initial values for the parameters are presented in Table 5.1 and showed in Figure 5.4. The magnet pair closest to the rotor shaft is noted as the first layer or $L1$, whereas the magnet pair furthest from the rotor shaft is noted as the second layer or $L2$.

First, the model was simulated under no load condition at several speeds using the initial set of values for the changeable parameters. This was done to analyze the speed dependence of the circulating current. Figure 5.5 shows that the speed has an impact on the circulating current magnitude in lower speed region. However at higher speeds it ceases to impact the magnitude, in accordance with theory presented in section 2.1.5. Therefore, 3000rpm is selected to be the speed used for the numerical analysis as it provides a good representation for the circulating current.

Table 5.1: Initial rotor parameters

Parameter	Value	Unit
$L1_{Ext}$	3.5	mm
$L2_{Ext}$	12.5	mm
$L1_{Arc}$	134	deg_e
$L2_{Arc}$	78	deg_e
$L1_{Pole}$	92	deg
$L2_{Pole}$	120	deg
$L1_T$	4.2	mm
$L2_T$	3.2	mm

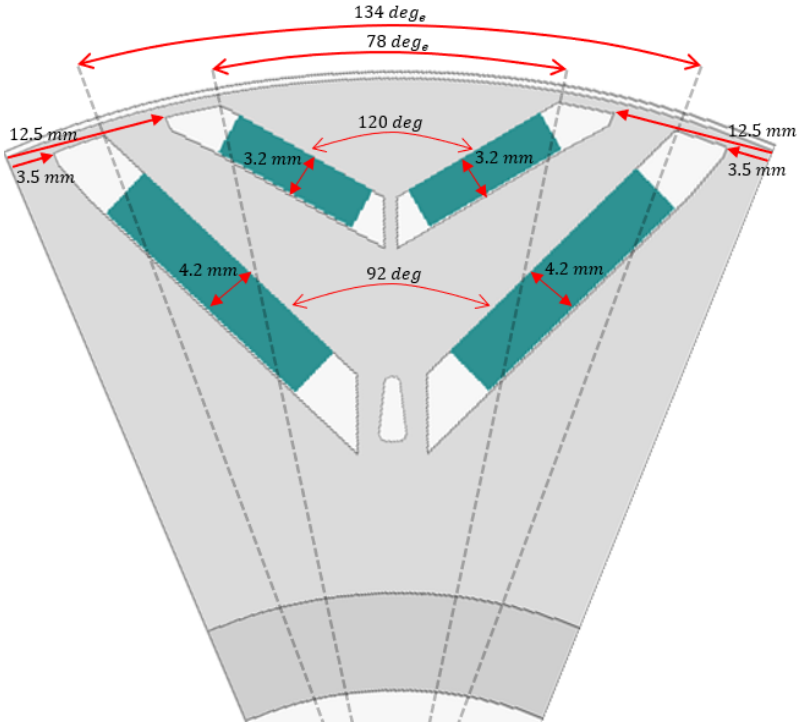

Figure 5.4: Initial rotor parameters

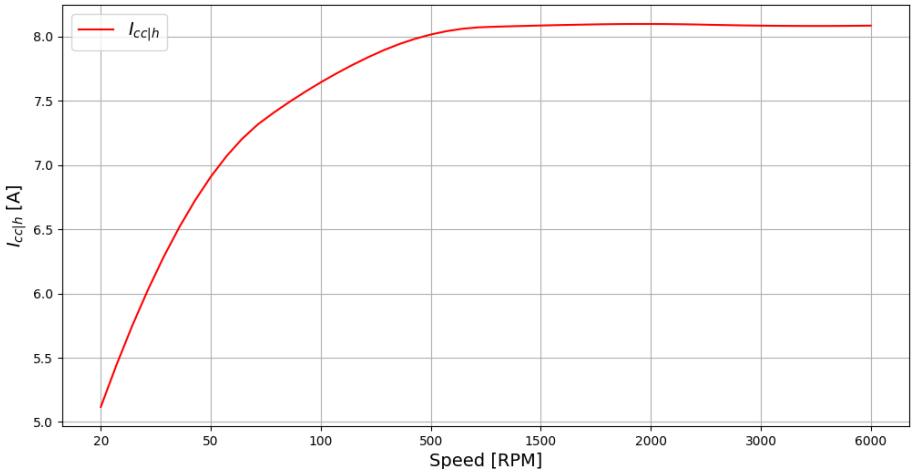

Figure 5.5: I_{cc} vs RPM

In Figure 5.6 the the circulating current present in the delta loop for the initial rotor design is displayed. Figure 5.7 displays the FFT of the circulating current extracted form the external circuit measurement in the delta loop.

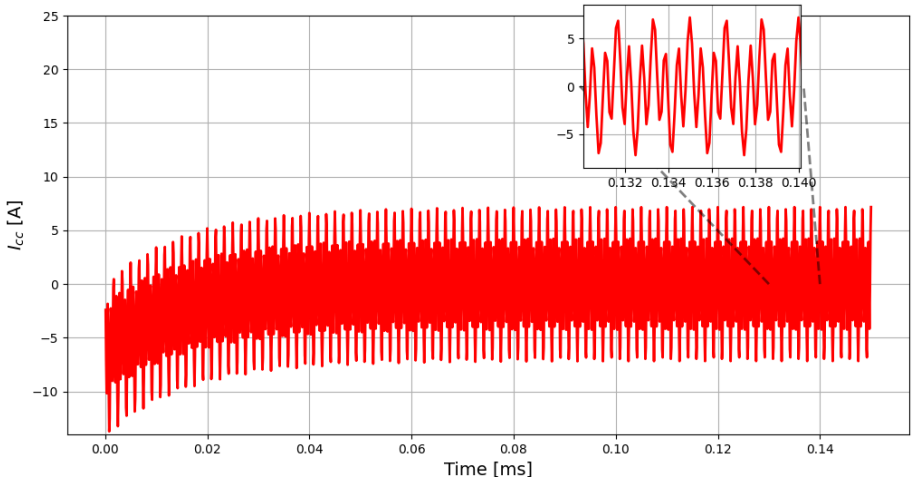

Figure 5.6: I_{cc} in no-load at 3000rpm

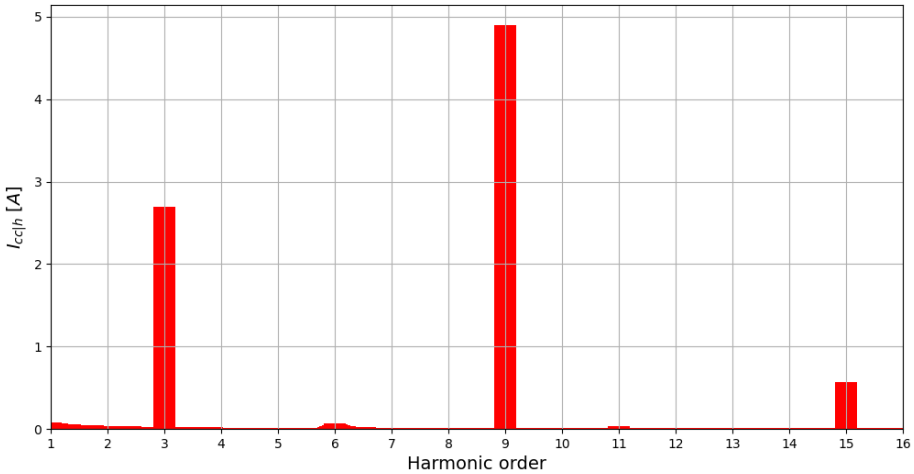

Figure 5.7: I_{cc} in no-load at 3000rpm

The resulting triplen harmonic content are presented in Table 5.2. Orders of triplen harmonics higher than 15 were not considered due to its much smaller amplitude.

Table 5.2: Circulating current harmonics amplitude in no load at 3000rpm

Harmonic order	Value	Unit
3^{rd}	2.675	A
9^{th}	4.914	A
15^{th}	0.5262	A

5.2.1 Inductance

In order to track the saturation in the model, a mapping of the DQ-inductance were done with reference to the DQ-current. A maximum DQ-current amplitude of 600 A was used as the boundary of the mapping, Figure 5.8.

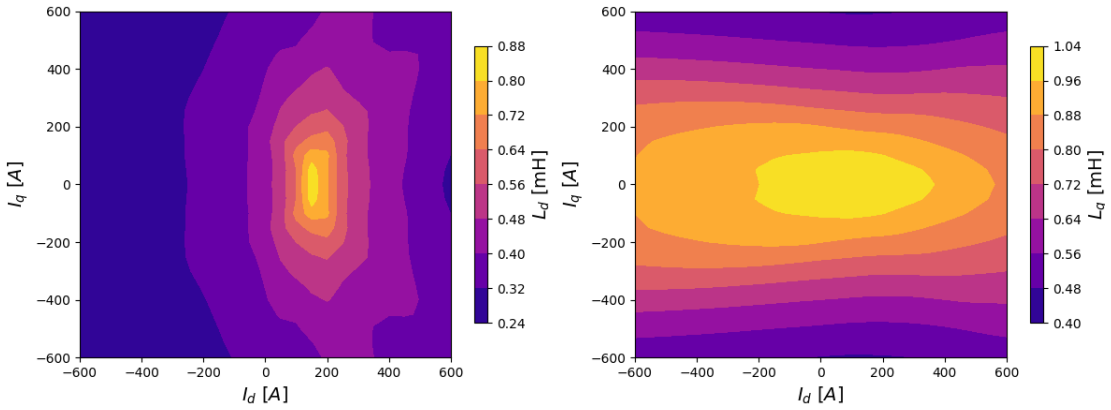

(a) Ld **(b)** Lq

Figure 5.8: Ld and Lq mapping

The inductances shows how the model reacts to applied currents with different magnitudes. Hence the mapping are useful for tracking the saturation behaviour of the model.

5.2.2 Flux linkage

In addition, similar mapping of the flux linkage Ψ in D- and Q-direction was computed to visualize the characteristics of the linked flux in the FE-model, Figure 5.9.

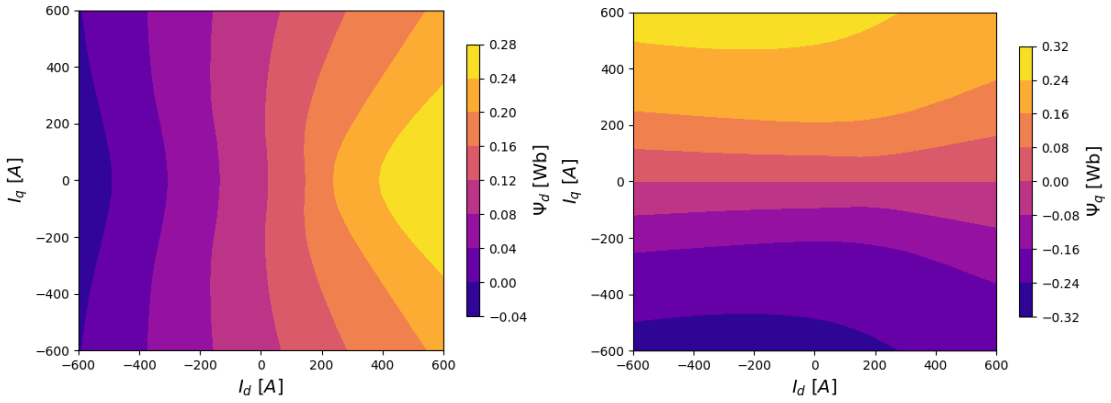

(a) Ψ_d **(b)** Ψ_q

Figure 5.9: Mapping of Ψ_d and Ψ_q

5.2.3 Saturation

It has earlier been stated that the saturation effect has the largest impact on the circulating current, specifically the third harmonic. In order to determine the impact of saturation in the model, several simulations were made with different levels of load current injected in the model through the external circuit. As mentioned, the input current was defined by ideal balanced three phase current sources generating ideal sinusoidal waves, however, referring to DQ-frame, three different magnitude ratios between I_d and I_q are introduced, $-30°$, $-45°$, and, $-60°$. Here, the Q-axis is the zero-reference. These magnitudes were selected to replicate typical MTPA operation for PMSM drive. Figure 3.3 in section 3.2.2.1, displays the chosen magnitude ratios in a DQ-coordinate system.

Noteworthy is that the DQ-ratios were kept static for speeds below base speed for simplicity reasons. Importantly, the optimal MTPA curvature is most likely not static for every speed below base speed but often increased slightly with increased speed.

In section 5.2.1, Figure 5.8, the saturation effect for the modelled machine is apparent for every possible current angle in the DQ-frame. The interesting saturation effect occurs for positive I_q currents and negative I_d currents, also noted as the second quadrant in the DQ-frame. For this reason, the load current was swept over three different DQ-magnitude ratios in order to visualize the relation between the saturation and the current harmonics generating the circulating current in the delta loop. The peak value of the load phase current in the delta phase winding can be described as the max value of I_d and I_q as,

$$I_{max} = \sqrt{I_d^2 + I_q^2} \tag{5.6}$$

Figure 5.10, displays the circulating current as a function of the line input current with different angles between I_d and I_q generating different saturation effects.

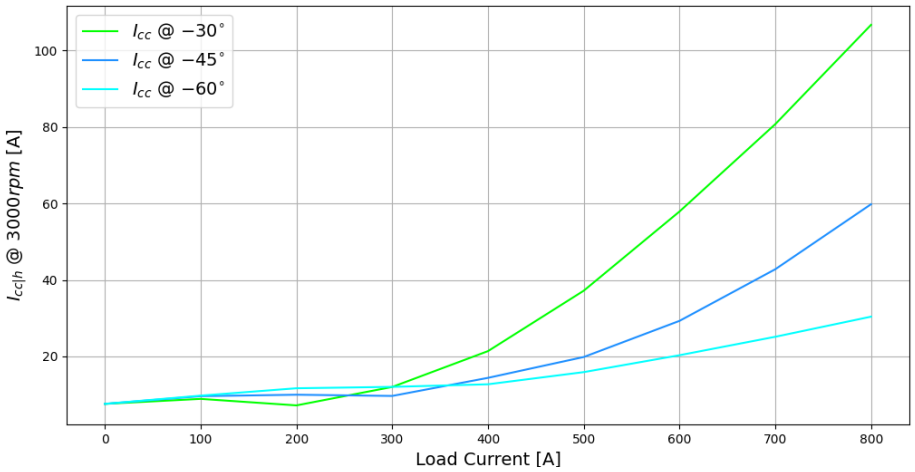

Figure 5.10: Saturation vs DQ-ratio

As the simulations allowed the extraction of the third and ninth harmonics, both

falling within the triplen harmonics category. These extracted harmonics reveal a notable contrast in how saturation impacts specific harmonics, as portrayed in Figure 5.11. It is important to note that higher-order harmonics were excluded from consideration due to having significantly lower current amplitudes.

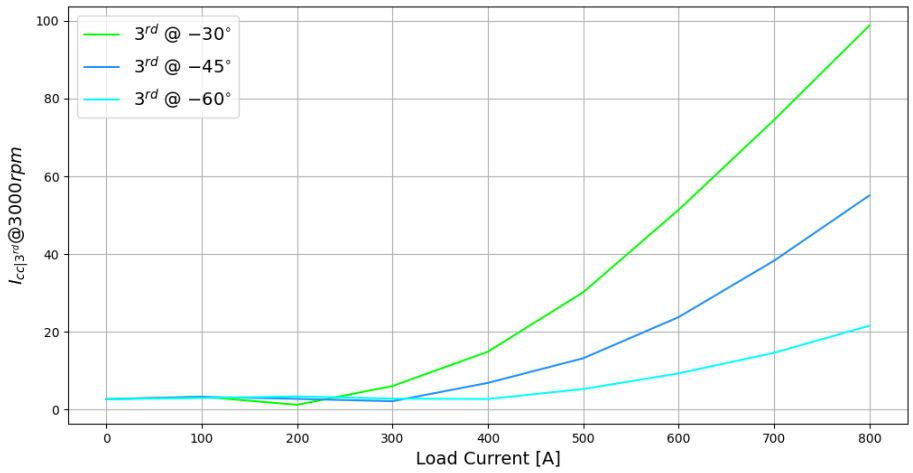

(a) $I_{cc|3^{rd}}$ at different load currents

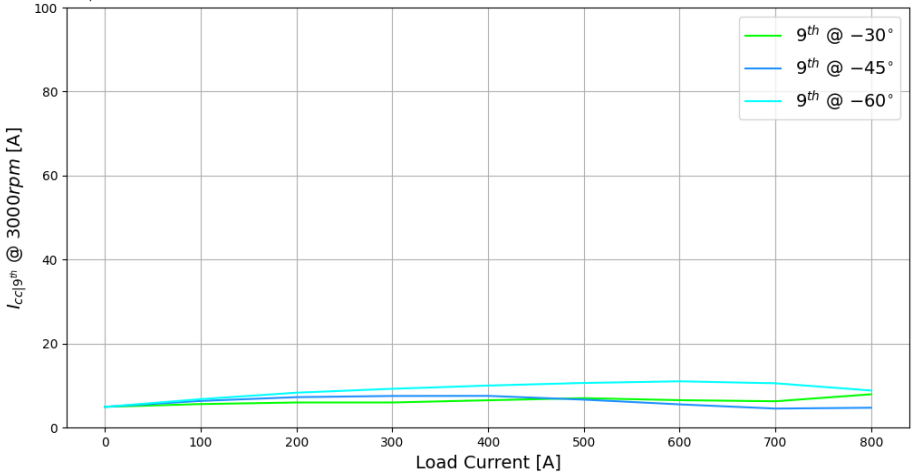

(b) $I_{cc|9^{th}}$ at different load currents

Figure 5.11: Harmonic amplitude at different load currents

The third harmonic experiences a notable surge with saturation. Nevertheless, in scenarios of low load current, below $250A$, the ninth harmonic surpasses it across all current magnitude ratios.

In addition, in Figure 5.12, the operational points are shown with respect to the inductance in L_d and L_q to highlight the specific difference in the inductive decay.

The variation in current magnitude ratios directly influences the values of L_d and L_q, thereby affecting saturation levels. Notably, the current magnitude ratio associated with the highest circulating current amplitude also experiences the quickest decrease in inductance value. Hence, signaling the most pronounced saturation.

Also, in Figure 5.13 the corresponding flux linkage can be seen to be reaching the highest value for the current ratio with the highest circulating current, as higher flux linkage indicates higher saturation impact.

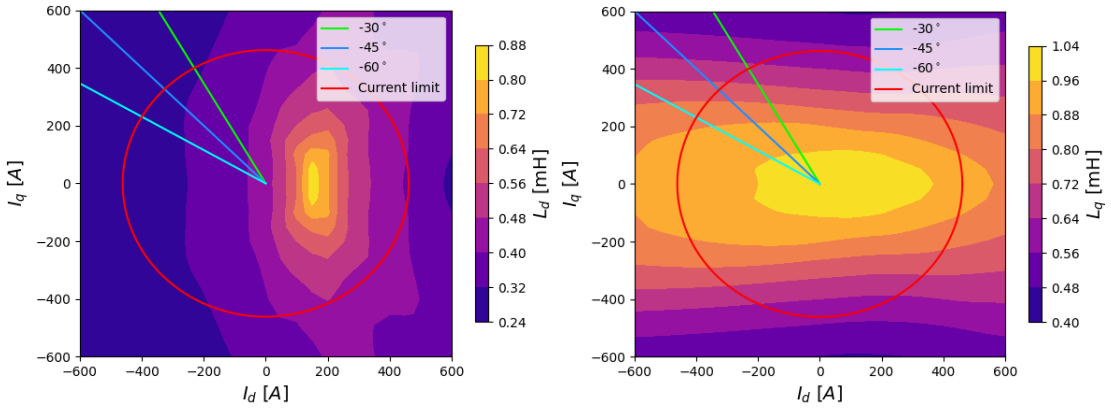

(a) L_d with current ratios **(b)** L_q with current ratios

Figure 5.12: L_d and L_q mapping with current ratios

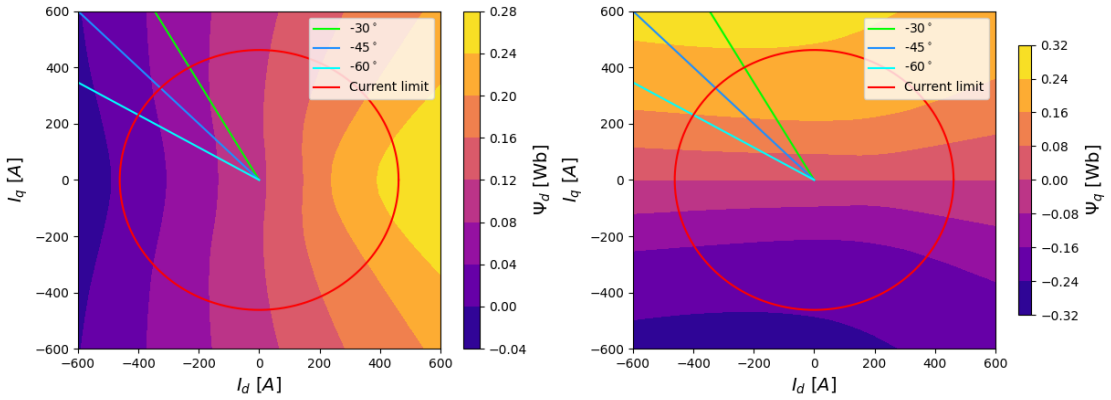

(a) Ψ_d with current ratios **(b)** Ψ_q with current ratios

Figure 5.13: Ψ_d and Ψ_q mapping with current ratios

In order to track the saturation impact more in detail, linear iron were introduced in both the stator and rotor separately. This was achieved by simply using a static relative permeability of $\mu_0 = 6000$ instead of a predefined B-H curve as seen in Figure 5.14.

First, linearity was introduced in the stator iron while the rotor material was kept as non-linear and simulated with line current ranging from 0 to 800 A peak, and a selected DQ-magnitude ratio of $-45°$. Then, for the same set of simulations, the stator teeth width was decreased. Lastly, the material in the linearity was introduced in the rotor material while the stator was kept non-linear, resulting in the circulating current, hence solely represented by the third harmonic, showed in Figure 5.15.

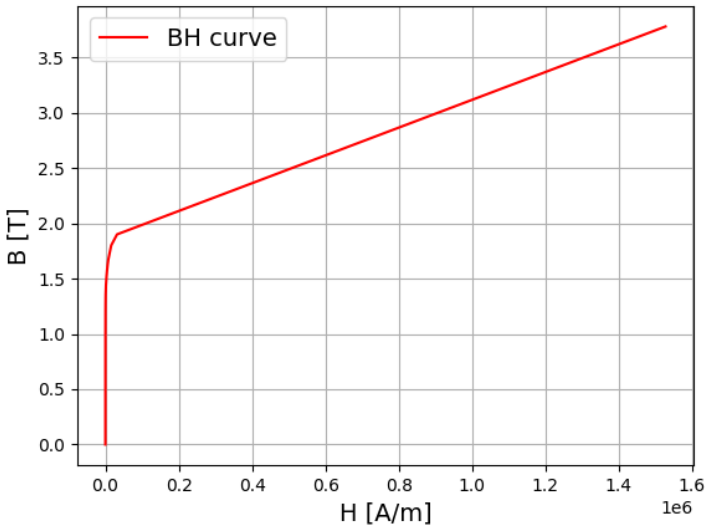

Figure 5.14: B-H curve for electric steel

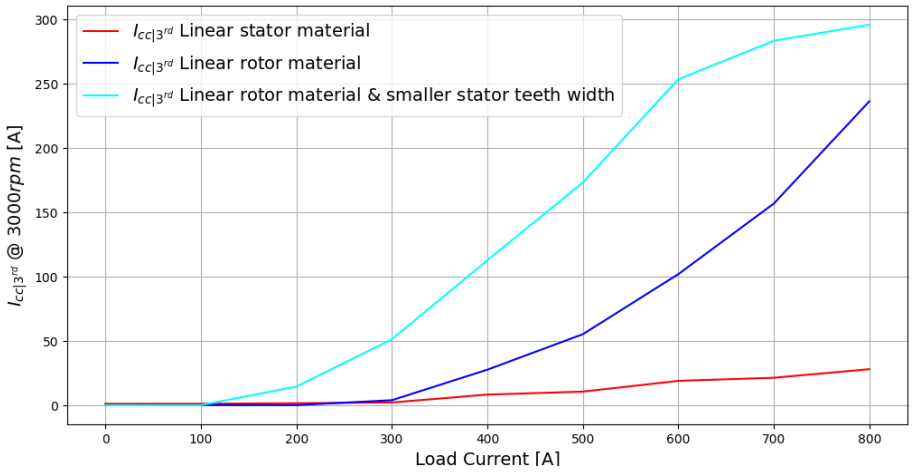

Figure 5.15: Linear material comparison on circulating current

Implementing linear relative permeability in the stator material exhibits a comparatively minor effect on reducing the circulating current, in contrast to the significant impact observed in models employing linear material in the rotor. Linearity precludes material saturation, causing the flux to increase linearly. As seen in the model with linear rotor material, the flux from the rotor generates high magnitudes and thereby saturating the stator. The result was substantial circulating current amplitudes. Moreover, in the model with linear rotor material and smaller stator teeth width, the stator saturates notably quicker due to the increased reluctance in the stator teeth leading to a higher flux and subsequently even greater circulating current amplitudes.

The difference in saturation is clearly visualized in Figure 5.16a and Figure 5.16b, where both were loaded with 300 A line current while having different stator teeth

width. The stator with smaller teeth has a significantly higher magnetic flux density present within the stator teeth.

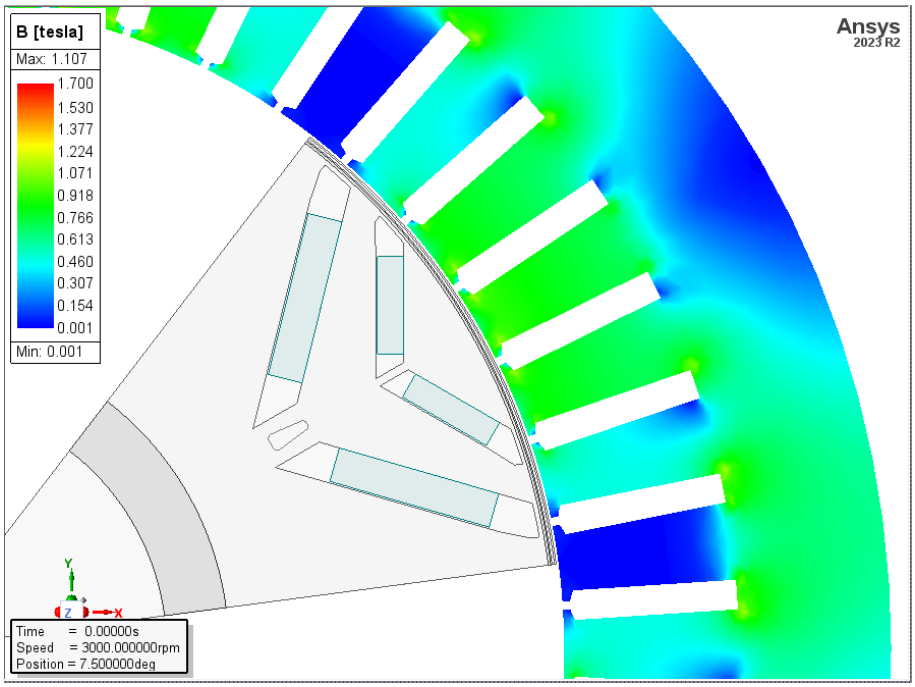

(a) Initial stator teeth width

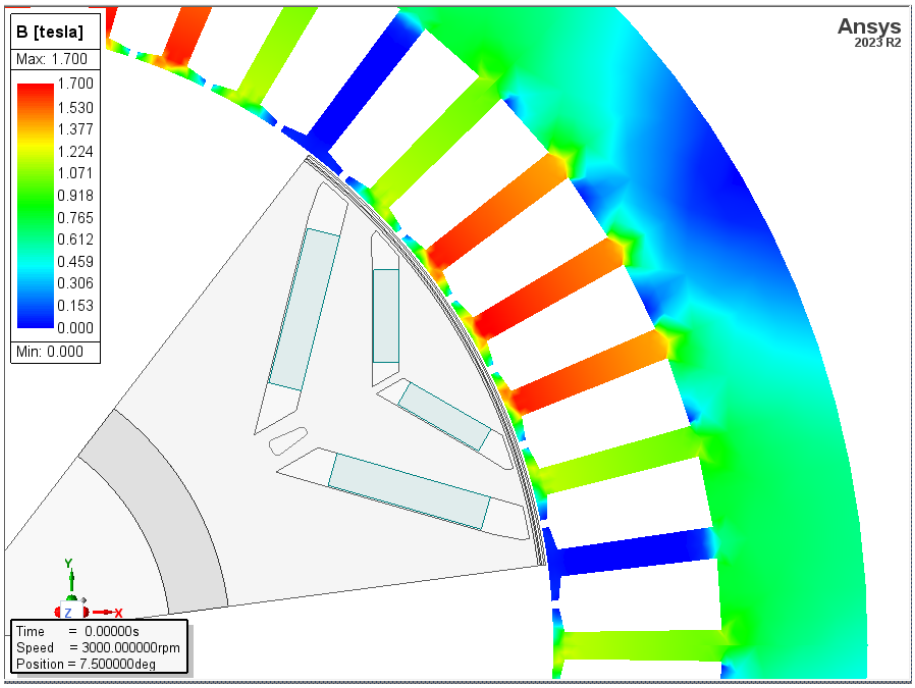

(b) Smaller stator teeth width

Figure 5.16: Stator teeth saturation

5.2.4 Copper losses

The circulating currents generate unwanted copper losses in the machine. In order to calculate the copper losses from the circulating currents, their harmonic amplitudes and the winding resistance were used. The active winding resistance R_{aw} was calculated by dividing the per winding solid loss P_{solid} by the square of the phase current I_{phase},

$$R_{aw} = \frac{P_{solid}}{I_{phase}^2} = 12.27m\Omega \tag{5.7}$$

The total resistance R per phase then becomes the sum of the active winding resistance and the end winding resistance R_{ew} calculated in (5.4)

$$R = R_{aw} + R_{ew} = 12.27 + 3.10 = 15.37m\Omega \tag{5.8}$$

The copper losses due to the circulating currents I_{cc} can then be calculated as

$$P_{cc} = R \times I_{cc}^2 \tag{5.9}$$

The resulting copper losses generated by the circulating currents are displayed in Figure 5.17, for a phase delay of $-45°$ degrees.

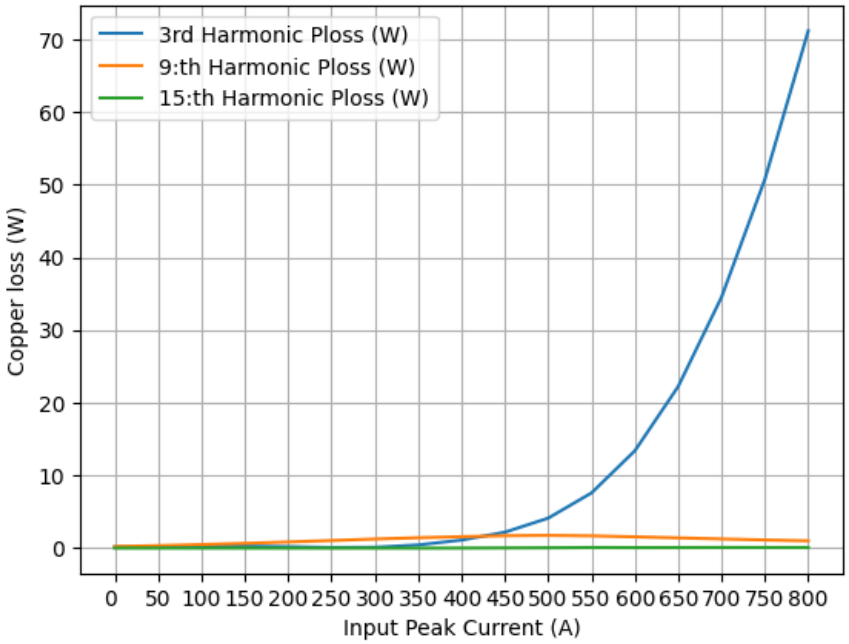

Figure 5.17: Circulating current copper losses

Moreover, in Figure 5.18 the copper losses generated by the model with reduced stator teeth width are presented. As expected from Figure 5.15, the increased circulating current increase the copper losses drastically.

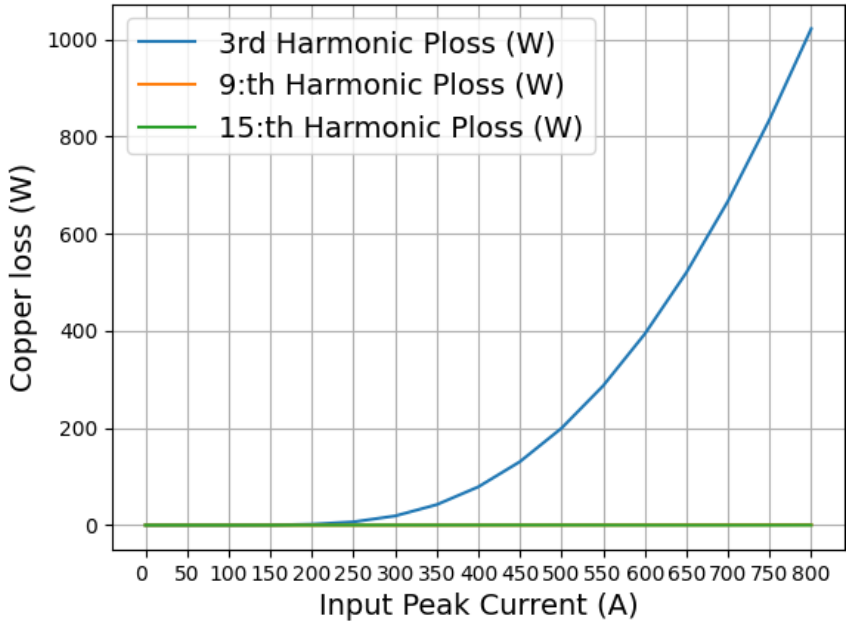

Figure 5.18: Circulating current copper losses - Smaller teeth width

5.3 Parametric evaluation

The parameters was initially swept individually to determine the impact from each of them. The boundaries for each sweep was determined by the geometrical and mechanical constraints. In other words, the parameters were swept from largest possible value to smallest possible values with respect to the geometry of the rotor, and within reasonable mechanical limits.

5.3.1 Circulating current

The individual impact on the circulating current in no load condition is presented in Figure 5.19a-5.19d for the angle parameters, and in Figure 5.20a-5.20d for the length and thickness parameters. It should be noted that the parameters were set to their initial values, seen in Table 5.1 while not being swept.

From the individual parameter evaluation, it was shown that the extension length for the second magnet layer had a large impact on the circulating current amplitude together with the arc angles for both magnet layers.

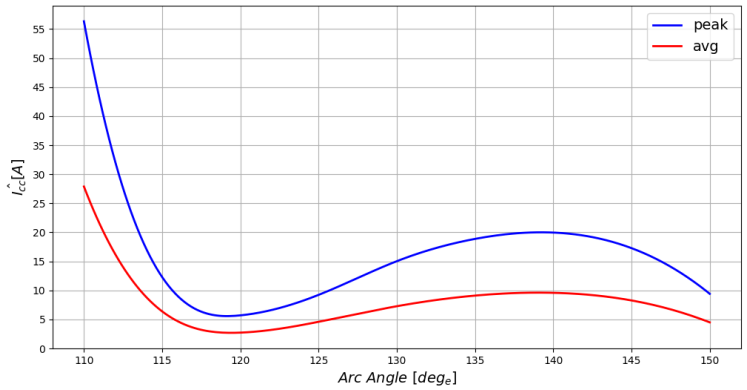

(a) L1 Arc Angle

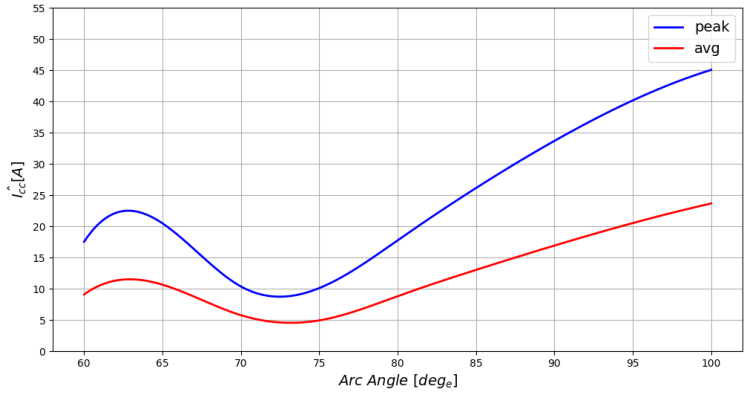

(b) L2 Arc Angle

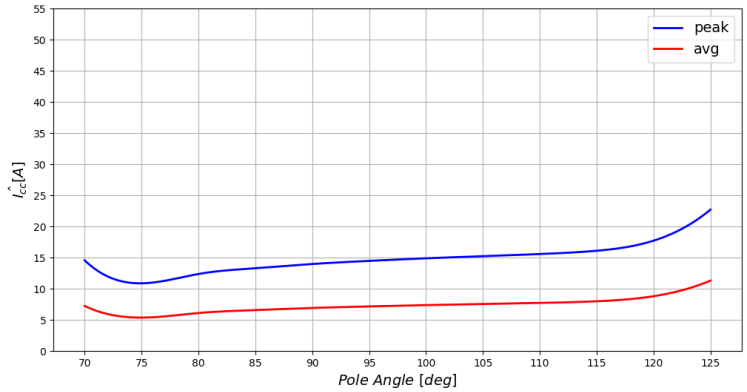

(c) L1 Pole Angle

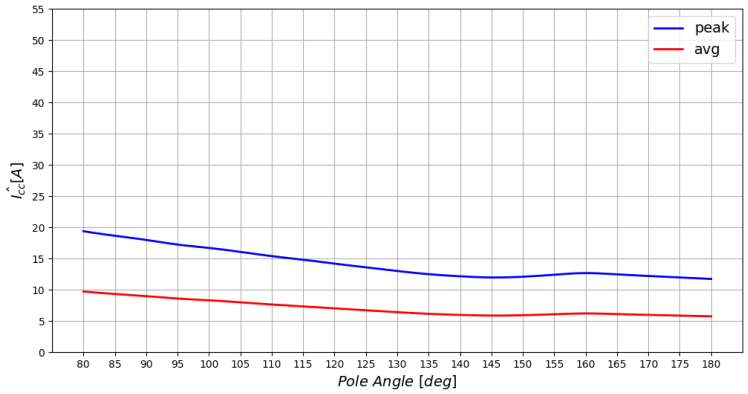

(d) L2 Pole Angle

Figure 5.19: Individual angle parameter impact on circulating current

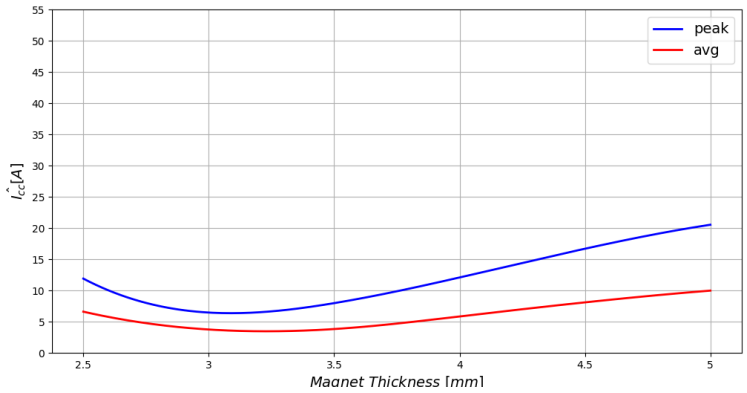

(a) L1 Magnet Thickness

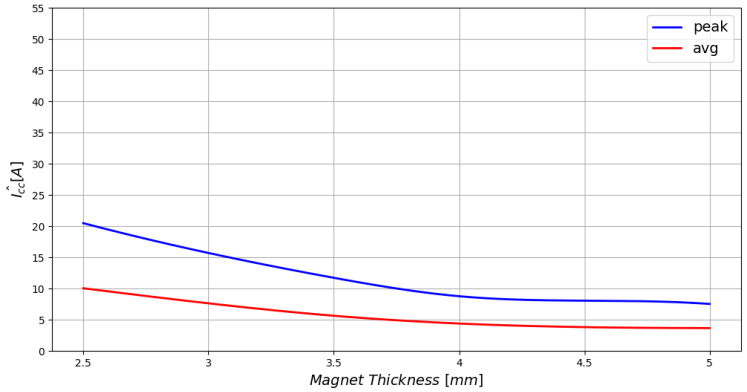

(b) L2 Magnet Thickness

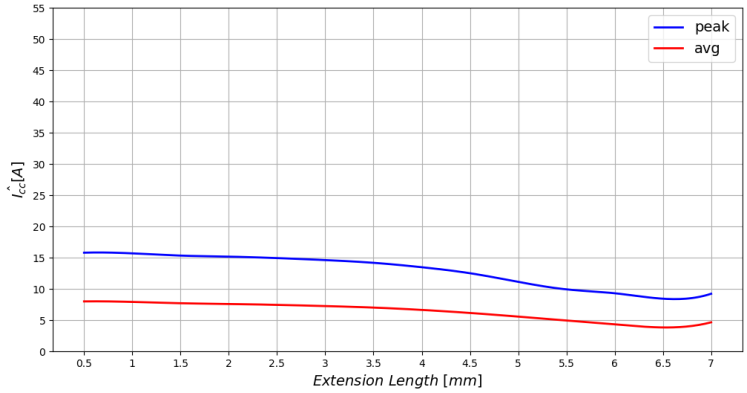

(c) L1 Extension Length

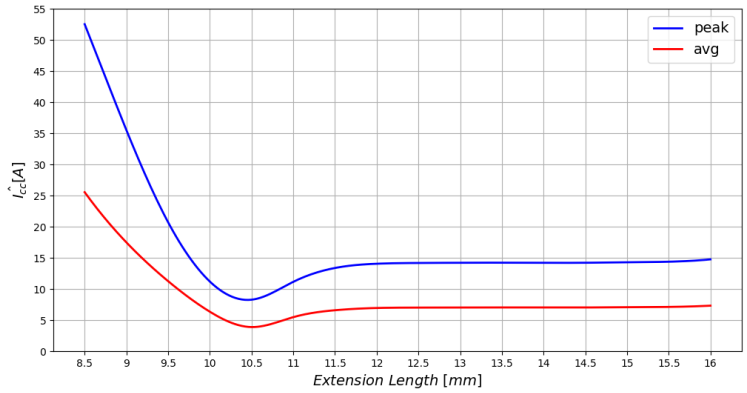

(d) L2 Extension Length

Figure 5.20: Individual length and thickness parameter impact on circulating current

Thereafter, each parameter pair was swept utilizing the same principle resulting in the co-dependence of each parameter pair. Figure 5.21a-5.21b show the angle parameters whereas 5.22a-5.22b show the length and thickness parameters.

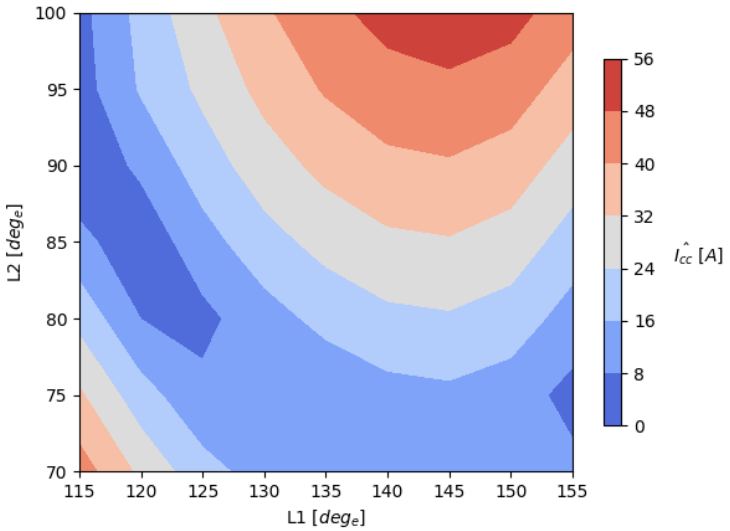

(a) Arc angle vs I_{cc}

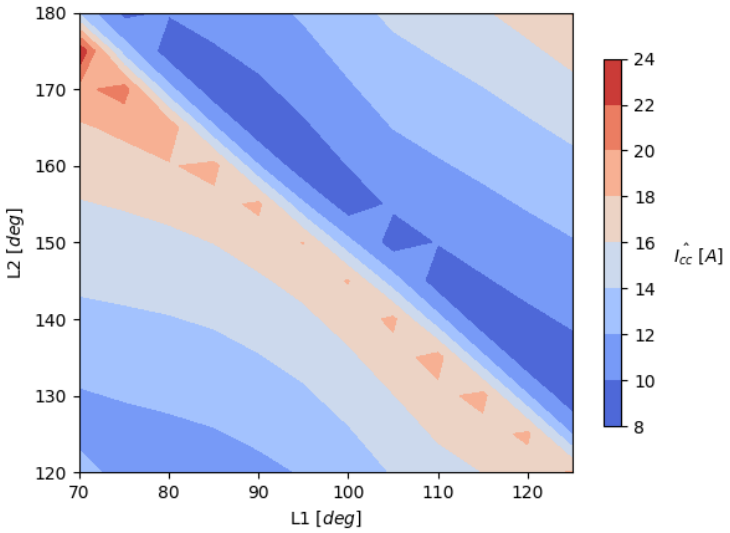

(b) Pole angle vs I_{cc}

Figure 5.21: Combined angle parameters impact on circulating current

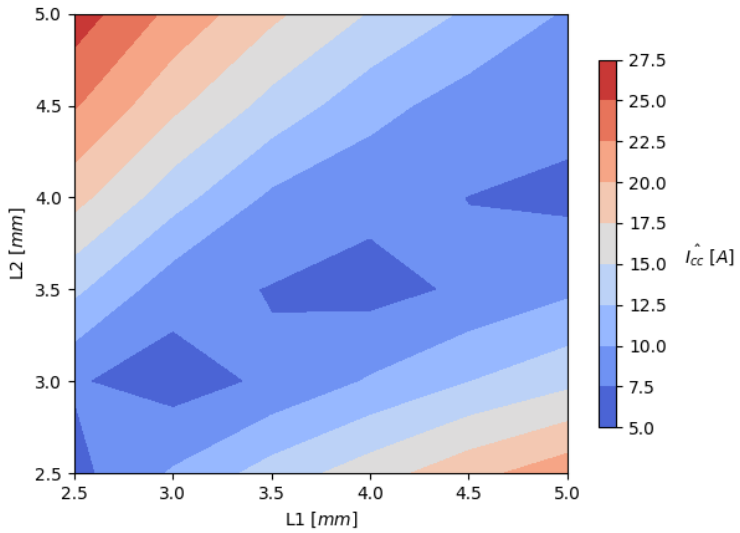

(a) Magnet thickness vs I_{cc}

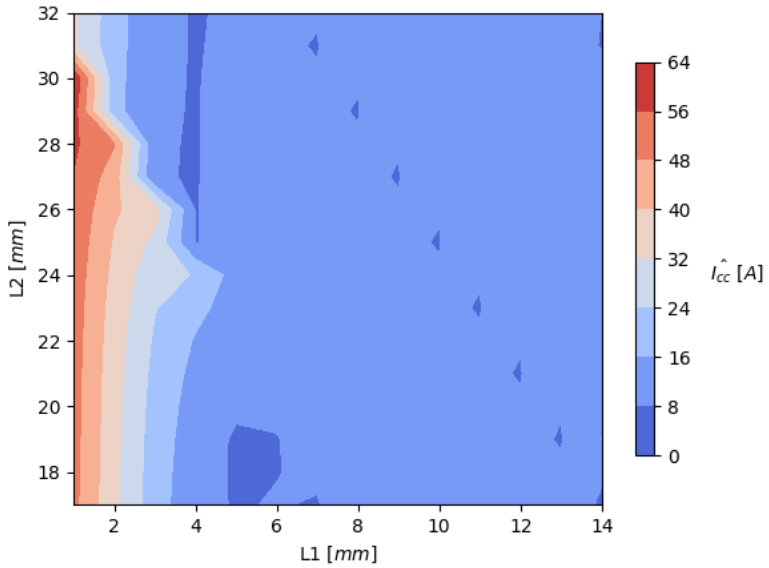

(b) Extension length vs I_{cc}

Figure 5.22: Combined length and thickness parameters impact on circulating current

As can be seen the pole angle had a smaller impact on the circulating current in both the individual evaluation and the pair-parametric evaluation. However, its impact is believed to be mirroring the concentration of the magnetic flux in the air-gap. When the magnetic flux is heavily concentrated in one reluctance path, local saturation will occur. Consequently, the triplen harmonic will be enhanced. Similarly, the magnet thickness reflects on the circulating current magnitude as a ratio between the first and second magnet layer. For the model, the ratio could be seen in the pair-parametric evaluation where it was constant over the each simulated steps.

5.3.2 Air-gap flux density

To further analyze the rotor parametric impact on B_{airgap}, the slots in the stator as well as the coils were removed. The slotless design can be seen in Figure 5.23.

Simulations were made in no load condition at 3000rpm and swept over several values for each changeable parameter, resulting in an explicit display of the magnitude of B_{airgap} for each parameter. Figures 5.24a-5.24d show the characteristics of each changeable angle parameter and Figures 5.25a-5.25d show each changeable length and thickness parameter. All sub-Figures in 5.24 and 5.25 is displayed as a function of the distance representing two pole pitches - marked as the dashed lines in Figure 5.23 where the slotless stator model is shown.

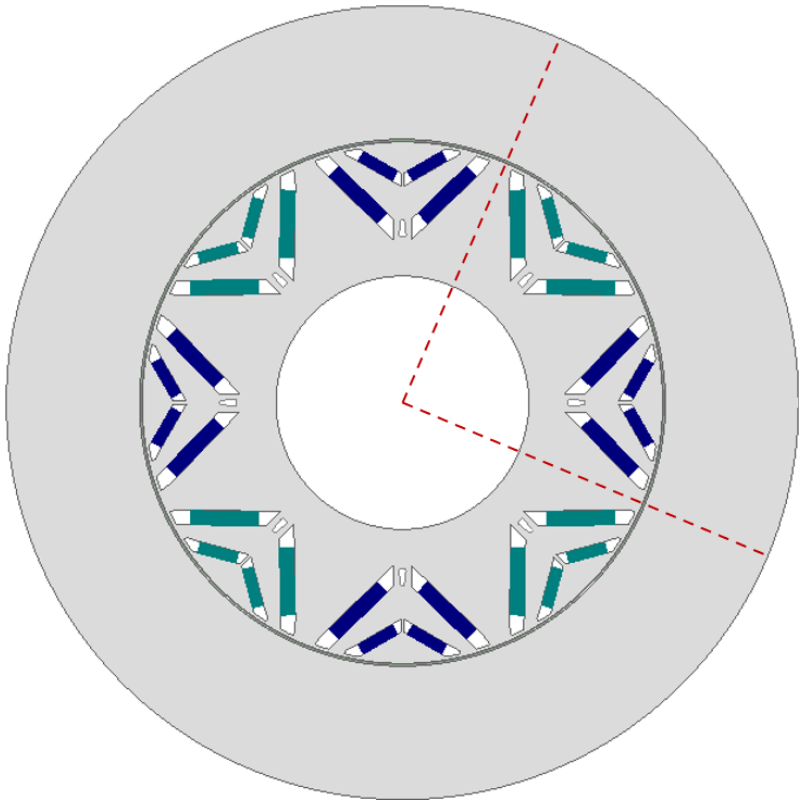

Figure 5.23: Slotless stator model

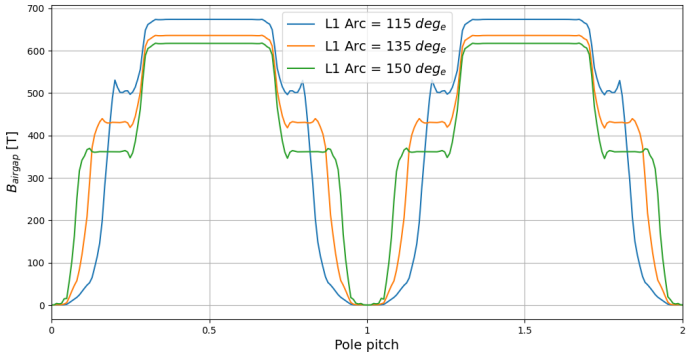

(a) L1 Arc Angle

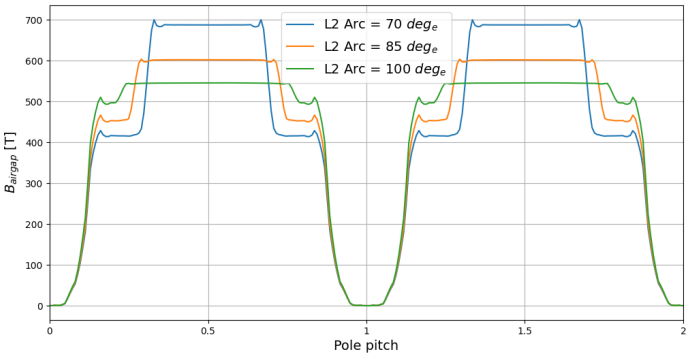

(b) L2 Arc Angle

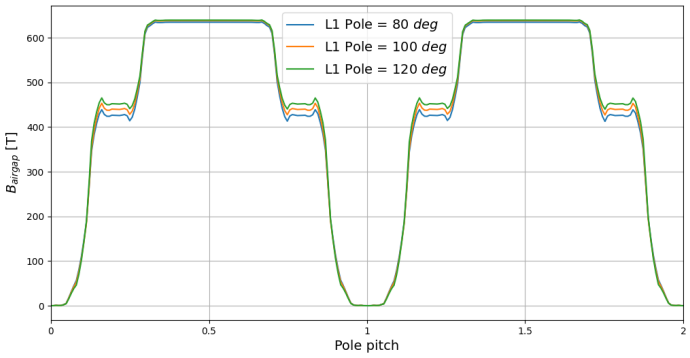

(c) L1 Pole Angle

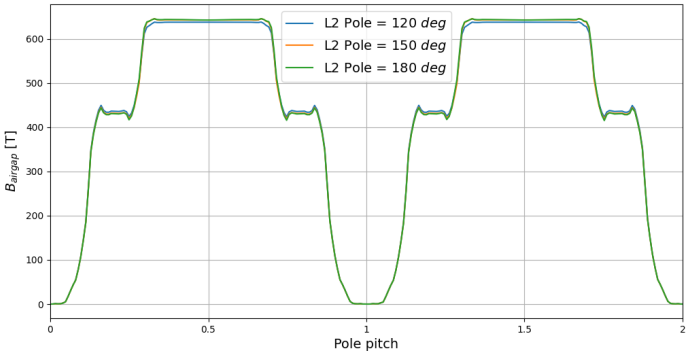

(d) L2 Pole Angle

Figure 5.24: Individual angle parameter impact on ideal air-gap flux density waveform

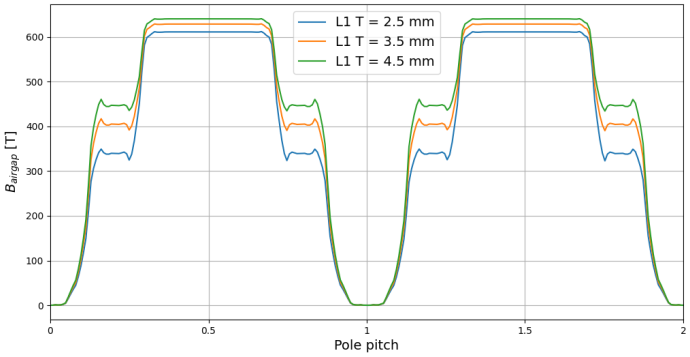

(a) L1 Magnet Thickness

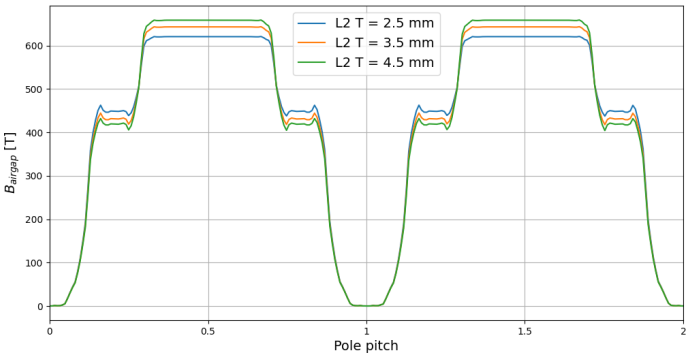

(b) L2 Magnet Thickness

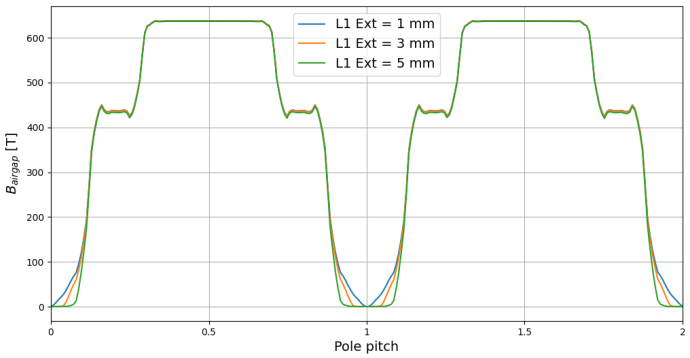

(c) L1 Extension Length

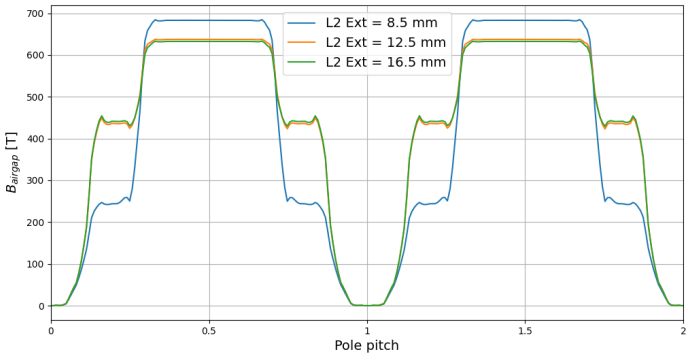

(d) L2 Extension Length

Figure 5.25: Individual length and thickness parameter impact on ideal air-gap flux density waveform

In accordance with the evaluation of circulating currents based on individual impacts, as presented in the previous section, similarities are expected in the air-gap flux density. The most significant deviations in circulating current, as depicted in 5.19a-5.20d, were notably associated with pole arc angles for both layers and the extension length of the flux barrier in the second magnet layer. Similarly, the largest deviations in air-gap flux density were observed in the same parameters, as shown in 5.24a-5.25d. This correlation arises from the fact that the arc angles, along with the extension lengths, resemble the pole coverage which hold a decisive influence on the produced triplen harmonic. This by impacting the sinusoidal degree and zero-crossing directly in the linked flux.

5.4 Taguchi analysis

The levels used in the first iteration of the Taguchi experimental design was determined from the co-dependent variables from the pair-parametric evaluation in section 5.3. The areas of the lowest circulating currents was set as the levels and can be seen in Table 5.3.

Table 5.3: Table of parameter levels

Parameter	Level 1	Level 2	Level 3	Level 4	Unit
$L1_{Ext}$	2.3	2.9	-	-	mm
$L2_{Ext}$	11.6	12	12.4	12.8	mm
$L1_{Arc}$	116	119	122	125	degrees
$L2_{Arc}$	78	81	84	87	degrees
$L1_{Pole}$	110	114	119	123	degrees
$L2_{Pole}$	135	139	143	147	degrees
$L1_{T}$	3.1	3.5	3.9	4.3	mm
$L2_{T}$	3	3.2	3.4	3.6	mm

The resulting orthogonal array as well as the third harmonic current amplitude for each simulation in no load can be seen in Table 5.4.

Table 5.4: $L_{32}(4^8)$ Orthogonal array

Simulation	$L1_{Ext}$	$L2_{Ext}$	$L1_{Arc}$	$L2_{Arc}$	$L1_{Pole}$	$L2_{Pole}$	$L1_T$	$L2_T$	$I_{cc\|3^{rd}}$
1	1	1	1	1	1	1	1	1	26.81
2	1	2	2	2	2	2	2	2	14.34
3	1	3	3	3	3	3	3	3	0.42
4	1	4	4	4	4	4	4	4	12.31
5	1	1	1	2	2	3	3	4	20.67
6	1	2	2	1	1	4	4	3	7.5
7	1	3	3	4	4	1	1	2	1.69
8	1	4	4	3	3	2	2	1	6.78
9	1	1	2	3	4	1	2	3	11.76
10	1	2	1	4	3	2	1	4	11.35
11	1	3	4	1	2	3	4	1	6.12
12	1	4	3	2	1	4	3	2	5.6
13	1	1	2	4	3	3	4	2	1.97
14	1	2	1	3	4	4	3	1	7.7
15	1	3	4	2	1	1	2	4	3.76
16	1	4	3	1	2	2	1	3	1.47
17	2	1	4	1	4	2	3	2	9.76
18	2	2	3	2	3	1	4	1	7.53
19	2	3	2	3	2	4	1	4	5.05
20	2	4	1	4	1	3	2	3	3.64
21	2	1	4	2	3	4	1	3	5.08
22	2	2	3	1	4	3	2	4	4.91
23	2	3	2	4	1	2	3	1	1.14
24	2	4	1	3	2	1	4	2	8.15
25	2	1	3	3	1	2	4	4	0.64
26	2	2	4	4	2	1	3	3	5.43
27	2	3	1	1	3	4	2	2	3.6
28	2	4	2	2	4	3	1	1	0.4
29	2	1	3	4	2	4	2	1	1.02
30	2	2	4	3	1	3	1	2	5.36
31	2	3	1	2	4	2	4	3	8.09
32	4	4	2	1	3	1	3	4	5.73

In addition, the signal-to-noise ratios from the first iteration of the Taguchi design experiment can be seen in Figure 5.26.

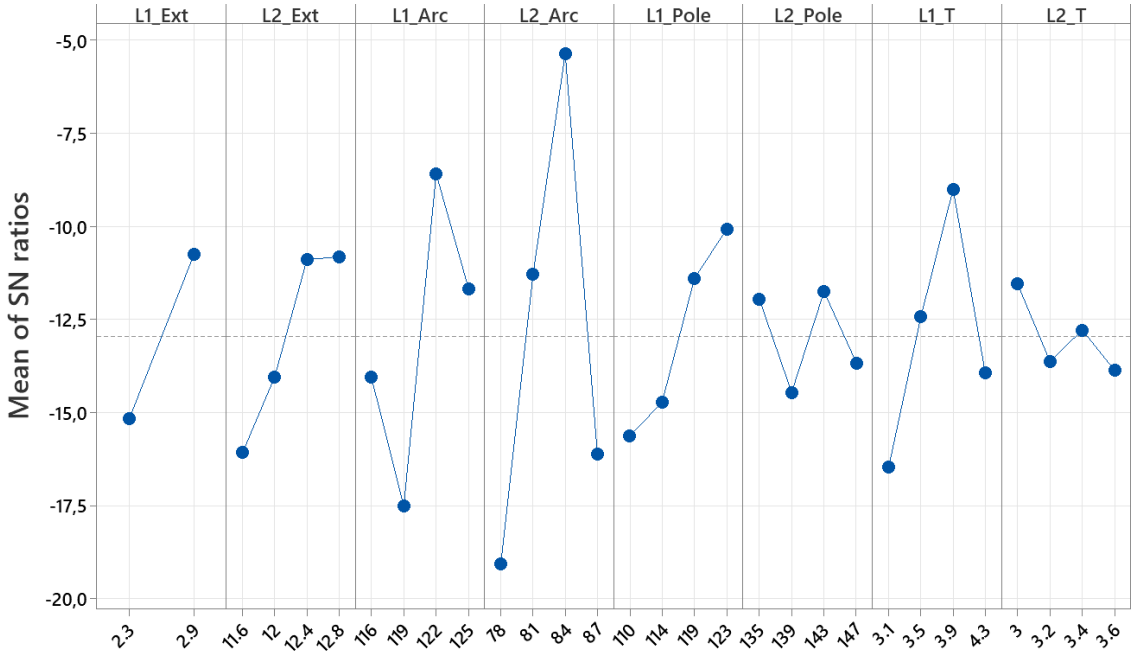

Figure 5.26: SN-Ratios: first iteration

From Figure 5.26 the optimal levels for each parameter can be seen in Table 5.5, representing the highest SN ratio.

Simulating the model incorporated with the values in Table 5.5, the FFT of the current signal can be seen in Figure 5.27 and the triplen current harmonic amplitudes can be seen in Table 5.6.

Table 5.5: Optimal parameters
- First iteration

Parameter	Value	Unit
$L1_{Ext}$	2.9	mm
$L2_{Ext}$	12.8	mm
$L1_{Arc}$	122	deg
$L2_{Arc}$	84	deg
$L1_{Pole}$	123	deg
$L2_{Pole}$	143	deg
$L1_{T}$	3.9	mm
$L2_{T}$	3	mm

Table 5.6: Circulating current amplitudes
- First iteration

Harmonic order	Value	Unit
3^{rd}	2.312	A
9^{th}	2.466	A
15^{th}	0.591	A

Comparing with the values from the initial model presented in Table 5.1, and the triplen harmonic amplitudes in Table 5.2. A decrease of 13.57% for the third harmonic, as well as 49.82% for the ninth harmonic has been made with the optimized parameters. Although, an increase of 12.35% for the fifteen harmonic was observed.

Figure 5.27: FFT - first iteration

To further optimize the response variable and improve accuracy with a reduced parametric range, a second iteration of the Taguchi experimental design was done. The parametric boundaries for the second iteration can be seen in Table 5.7.

Table 5.7: Table of parameter levels - second iteration

Parameter	Level 1	Level 2	Level 3	Level 4	Unit
$L1_{Ext}$	2.9	3.1	-	-	mm
$L2_{Ext}$	12.4	12.6	12.8	13	mm
$L1_{Arc}$	122	124	126	128	deg
$L2_{Arc}$	79	81	83	85	deg
$L1_{Pole}$	114	117	120	123	deg
$L2_{Pole}$	140	142	144	146	deg
$L1_{T}$	3.6	3.8	4	4.2	mm
$L2_{T}$	2.9	3.1	3.3	3.5	mm

The signal-to-noise ratios from the second iteration of the Taguchi experimental design can be seen in Figure 5.28.

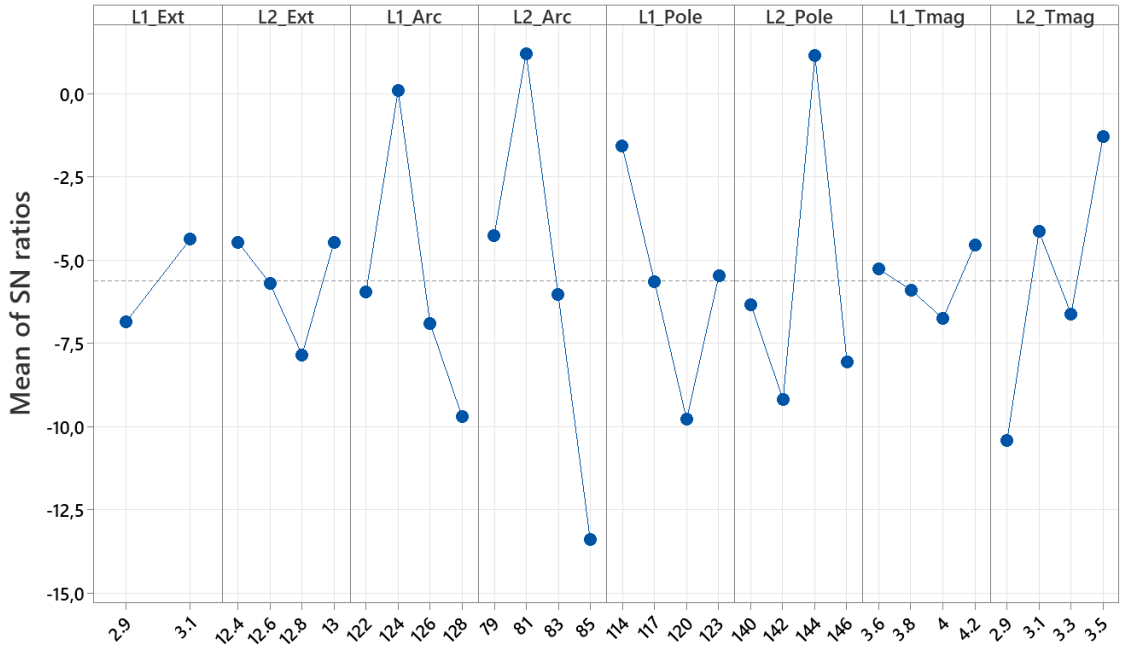

Figure 5.28: SN-ratios second iteration

As the first iteration, reading the parametric values of the highest SN ratio in Figure 5.28 the optimal value for each parameter can be determined. The values are presented Table 5.8 and the corresponding harmonic amplitudes are shown in Table 5.9.

Table 5.8: Optimal parameters - Second iteration

Parameter	Value	Unit
$L1_{Ext}$	3.1	mm
$L2_{Ext}$	12.4	mm
$L1_{Arc}$	124	deg
$L2_{Arc}$	81	deg
$L1_{Pole}$	114	deg
$L2_{Pole}$	144	deg
$L1_{T}$	4.2	mm
$L2_{T}$	3.5	mm

Table 5.9: Circulating current amplitudes - Second iteration

Harmonic order	Value	Unit
3^{rd}	0.271	A
9^{th}	3.138	A
15^{th}	0.745	A

The FFT of the current signal with the optimal values from the second iteration can be seen in Figure 5.29.

Figure 5.29: FFT second iteration

In Section 2.4.2, it was stated that the Taguchi method prioritizes robustness which does not necessarily translate to the minimum circulating current amplitude at a particular point. The lowest third harmonic current amplitude was identified in the second iteration of the Taguchi method. With a different set of parameters than for the parameters resulting in the best robustness, these parametric values can be seen in Table 5.10 and the harmonic amplitudes are shown in Table 5.11.

Table 5.10: Optimal parameters - lowest third harmonic amplitude

Parameter	Value	Unit
$L1_{Ext}$	3.1	mm
$L2_{Ext}$	12.4	mm
$L1_{Arc}$	124	deg
$L2_{Arc}$	83	deg
$L1_{Pole}$	117	deg
$L2_{Pole}$	144	deg
$L1_{T}$	3.6	mm
$L2_{T}$	3.5	mm

Table 5.11: Circulating current amplitudes - Lowest third harmonic

Harmonic order	Value	Unit
3^{rd}	0.123	A
9^{th}	2.819	A
15^{th}	0.758	A

The resulting design with the minimum circulating current design rotor parameters from the second Taguchi iteration can be seen in Figure 5.30.

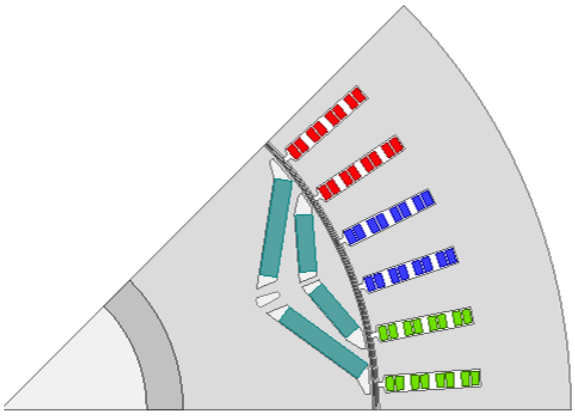

Figure 5.30: Minimum circulating current design

Figure 5.31 displays the FFT of the lowest resulting third harmonic current.

Figure 5.31: FFT second iteration

The reduction of the third harmonic current amplitude from the initial model was 89.9% for the second iteration of the Taguchi method in no load. With the lowest third harmonic current measured in a single simulation, the reduction was 95.5%. At 800 A line current, comparing the third harmonic amplitude of the initial and optimized model, the decrease was calculated to 5.77%. Figure 5.32 shows the amplitudes of the harmonic content in the first and second Taguchi optimization together with the iteration that generated the lowest circulating current.

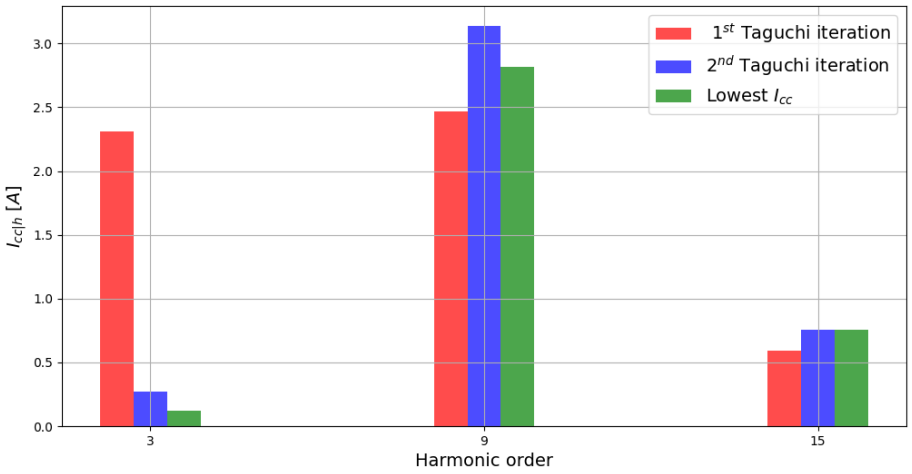

Figure 5.32: Taguchi iteration comparison

The copper losses as a function of increasing load current from 0 A to 800 A with 50 A steps is shown in Figure 5.33. The sum of the losses for the optimal model was calculated to 10% lower than from the initial model.

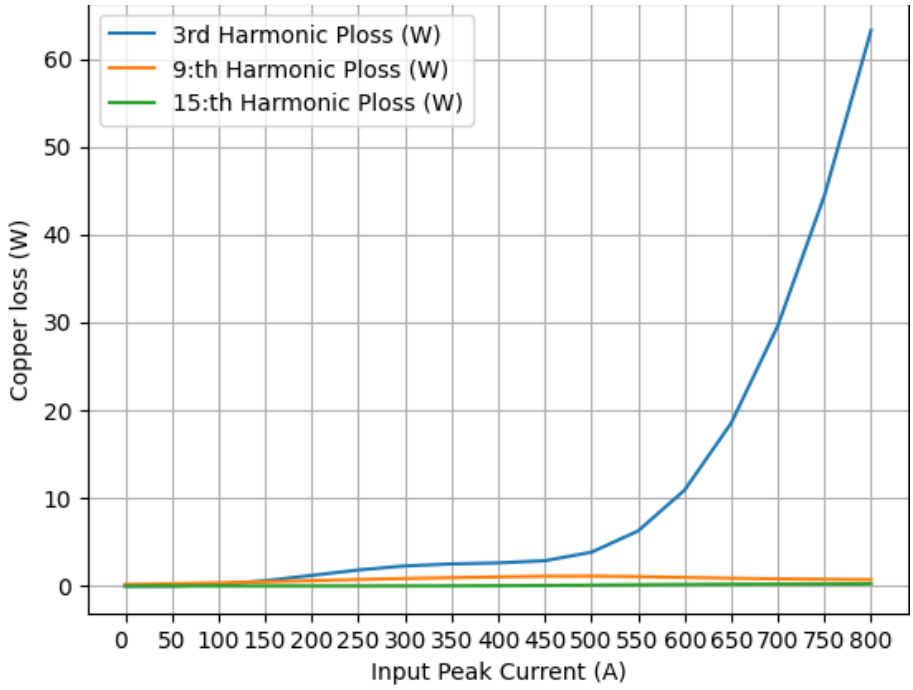

Figure 5.33: Circulating current copper losses - optimal model

Comparing the initial model with the optimized model with reduced stator teeth width. The sum of the power losses was compared between the two models from 0-350 A and from 400-800 A. The line plot for both models can be seen in Figure 5.34 and the power losses and its comparison can be seen in Table 5.12.

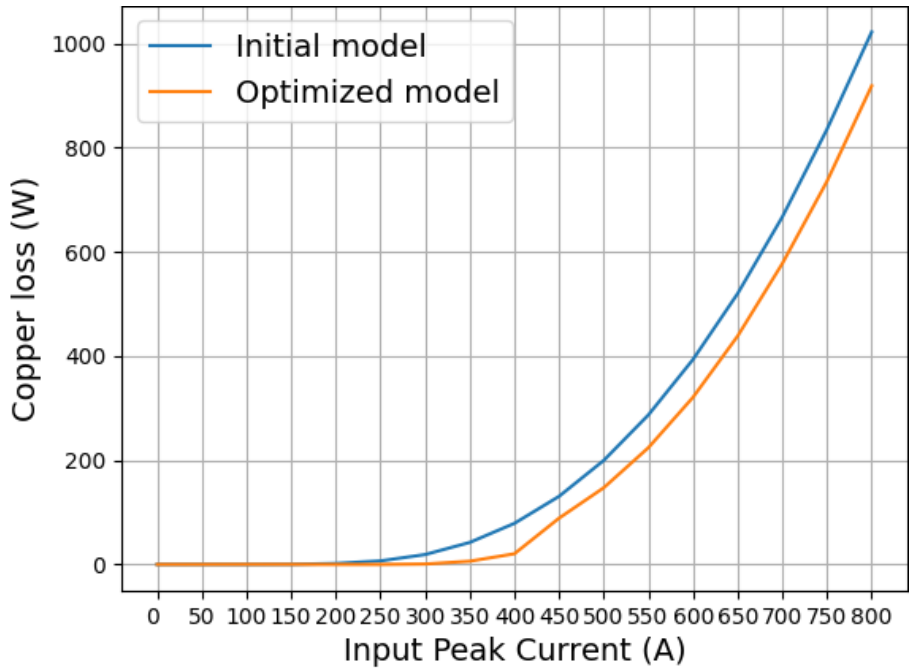

Figure 5.34: Circulating current copper losses - initial vs optimized model

Table 5.12: Power losses comparison - initial vs optimized model

Load current	Initial model	Optimized model	Reduction
0-350 A	70.36 W	7.40 W	89.5 %
400-800 A	4053.33 W	3450.25 W	14.9 %

With reduced stator teeth width, the optimized model reduced the copper losses by 89.5% between 0-350 A compared to the initial model. From 400-800 A, the reduction of the copper losses was calculated to be 14.9% lower than the initial model.

Both the standard model and the reduced stator teeth width model follow the same trend. In low load currents, the investigated parameters have a significant impact on reducing the circulating currents and the power losses. While at higher load currents, the parameters lose much of their significance in reducing the triplen harmonics. The triplen harmonic amplitudes were heavily impacted by the level of saturation in the machine stator and rotor core. Undoubtedly, the saturation effect has a considerably larger impact on the circulating current than the rotor parameters in high input currents since the optimal rotor configuration can not effectively reduce the saturation, resulting in only 5.7% reduction in maximum load compared to 95.5% in no load. As mentioned, the level of saturation can be impacted by the

choice of material or larger size of the machine. However, this comes with increased manufacturing costs.

5.4.1 ANOVA

The ANOVA result from the first iteration seen in Table 5.13 show that the variables $L1_{Ext}$ and $L2_{Arc}$ have a significant impact on the circulating current amplitude. While $L2_{Arc}$ is almost at the threshold to be seen as significant. Having an interaction between these two parameters seen in Table 5.14 show parameters $L1_{Arc}$ and $L2_{Arc}$ now have a significant impact. Parameter $L1_{Ext}$ is now close to the threshold to be seen as significant.

Table 5.13: F-value and P-value - first iteration

Parameter	F-value	P-value
$L1_{Ext}$	6.9975	0.0267
$L2_{Ext}$	2.4836	0.1271
$L1_{Arc}$	3.0024	0.0876
$L2_{Arc}$	5.0791	0.0250
$L1_{Pole}$	1.2905	0.3359
$L2_{Pole}$	0.4647	0.7139
$L1_{T}$	0.9644	0.4507
$L2_{T}$	0.0822	0.9680

Table 5.14: F-value and P-value - first iteration with interaction effect

Parameter	F-value	P-value
$L1_{Ext}$	4.6419	0.0633
$L2_{Ext}$	2.5850	0.1258
$L1_{Arc}$	5.2799	0.0267
$L2_{Arc}$	4.6238	0.0370
$L1_{Pole}$	1.3432	0.3272
$L2_{Pole}$	0.4837	0.7028
$L1_{T}$	1.0039	0.4396
$L2_{T}$	0.9031	0.4810
$L1_{Ext}$:$L2_{Arc}$	2.1684	0.1697

Moreover, the ANOVA result from the second iteration in Table 5.15 show that only $L2_{Arc}$ has a significant impact on the circulating current. Adding the interaction effect between $L2_{Arc}$ and $L1_{Ext}$ shows still that only $L2_{Arc}$ have a significant impact as seen in Table 5.16.

Table 5.15: F-value and P-value - second iteration

Parameter	F-value	P-value
$L1_{Ext}$	2.2613	0.1669
$L2_{Ext}$	0.3011	0.8239
$L1_{Arc}$	1.6094	0.2547
$L2_{Arc}$	5.6927	0.0183
$L1_{Pole}$	0.6013	0.6303
$L2_{Pole}$	0.8295	0.5104
$L1_{T}$	0.2072	0.8889
$L2_{T}$	0.4598	0.7176

Table 5.16: F-value and P-value - second iteration with interaction effect

Parameter	F-value	P-value
$L1_{Ext}$	3.4625	0.0998
$L2_{Ext}$	0.2824	0.8368
$L1_{Arc}$	1.3086	0.3370
$L2_{Arc}$	5.6942	0.0220
$L1_{Pole}$	0.5640	0.6538
$L2_{Pole}$	0.7780	0.5385
$L1_{T}$	0.1943	0.8973
$L2_{T}$	0.4337	0.7348
$L1_{Ext}$:$L2_{Arc}$	0.6841	0.5864

Continuing with the second iteration, the interaction effect between $L1Arc$ and

$L2_{Arc}$ shown in Table 5.17. The parameters $L1_{Ext}$ and $L1_{Pole}$ displays significance while $L2_{Arc}$ and the interaction between $L1_{Arc} : L2Arc$ are close to the threshold of significance.

Adding the interaction between $L1_{Ext}$ and $L2_{Arc}$ to the already existing interaction between $L1_{Arc}$ and $L2Arc$ can be seen in Table 5.18. The parameters that shows significance are $L1_{Ext}$, $L1_{Pole}$ and the interaction between $L1_{Arc} : L2_{Arc}$. Parameter $L2_{Ext}$ and the interaction between $L1_{Ext} : L2_{Arc}$ are close to the threshold of significance.

Table 5.17: F-value and P-value - second iteration with changed interaction effect

Parameter	F-value	P-value
$L1_{Ext}$	22.0778	0.0033
$L2_{Ext}$	3.077096	0.1121
$L1_{Arc}$	0.758967	0.5567
$L2_{Arc}$	3.897199	0.0736
$L1_{Pole}$	4.951245	0.0461
$L2_{Pole}$	2.284081	0.1790
$L1_T$	2.329128	0.1740
$L2_T$	0.738440	0.5665
$L1_{Arc}$:$L2_{Arc}$	3.6374	0.0650

Table 5.18: F-value and P-value - second iteration with double interaction effects

Parameter	F-value	P-value
$L1_{Ext}$	14.4999	0.0089
$L2_{Ext}$	3.6749	0.0820
$L1_{Arc}$	1.5662	0.2929
$L2_{Arc}$	0.2042	0.8899
$L1_{Pole}$	4.9985	0.0452
$L2_{Pole}$	2.2040	0.1884
$L1_T$	2.4012	0.1663
$L2_T$	1.8765	0.2344
$L1_{Arc}$:$L2_{Arc}$	4.2075	0.0472
$L1_{Ext}$:$L2_{Arc}$	3.7285	0.0799

The result from the ANOVA indicates that the combined interaction of the pole arc angle for both L1 and L2 magnetic layers in the model have a significant impact on the third harmonic current amplitude, followed by the extension spacing length $L1_{Ext}$ and $L1_{Pole}$. The parameters $L2_{Ext}$ and the interaction between $L1_{Ext}$ and $L2_{Arc}$ are approaching the significance threshold with p-values near 0.05, suggesting these parameters warrant further study to fully understand their impact.

The arc angle together with the flux barriers represent the pole coverage and therefore it has a large impact of the magnetic flux distribution in the air-gap which was shown by using Maxwell's equation to be directly impacting the harmonic content in the back-emf, consequently inducing the circulating current.

5.5 Rotor duct analysis

To further analyze the rotor characteristics, rotor designs incorporating a rotor duct were analyzed.

The theory in section 2.3.1.4 suggests that a rotor duct will alter the reluctance in the magnetic flux path. Hence a rotor duct placed in the D-axis was examined

concerning the circulating current under no-load conditions at 3000 rpm for the numerically optimal rotor design. In the no-load scenario, the Q-axis flux linkage is equal to zero, therefore a rotor duct placed in the Q-axis was not investigated at the mentioned operating point. This study was made in the context of the numerically optimal rotor design, which exhibits a very low third harmonic but still experiences a minor disturbance from the ninth harmonic.

The duct, seen in Figure 5.35, formed as an ellipse was simulated with the major radius swept from 0.5mm to 2.3mm to stay within geometrical constraints. Each incremental step of the swept parameter was 0.2mm.

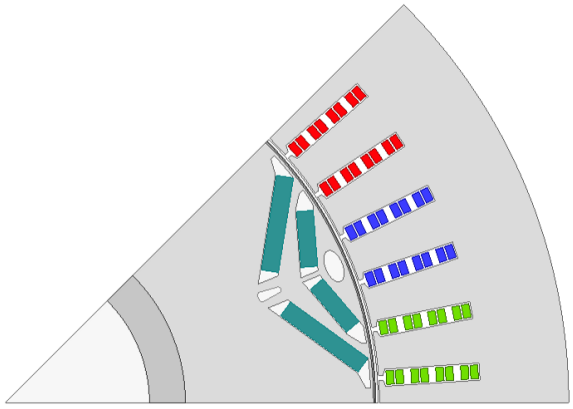

Figure 5.35: D-axis rotor duct in optimal model

Figure 5.36 shows the resulting harmonic content in the circulating current from each major radius of the elliptic duct.

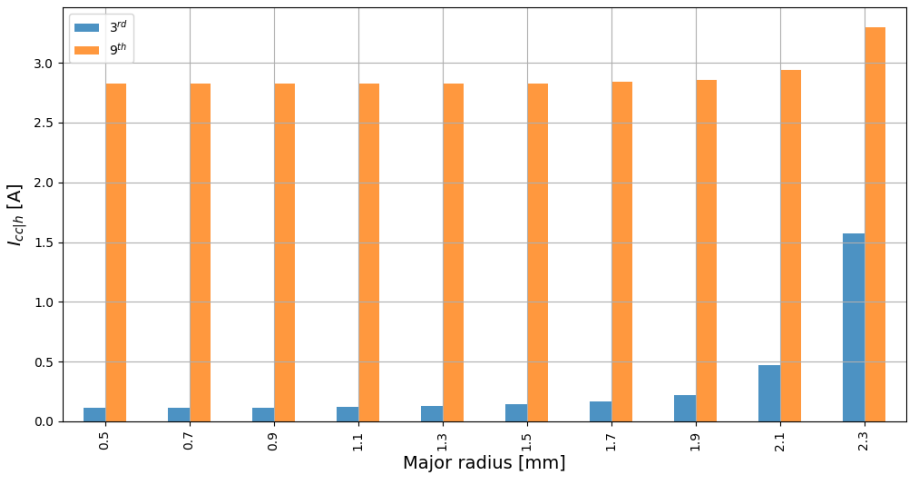

Figure 5.36: Resulting harmonic content vs major radius

As seen in Figure 5.36, the lowest harmonic content could be found in geometries with the smallest rotor ducts. The circulating current increases first at larger rotor

ducts.

To further analyze the reluctance in the rotor and its relation to the triplen harmonic, two operating points in load condition was analyzed for the D-axis rotor duct with a major radius of 1 mm. The operating points used were a line current amplitude of 500 A and 800 A with a DQ-ratio at $-45°$ and 3000rpm. This ensures a high level of saturation in the rotor and stator core shown in the previous analysis. In Figure, 5.37, the corresponding current harmonics are illustrated where it can be seen that at very high levels of saturation, the D-axis rotor duct decreases the third harmonic but increases the ninth harmonic.

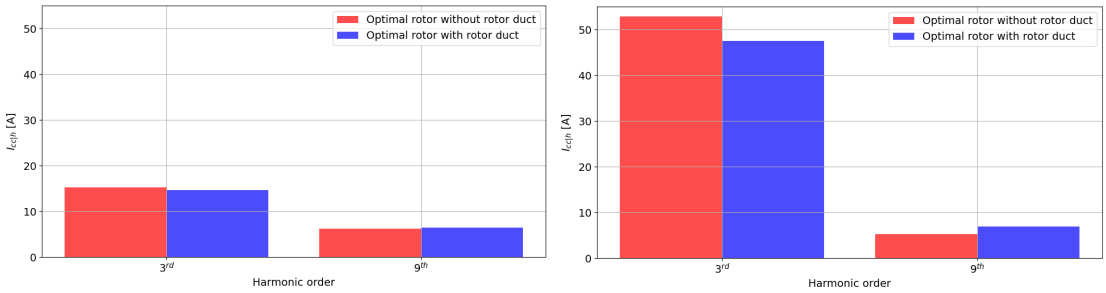

(a) Current harmonics at 500A load current

(b) Current harmonics at 800A load current

Figure 5.37: Current harmonics at high level of saturation

In addition, the corresponding flux linkage in D- and Q-axis for the 800A load point is reflected in Table 5.19.

Table 5.19: Flux linkage in D- and Q-axis comparison for rotor duct for 800A load current

Flux Linkage	D-axis	Q-axis
Optimal rotor without rotor duct	0.05131 Wb	0.1767 Wb
Optimal rotor with rotor duct	0.05111 Wb	0.1754 Wb

The duct placed in the D-axis had no impact on the triplen current harmonics for all ducts with smaller or equal major radius than 1.1 mm. For larger-sized ducts, the triplen harmonics increased with the duct size.

Moreover, under load conditions, the duct had a positive impact on the circulating current. Even though the amount of material was decreased indicating that local saturation could occur at lower input currents, the third harmonic was damped. A reasonable explanation would be that the increased reluctance induced by the rotor duct decreases the flux linkage in the D-axis and thereby dampens the third harmonic. Also, the small change in Q-axis flux linkage could be a consequence of altered cross-saturation, as a factor of the high negative D-axis current and decreased magnet flux linkage in the D-axis. Additionally, the generation of harmonics

was impacted by the divergence of magnetic flux in the D-axis which was reduced with the duct. The divergence flux could be a large factor for the decreased triplen harmonic content under load conditions compared with the no-load results.

In Figure 5.38, the resulting magnitude of the flux density along the outer part of the rotor is displayed for both the optimal numerical rotor design with and without the rotor duct, in no load condition with a slotless stator.

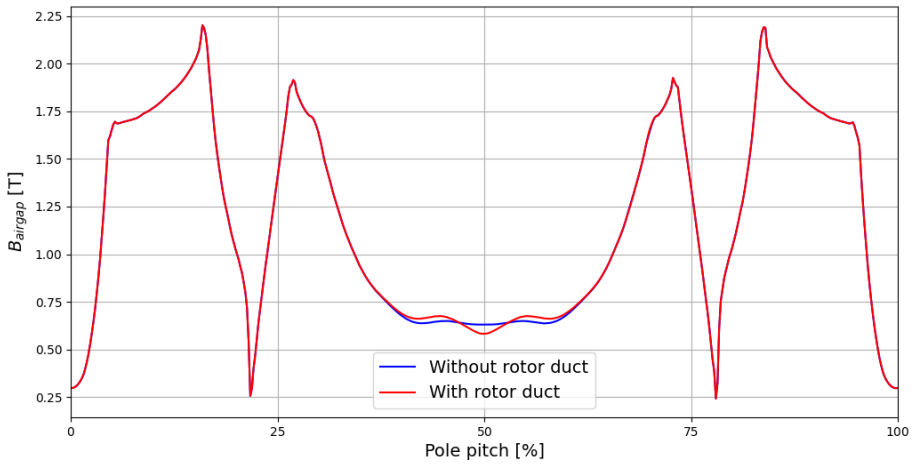

Figure 5.38: Duct impact on rotor flux

Evidently, the rotor flux is impacted by the duct seen in the middle of the pole pitch where the concentration of flux is altered.

6
Compared Analysis

This chapter compares the analytical and numerical results. First, the corresponding air-gap flux waveforms from both methods were compared. Then, the optimal segments generated in the analytical optimization were applied in the numerical model and the circulating currents were studied.

6.1 Air-gap flux density

In the numerical analysis, the circulating current was clearly visualized, unlike in the analytical analysis. However, both methods were able to visualize the waveform of the air-gap flux density. Figure 6.1 compares the air-gap flux densities under one pole pitch between the analytically optimized model and the numerically optimized model. The comparison was conducted under no-load conditions. Importantly, the amplitudes in the analytical calculations were adjusted to match the amplitude of the numerical model. Consequently, the optimized segments from the analytical model were recalculated, as the optimization algorithm factors in the magnitude of each segment.

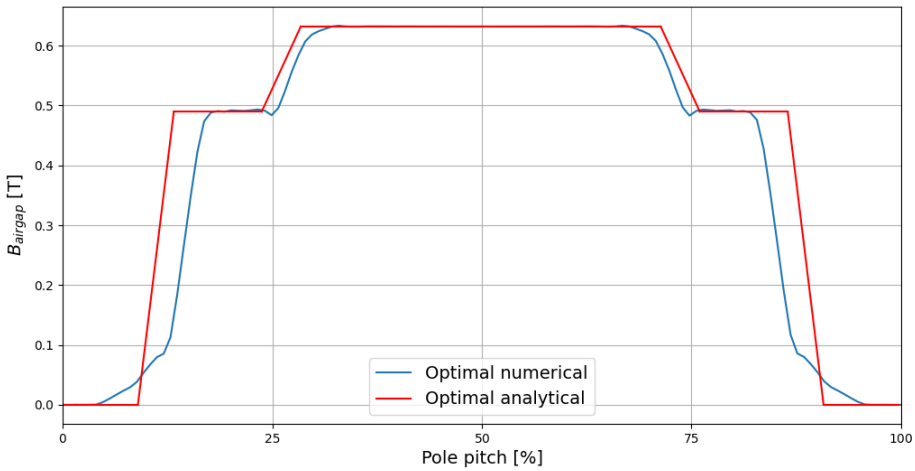

Figure 6.1: Compared optimal air-gap flux density

Undoubtedly, there are notable similarities in the optimal shapes of the waveform between the analytical and numerical analyses. However, the most apparent difference lies in the width of the waveform, where both the top and bottom parts of the analytical waveform were wider than the numerical one. The insights from

the variation in the waveform influenced by the individual parameters, explored in section 5.3.2, could be used to identify the specific differences. The arc angles for L_1 and L_2 were larger for the analytical model, as well as the extension length spacing for the flux barrier of L_1, which appears larger for the optimal numerical model.

To further investigate the precision of the analytical method, the optimal segments that analytically indicated minimal third harmonic amplitude in the air-gap flux were implemented in the slotless numerical model. The resulting magnetic alignment is displayed in Figure 6.2, where the segments α_1-α_5 are displayed and separated with marking lines on the right-hand side.

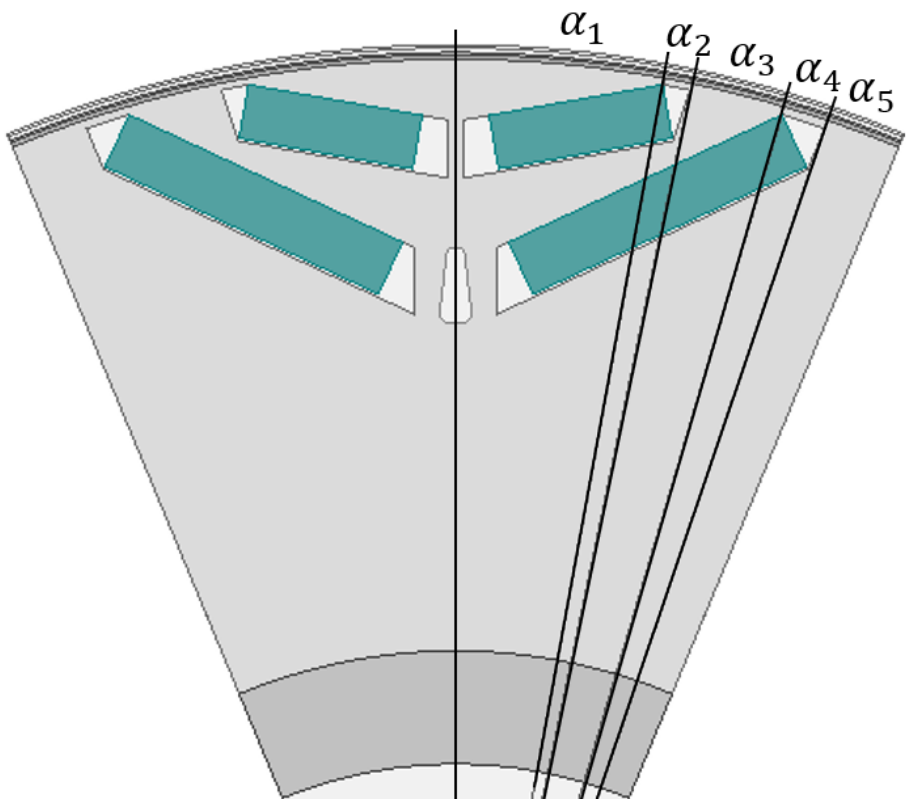

Figure 6.2: Analytical segments in numerical model

The resulting flux density from the numerical model with the analytical optimal segmentation is illustrated in Figure 6.3. It is evident that the segmentation itself does not generate an identical flux waveform, indicating that other parameters have a deciding impact on the wave shape. Although the two waveforms are not identical, the greatest similarity can be seen in the width of the waves, aligning with the expectations.

6.2 Circulating current

To investigate the circulating current generated by the waveform of the air-gap flux density, derived from the analytical calculation method, the numerical model was

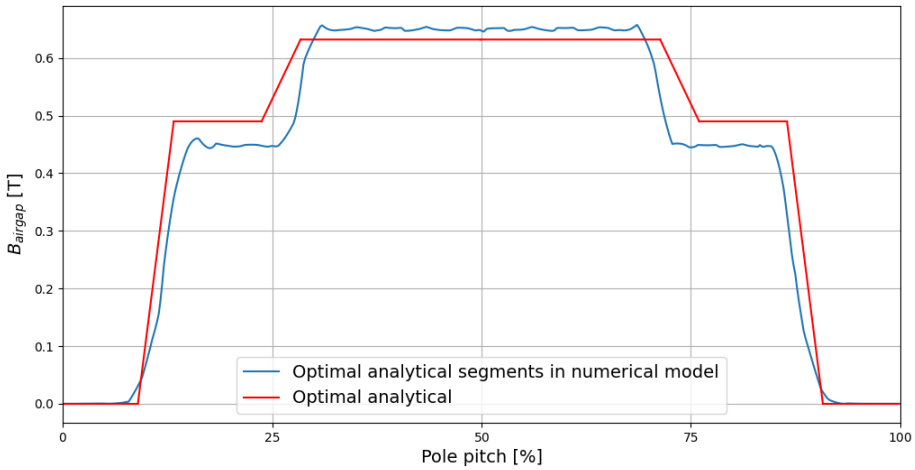

Figure 6.3: Optimal air-gap flux density: analytical segments in numerical model

incorporated with the analytical segments, generating the waveform presented in Figure 6.3. It was simulated in no load at 3000rpm with the same stator as in the numerical analysis.

The resulting current harmonics visualized in Figure 6.4, reveal that the triplen harmonics from the conversion from analytical segments to the numerical model were 18.14% lower than those generated by the initial numerical model, as showed in Figure 5.7. Notably, the third harmonic exhibited a significant decrease of 68.97%, whereas the ninth harmonic only decreased by 0.5% A and the fifteenth harmonic increased by 75.57%. This suggest that the use of the segmented pole coverage method made it feasible to reduce the circulating current in the numerical delta connected DIPMSM.

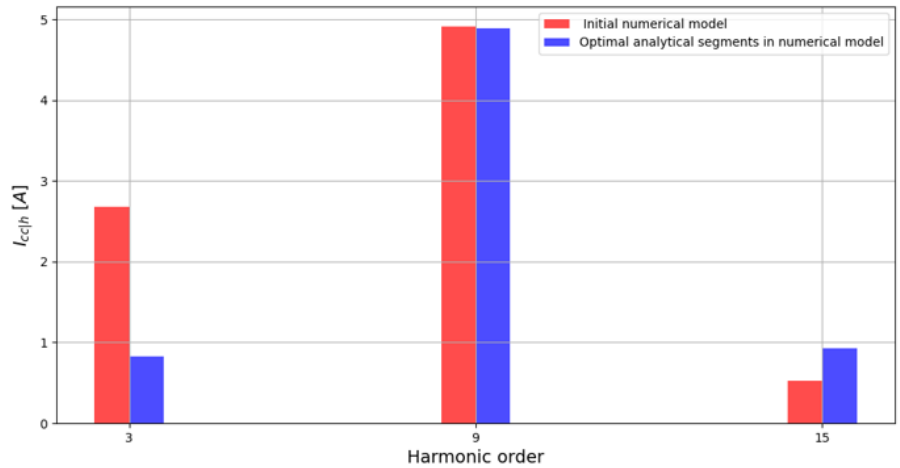

Figure 6.4: Circulating current harmonics: analytical segments in numerical model

7
Conclusion

The conducted analyses, both analytical and numerical, provided a comprehensive insight into the generation of triplen harmonics in relation to the rotor design. However, it is critical to highlight that changing the parameters to minimize the circulating currents could significantly influence other vital machine characteristics, such as average torque amplitude and torque ripple. These characteristics were not explored in the thesis, as it was solely focused on the circulating currents.

The analysis confirmed that the triplen harmonics induces circulating currents in the delta connection. The magnitude of this circulating current can be characterized as the cumulative sum of the amplitudes of the individual harmonic components corresponding to the triplen harmonic orders. The circulating current can also be expressed as a ratio-function of the triplen harmonic present in the back-emf and the impedance consisting of the resistive and inductive components in the machine. In higher rotational speeds, the circulating current was constant implying that the inductive attributes becomes dominant and the resistance can be neglected.

In addition, the thesis confirmed that the relationship between the circulating current and the triplen harmonic is a combination of the triplen harmonics induced due to the imbalance generated by the magnet positioning as well as the triplen harmonics generated as a result of saturation. When the iron core saturates the third harmonic current amplitude drastically increased. The stator teeth were shown to experience the highest level of saturation. By reducing the width of the stator teeth, the third harmonic current amplitude increased further.

The study determines the pole coverage as the main contributor to the triplen harmonic from the rotor design perspective. Unlike a surface-mounted PMSM where two-thirds pole coverage minimized the triplen harmonic, the double V-shaped design demonstrated the necessity of a pole coverage greater than two-thirds to effectively reduce triplen harmonics. This compensation accounts for the counteracting triplen harmonic flux generated by the outer portion of the first magnet layer.

It can be concluded, for the double V-shaped topology, the pole arc angles have the largest impact followed by the flux barrier extension lengths. This was shown with the use of spectral analysis, breaking down the current harmonic components in the delta loop. With that, an optimization could be constructed to minimize the circulating current as a function of the rotor parameters. The third harmonic in the delta loop was reduced by 95.5% in no load and 5.7% in maximum load conduction

with the optimal rotor design. This indicates that the saturation effect inducting the third harmonic can not be eliminated by optimal alignment of the rotor parameters.

The analysis of the stator winding losses attributed to the third harmonic current amplitude across varying load currents was undertaken. The findings revealed a significant reduction of 89.5% in winding losses in the 0-350A load current range and in the 400-800A, the reduction was calculated to 15%, compared to the initial model. This reduction not only underscores the effectiveness of the optimization techniques applied but also highlights the impact of the saturation at higher load currents, which diminishes the significance of the rotor parameters in terms of loss reduction. Decreasing the stator teeth width further increased the amplitude of the copper losses.

Furthermore, the study concludes that in loaded conditions the third harmonic can be reduced by placing a duct in the rotor D-axis. In the maximum load condition, the third harmonic was reduced by 10%. Meanwhile, the ninth harmonic increased by 24.7%. Although there was a significant increase in the ninth harmonic, its amplitude is relatively low compared with the third harmonic, consequently, the circulating current could be reduced by 6.2%. However, the flux in both D- and Q-axis were decreased by 0.39% and 0.74% respectively, indicating that the duct can have a slightly negative impact on the torque.

Additionally, the optimal segments found in the analytical analysis could be applied in the numerical model and thereby the circulating currents could be studied. The third and ninth current harmonics could be seen decreasing by 68.97% and 0.5% respectively, and the fifteen harmonic was increased by 75.57%, when comparing the model to the initial numerical model. However, the sum of the triplen harmonic components were decreased by 18.14%. The outcome of the optimal segments from the analytical analysis implemented in the numerical model was a significant decrease in circulating current in no load condition. This demonstrated that the segmented pole coverage method can be used for analysing the harmonics generated by specific rotor design.

Finally, optimizing the rotor design can help reducing the circulating currents in delta connected DIPMSM. However, the effectiveness of such optimization diminishes considerably when the iron core saturates. Hence, decreasing the specific magnetic loading and utilizing material with extremely high relative permeability could potentially prolong the unsaturated mode of operation, enabling circulating currents within acceptance. Such a machine design is considered unrealistic as the desired traits of space-, material- and weight-saving, as well as cost are compensated for.

7.1 Future work

To further evaluate the impact of circulating currents in the delta connection, studies covering a wider range of rotor topologies could enhance the general understanding of circulating currents. Optimizing the rotor structure to solely minimize the circulating currents could lead to other unwanted characteristics such as decreased torque and increased torque ripple. In further research targeting usable design, the objective function for the minimization should therefore include the impacts of other important parameters such as those just mentioned.

Control strategies are widely used to reduce harmonics. Future research could explore the potential of incorporating signal injection with pulse-width modulation as a method to potentially mitigate harmonics in the circulating currents. This could work as a complement, or even replacement to the optimized rotor design, or used at higher loads when the stator saturates.

It is clear that FEM models provide a good representation of realistic characteristics. However, conducting measurements on a realistic model could further improve the understanding of the circulating current characteristics. Especially how Lenz's law impacts the back-EMF harmonics

The losses in the models did not represent the total losses in a PMSM as only copper losses from the circulating currents were studied. Further investigation of losses such as copper losses from the fundamental current and iron losses is needed for a more accurate conclusion of the total amount of losses in a delta connected machine.

Lastly, the thesis have been limited to only considering full-pitch winding, whereas a common method to eliminate harmonics is with factorial winding. However, as with all design parameters, factorial winding comes with compromised machine performance. To ensure optimal winding layout and minimize the circulating currents, structured analysis of factorial winding configurations is needed.

Bibliography

[1] European Commission, “Reducing CO2 emissions from heavy-duty vehicles,” Climate Action, 2023. https://climate.ec.europa.eu/eu-action/transport/road-transport-reducing-co2-emissions-vehicles/reducing-co2-emissions-heavy-duty-vehicles_en. Accessed on: 2024-02-01.

[2] European Commission, “The European Green Deal", Jul. 14, 2021. [Online]. Available: https://commission.europa.eu/strategy-and-policy/priorities-2019-2024/european-green-deal_en. Accessed on: 2024-02-01.

[3] “Climate,” Volvo Group, 2024. [Online]. Available: https://www.volvogroup.com/en/sustainable-transportation/responsible-business/climate.html. Accessed on: 2024-02-01.

[4] C. Dinca and U. Schäfer, “Circulating currents of delta connected fractional slot machines for mass production,” E & I Elektrotechnik Und Informationstechnik, vol. 132, no. 1, pp. 68–74, 2015.

[5] E. Nipp, “Permanent magnet motor drives with switched stator windings,” KTH Royal Institute of Technology, 1999.

[6] P. Pramod, "Circulating Currents in Delta Wound Permanent Magnet Synchronous Machines", MicroVision, Inc., Redmond, USA. ORCiD 0000-0001-9835-0380.

[7] S. Mukundan, H. Dhulipati, Z. Li, M. S. Toulabi, J. Tjong and N. C. Kar, "Coupled Magnetic Circuit-Based Design of an IPMSM for Reduction of Circulating Currents in Asymmetrical Star–Delta Windings," in IEEE Transactions on Transportation Electrification, vol. 8, no. 2, pp. 2971-2984, 2022.

[8] A. S. Raju and D. C. Thakur, "Delta connected PMSM for traction of heavy vehicles", MSc thesis, Faculty of Science and Technology, Uppsala University, Uppsala 2023.

[9] B. Hassan, "Environmental Impact of Modern Permanent Magnets" in *Modern Permanent Magnets - Fundamentals and Applications*, IntechOpen, Sep. 22, 2023.

[10] A. Küchler, "Electrical Stresses in High Voltage Engineering" in *High voltage engineering: Fundamentals - Technology - Applications*. Springer, 2017. ch 2.2.

[11] A. Arzillo et al., "An Analytical Approach for the Design of Innovative Hairpin Winding Layouts," 2020 International Conference on Electrical Machines (ICEM), Gothenburg, Sweden, 2020, pp. 1534-1539.

[12] T. Glaessel, J. Seefried and J. Franke, "Challenges in the manufacturing of hairpin windings and application opportunities of infrared lasers for the contacting process," 2017 7th International Electric Drives Production Conference (EDPC), Würzburg, Germany, 2017, pp. 1-7.

[13] E. Acha, V. G. Agelidis, O. Anaya-Lara, and T. J. E. Miller, "Power systems engineering - fundamental concepts" in *Power Electronic Control in Electrical Systems*, Newnes, 2002, ch 2.12, pp. 72–78.

[14] T. A. Lipo, Introduction to AC machine design. John Wiley & Sons, New Jersey, USA, 2017.

[15] F. Rehm, P. Breining, S. Decker, J. Kolb and M. Hiller, "Loss Comparison of Small Delta- and Star-Connected Permanent Magnet Synchronous Machines," IECON 2019 - 45th Annual Conference of the IEEE Industrial Electronics Society, Lisbon, Portugal, 2019, pp. 1171-1176.

[16] N. Bianchi and S. Bolognani, "Interior PM synchronous motor for high performance applications," IEEE Conference Publication | IEEE Xplore, 2002.

[17] O. Wallmark, *AC Machine Analysis: Fundamental Theory*. Stockholm, Sweden: KTH Royal Institute of Technology, 2015.

[18] A. Wang, J. Zhao and Y. Wang, "Optimal shape design of rotor to reduce torque ripple for IPM motor based on the principle of mutual harmonics exclusion," 2012 15th International Conference on Electrical Machines and Systems (ICEMS), Sapporo, Japan, 2012, pp. 1-5.

[19] H. Polinder, "Principles of electrical design of permanent magnet generators for direct drive renewable energy systems," in *Electrical Drives for Direct Drive Renewable Energy Systems*, 2013, pp. 30–50.

[20] J. -W. Kwon, M. Li and B. -I. Kwon, "Design of V-Type Consequent-Pole IPM Machine for PM Cost Reduction With Analytical Method," in IEEE Access, vol. 9, pp. 77386-77397, 2021.

[21] K. Wang, J. X. Shen, F. Z. Zhou, R. H. Qiu, R. G. Lin, "Optimal design of magnet pole arc considering utility of third-harmonic back-EMF in high-speed sensorless brushless DC motors," 2007 International Confer-

ence on Electrical Machines and Systems (ICEMS), Seoul, Korea (South), 2007.

[22] K. Yong-Ho, K. Soon-O, T. Sun, H. Jung-Pyo, "Initial design using space harmonic analysis methods in permanent magnet synchronous machines," Digests of the 2010 14th Biennial IEEE Conference on Electromagnetic Field Computation, Chicago, IL, 2010, pp. 1-1.

[23] M. Wang, H. Zhu, C. Zhou, P. Zheng and C. Tong, "Analysis and Optimization of a V-Shape Combined Pole Interior Permanent-Magnet Synchronous Machine With Temperature Rise and Demagnetization Considered," in IEEE Access, vol. 9, pp. 64761-64775, 2021.

[24] S. Lee, J. Hong, S. B. Lee, E. Wiedenbrug, M. Teska and H. Kim, "Evaluation of the influence of rotor axial air ducts on condition monitoring of induction motors," 2012 IEEE Energy Conversion Congress and Exposition (ECCE), Raleigh, NC, USA, 2012, pp. 3016-3023.

[25] The SciPy community, “SciPy v1.12.0 Manual”, 2024. [Online]. Available: https://docs.scipy.org/doc/scipy/reference/generated/scipy.optimize.minimize.html. Accessed on: 2023-11-20.

[26] Minitab Inc., “Taguchi designs”, 2023. [Online]. Available: https://support.minitab.com/en-us/minitab/21/help-and-how-to/statistical-modeling/doe/supporting-topics/taguchi-designs/taguchi-designs/. Accessed on: 2023-12-10.

[27] Minitab Inc., “Analysis of Variance table for One-Way ANOVA”, 2023. [Online]. Available: https://support.minitab.com/en-us/minitab/21/help-and-how-to/statistical-modeling/doe/supporting-topics/taguchi-designs/taguchi-designs/. Accessed on: 2023-12-20.

A

Appendix 1

```
"""
Finding the optimal analytical pole coverage
    Master's thesis 2024
"""
import numpy as np
from scipy.integrate import quad
from scipy.optimize import minimize

### Define parameters ###
p = 8 # Nr of poles
n = 3 # Harmonic multiple
A = 1  # Scaled magnetic flux L1 magnet
B = 1  # Scaled magnetic flux L2 magnet

Matrix_size = 100 # Size of swept data

# Defined boundaries
a1_bounds = [np.pi/40, np.pi/8] # 20%-100%
a2_bounds = [np.pi/100, np.pi/40] # 8%-20%
a3_bounds = [np.pi/80, np.pi/20] # 10%-40%
a4_bounds = [np.pi/100, np.pi/40] # 8%-20%

# Creates segment data
a1_arr = np.linspace(float(a1_bounds[0]), float(a1_bounds[1]),
    Matrix_size)
a2_arr = np.linspace(float(a2_bounds[0]), float(a2_bounds[1]),
    Matrix_size)
a3_arr = np.linspace(float(a3_bounds[0]), float(a3_bounds[1]),
    Matrix_size)
a4_arr = np.linspace(float(a4_bounds[0]), float(a4_bounds[1]),
    Matrix_size)

# Defines integrals
def integrate_result1(alpha_1):
    f1_1 = lambda theta: A * np.cos(n * p * theta / 2) + B * np.cos
    (n * p * theta / 2)
    result, _ = quad(f1_1, 0, alpha_1)
    return (p / np.pi) * result
def integrate_result2(alpha_1, alpha_2):
    f2_2 = lambda theta: (A+B / alpha_2) * (alpha_1 + alpha_2 -
    theta) * np.cos(n * p * theta / 2)
    result, _ = quad(f2_2, alpha_1, alpha_1 + alpha_2 )
```

```
    return (p / np.pi) * result
def integrate_result3(alpha_1, alpha_2, alpha_3):
    f3_3 = lambda theta: A * np.cos(n * p * theta / 2)
    result, _ = quad(f3_3, alpha_1 + alpha_2, alpha_1 + alpha_2 +
   alpha_3)
    return (p / np.pi) * result
def integrate_result4(alpha_1, alpha_2, alpha_3, alpha_4, ):
    f2_2 = lambda theta: (A/ alpha_4) * (alpha_1 + alpha_2 +
   alpha_3 + alpha_4 - theta) * np.cos(n * p * theta / 2)
    result, _ = quad(f2_2, alpha_1 + alpha_2 + alpha_3, alpha_1 +
   alpha_2 + alpha_3 + alpha_4)
    return (p / np.pi) * result

objective_values = []
def objective_function(segments):  # Objective function
    alpha_1, alpha_2, alpha_3, alpha_4 = segments
    result= (
        integrate_result1(alpha_1)
        + integrate_result2(alpha_1, alpha_2)
        + integrate_result3(alpha_1, alpha_2, alpha_3)
        + integrate_result4(alpha_1, alpha_2, alpha_3, alpha_4))
    return abs(result)

initial_guess = [np.pi/12, a2_arr[0], np.pi/40, a4_arr[0]] # Based
   on values from plots

# Defines boundaries for the optimizatoin
bounds = [
    (min(a1_arr), max(a1_arr)),
    (min(a2_arr), max(a2_arr)),
    (min(a3_arr), max(a3_arr)),
    (min(a4_arr), max(a4_arr)),
]

result = minimize(objective_function, initial_guess, bounds=bounds,
    method='Nelder-Mead') # Simplex algorithm
min_sum_harmoninc= result.fun
optimal_segment = result.x

segments = []
for i in optimal_segment: #creates list with segments converted to
   percentage of pole coverage
    val = ((i/(sum(optimal_segment)+(np.pi/8)-sum(optimal_segment))
   ))*100
    segments.append(val)
segments.append((((np.pi/8)-sum(optimal_segment))/(sum(
   optimal_segment)+(np.pi/8)-sum(optimal_segment)))*100)

print(result)
print(f"Minimum B_[airgap|3]: {min_sum_harmoninc} [T]")
print(f"Optimal segments: a1 = {segments[0]:.2f}%, a2 = {segments
   [1]:.2f}%, a3 = {segments[2]:.2f}%, a4 = {segments[3]:.2f}%, a5
   = {segments[4]:.2f}%")
```

Listing A.1: Python code for analytical optimization.

DEPARTMENT OF ELECTRICAL ENGINEERING
CHALMERS UNIVERSITY OF TECHNOLOGY
Gothenburg, Sweden
www.chalmers.se

CHALMERS
UNIVERSITY OF TECHNOLOGY